Title

COHERENCE AND RELAXATION IN ENERGY TRANSFER PROCESSES IN CONDENSED PHASES

Author

Shelby, Robert Mckinnon.

Publication Date

1978-03-01

Thesis/dissertation

COHERENCE AND RELAXATION IN ENERGY TRANSFER PROCESSES IN CONDENSED PHASES

Robert McKinnon Shelby
(Ph. D. thesis)

March 1978

Prepared for the U. S. Department of Energy
under Contract W-7405-ENG-48

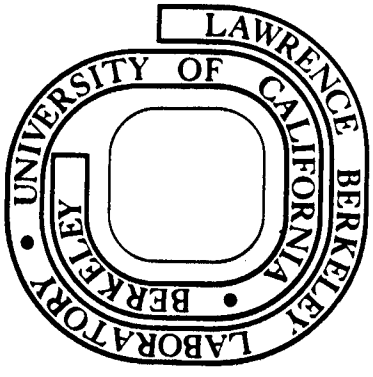

DISCLAIMER

COHERENCE AND RELAXATION IN ENERGY TRANSFER PROCESSES IN CONDENSED PHASES

Robert McKinnon Shelby

Materials and Molecular Research Division, Lawrence Berkeley Laboratory
and Department of Chemistry, University of California
Berkeley, California 94720

ABSTRACT

Investigations of electronic triplet and vibrational energy transfer dynamics and relaxation processes are presented. Emphasis is placed on understanding the role of coherence and interactions which tend to destroy the coherence. In the case of triplet excitons at low temperatures, the importance of coherence in energy migration can be established, and the average coherence parameters can be experimentally determined. In the case of vibrational excitations, both picosecond spectroscopic studies of vibrational relaxation and spontaneous Raman spectroscopy are used to characterize the dynamics and give increased insight into the nature of the mechanisms responsible for vibrational dephasing. The design and operation of the picosecond apparatus used in these experiments is also described.

The coherence of electronic triplet energy propagation in organic solids at liquid helium temperatures is established from the time resolved response of the crystal to short optical pulses obtained from a dye laser (pumped by a nitrogen gas laser). The effects of trapping and

detrapping of the excitations by perturbed molecules (x-traps) is evident in both 1,2,4,5-tetrachlorobenzene (TCB) and 1,4,-dibromonaphthalene (DBN). In the TCB system a simple kinetic description of the band-trap equilibrium allows the extraction of a minimum average coherence length: $\langle \ell \rangle \geq 700$ Å = 186 molecules for this one-dimensional exciton. This magnitude clearly exceeds the random walk limit and is related to the thermalization mechanisms in this system.

To help characterize the coherence of vibrational excitations in molecular solids and liquids, the dephasing times of C-H bending mode overtones in 1,2,4,5-tetramethylbenzene (durene) single crystal and liquid and p-xylene liquid were measured using coherent Raman probe scattering of picosecond pulses. These dephasing times are in the 0.5 to 3 psec region, and their determination was facilitated by fitting the experimental data to numerical solutions of the equations which describe the stimulated Raman excitation and probing processes for homogeneously and inhomogeneously broadened lines. Comparisons of these results with spontaneous Raman spectra of these compounds and with previous picosecond data in methanol suggest that inhomogeneous broadening may be an important source of linewidth in liquids for this vibration.

For polyatomic molecules such as these, an important dephasing mechanism is intramolecular interactions between vibrational modes. For example, it is shown that Raman lineshape functions and vibrational dephasing times can reflect random frequency modulation of high frequency vibrational modes due to the exchange of thermal energy among low-frequency modes. When this exchange process is incorporated into the

vibrational correlation function, an analysis of the temperature dependence of the spontaneous Raman spectrum in the "intermediate exchange" regime allows one to obtain: (1) Life times and scattering rates which characterize the dominant dephasing channels, and (2) A measure of the strength of the interaction responsible for the intramolecular coupling. These ideas are applied to an analysis of the C-H stretching modes of the durene molecule in the solid phase. It is found that single low-frequency methyl group motions dominate the dephasing and that the $Q_1^2 Q_2^2$ term in the anharmonic potential may play an important role in the coupling.

This work is dedicated to Diane and to my parents for their support, encouragement and understanding.

Table of Contents

INTRODUCTION

The study of the transfer and dissipation of energy provides an important avenue toward a more complete understanding of the structure and dynamics of molecular solids and liquids. The behavior of condensed phases is qualitatively different from that of gases in that intermolecular effects play a much more dominant role. For example, in the gas phase one can hope to study the properties of essentially isolated molecules which are only weakly perturbed by their environment through collisions. Although a similar viewpoint may sometimes prove valuable in condensed phase studies, one often studies macroscopic properties which are more properly identified with closely coupled molecular aggregates. This is particularly true of energy transfer and relaxation studies, since these phenomena intrinsically involve interactions of molecules with their environment and its degrees of freedom. Thus, it is essential to develop experiments, models and viewpoints which are capable of bridging the gap between macroscopic observables and the interesting features of the dynamics.

In the case of crystalline solids, the periodicity of the crystal lattice helps to simplify the equations of motion of the N-interacting-molecule system. The solution[1] (to a certain degree of approximation) consists of collective excitations of the crystal characterized by their "crystal momentum," or wave vector. When these elementary crystal excitations or "quasiparticles" interact relatively weakly with one another, they form a useful starting point for a description of the dynamics of

excitations in a real crystal. This description will be called the coherent model since quantum mechanical phase relationships among the excited molecules are preserved for a significant time period compared to the time required for energy transfer to take place. The excitations are delocalized over a substantial number of lattice sites and move through the crystal in a wavelike fashion. An example of such a system is provided by electronic triplet excitations in some organic molecular crystals.[9] The coherent limit is interesting because it results in energy transport over relatively large distances during the excited lifetime as compared with the diffusive mode of transport discussed below.

Interactions which disrupt the coherence are those which scramble the well-defined phase relationship. In the case of triplet excitons for example, the coupling between the excitons and lattice vibrations (phonons) as well as scattering by impurity sites and crystal defects tends to cause mixtures of quasiparticle states or k-states to form and evolve in time in a random fashion. The interactions which cause this dephasing are very interesting in their own rite, since few systems exist in which this sort of interaction has been characterized in detail. Because of their importance in determining the macroscopic energy transfer properties of a system, these interactions and their associated relaxation processes are a subject of intense investigation.

When these perturbations become sufficiently strong that the phases are no longer well defined, the idea of collective excitations loses utility, and k, the crystal momentum, is no longer a good quantum number. One can say that in effect, the perfect periodicity present in an ideal crystal has been disrupted. This picture will be termed the

incoherent limit. For example, this limit would be appropriate when exciton-phonon scattering is rapid compared to the time required for the exciton to move one lattice spacing. Since the evolution in time of excited molecules in different parts of the crystal is uncorrelated, this limit is also called the localized limit.[2] In the localized picture energy transfer occurs as a diffusive random walk from one lattice site to another of these localized excitations. One thinks in terms of an excited molecule immersed in a reservoir of unexcited molecules. Since the crystal periodicity plays little role, this picture is also useful in discussing dynamics of excitations in molecular liquids. In many respects, the dynamics of intramolecular excitations in liquids and in solids when the localized picture is appropriate would be expected to be similar.

In any real system the dynamics would be classified as intermediate between the coherent and incoherent limits. A good deal of theoretical effort has been expended toward understanding energy transport in this intermediate regime.[3,4] This work has largely centered on incorporating the effects of perturbations such as exciton-phonon coupling into the description of the dynamics. As one intuitively expects, the motion is coherent at short times and diffusive and incoherent at long times, depending on the strength of the perturbation. It is useful to think of this kind of motion in terms of its coherence time, which represents the time required for loss of phase memory. Similarly, one can also characterize the exciton motion by an effective mean free path or coherence length which may or may not be simply related to the

coherence time.

In order to quantitatively characterize energy transfer dynamics in a specific system, experimental probes must be devised to isolate and observe the features mentioned above. In the case of triplet excitons in molecular crystals, measurement of the coherence parameters has proved somewhat elusive and ambiguous. For example, none of the techniques in wide use in the past several years has been able to provide information specifically related to the coherence length of triplet excitons. In Part One of this thesis experimental results are presented which are capable of placing a lower bound on the coherence length. This measurement is indirect, since it is based on a determination of the rate of exciton trapping at low temperatures following excitation of the crystal by a pulsed tunable dye laser. The results further establish the importance of coherent energy migration in such systems.

In contrast to the situation in triplet excitons, much less is known about energy transfer and relaxation mechanisms of vibrational excitations. Much of the work presented here is directed toward characterization of important vibrational relaxation mechanisms in molecular crystals and liquids. Quite aside from energy transfer, the understanding of vibrational dephasing and the redistribution of vibrational energy is an important problem and has received much recent attention. The advent of picosecond laser spectroscopy has resulted in direct vibrational relaxation measurements and several vibrational decay schemes in liquids have been investigated.[5] These advances have stimulated several theoretical works[6] in the field which have met with some success in

estimating decay rates based on simple models of the interactions of a vibrationally excited molecule with its surroundings.

The work presented here extends these investigations and attempts to more fully characterize the dynamics of vibrationally excited states. The experimental techniques include spontaneous Raman spectroscopy and picosecond spectroscopy. In Part Two, the construction, operation, and characterization of the picosecond apparatus used in these experiments is described from the perspective of a variety of possible applications. Part Three describes the application of these techniques to vibrational excitations. After a brief introduction to vibrational relaxation in section I, results of picosecond dephasing measurements in 1,2,4,5-tetramethylbenzene (durene) and p-xylene are presented in section II. Possible interpretations and relevant dephasing mechanisms are also discussed. Finally, in section III experimental evidence for the importance of a previously overlooked dephasing mechanism is given. This mechanism bears a strong resemblance to exchange theory in NMR and may be of general applicability in describing the dephasing of vibrationally excited polyatomic molecules in condensed phases, as well as in the description of similar processes in other branches of spectroscopy. The theoretical basis of this mechanism is outlined from the point of view of vibrational dephasing in liquids and solids, and its application to experimental results in durene is demonstrated.

In the last part of this thesis, the author attempts to stand back and assess the knowledge that has been gained, and to present some thoughts on the possible future direction of this line of research.

PART ONE

Coherent Energy Migration: Measurement of the Triplet Exciton Coherence Length Using Tunable Dye Lasers

I. Introduction

The coherence of excited triplet state energy transfer dynamics in organic molecular crystals has been studied using a variety of experimental probes. The dynamics have been inferred indirectly in steady state experiments through the interaction of excitons with traps[7] (perturbed molecules or impurities with excited triplet states of lower energy than that of the exciton). The coherence can also be monitored in the frequency domain via ESR[8] and ODMR[9] lineshape studies and by optical lineshape studies.[10] The interpretation of the observed lineshape in terms of the exciton coherence is complicated however, by contributions to the linewidth due to inhomogeneous broadening and other dephasing mechanisms which do not destroy the exciton coherence. In spite of these problems, ODMR studies of excitons[9] in 1,2,4,5-tetrachlorobenzene (TCB) and excited dimers[11] of TCB have succeeded in placing a lower bound on the coherence time of $\tau_c \sim 10^{-7}$ sec. ESR and optical studies of other systems such as 1,4,-dibromonaphthalene[12] also show evidence of a certain degree of coherence. More recently, a series of pulsed ESR and ODMR experiments[13-15] have been developed which are capable of preparing, isolating, and following the time evolution of well-defined linear combinations of triplet sublevels. These techniques serve to eliminate the

effects of unwanted contributions such as inhomogeneous broadening, spectral diffusion, etc. While these experiments are valuable probes of the dynamics, they have been successfully applied only to trapped excitations, and exciton dynamics must be deduced indirectly.

The use of tunable dye lasers can significantly broaden the scope of energy transfer studies in these systems, since the coherence and spectral purity of the laser enables the optical preparation of well-defined excited states. By monitoring the time dependence of these states it should be possible to directly obtain dynamical information related to interactions with phonons, traps, and crystal imperfections, and their effect on the coherence.

When the effect of such perturbations is dominated by resonant transfer interactions between an excited molecule and surrounding molecules in the ground state, the crystal periodicity plays an important role, and the delocalized picture of exciton dynamics is useful. The effect of the intermolecular interaction is to broaden the excited state into a band of states which are delocalized spatially over the N-molecule crystal. In a one-dimensional system, the delocalized wave functions or k-states are given by the Bloch Theorem:[1,2]

$$\psi_k = \sum_{n=1}^{N} \phi_n \exp [\, ikan] \qquad (1)$$

where a is the lattice spacing, the allowed values of the crystal momentum, k, are

$$k = \frac{2\pi}{Na} j; \quad j = -N/2, -N/2 + 1, \cdots, N/2 - 1, \tag{2}$$

and the function ϕ_n represents a state where the excitation is localized on molecule n. The energies of these states in the nearest neighbor approximation are

$$E(k) = E^o + 2\beta \cos ka \tag{3}$$

where β is the resonant intermolecular interaction between neighboring molecules, and E^o is the excited state energy in the absence of β. As indicated in Fig. 1, the intermolecular interaction also generates a rate of excitation transfer, $V_g(k)$. V_g is the group velocity of a wave packet (linear combination) of k-states with values of the wave vector near the value k, and is given by

$$V_g(k) = [1/\hbar]\,[\partial E(k)/\partial k] = (2\beta a/\hbar) \sin ka. \tag{4}$$

These equations along with the delocalized exciton states form the basis for a description of exciton dynamics in the coherent limit.

These expressions refer to individual k-states or wavepackets. However, in many cases one is concerned with the properties of an ensemble of excited states described by some distribution function (see Fig. 1). If the excited state lifetime is sufficiently long, this distribution will be given by a Boltzmann distribution.[7] Thermal equilibrium among the k-states is attained primarily due to scattering of the excitons by phonons. The timescale required for this thermalization process has not been determined with certainty for triplet excitons. The distribution among the k-states may also be strongly influenced by other effects such as trapping. For example, if excitations are selectively trapped

Figure 1. This figure schematically illustrates the basic ideas and parameters which are used to discuss coherence in energy transfer processes. It shows the one-dimensional exciton band dispersion, the group velocity, and the effect of finite coherence time and coherence length. The thermal distribution function is also shown.

COHERENT PROPERTIES OF EXCITONS

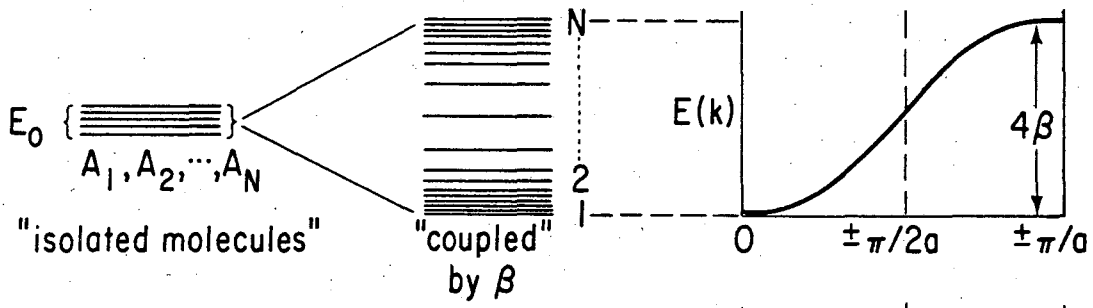

1. β generates a rate of energy transfer between molecules: $\nu_g(k)$.
2. Coherence lifetime, $\tau(k)$, generates a width to the state *and* a mean-free path for coherent energy migration

$$\ell(k) = \nu_g(k) \cdot \tau(k)$$

$$\tau(k)^{-1} \equiv \sum_{k'} (\tau_{kk'})^{-1} = \Gamma(k)$$

3. Distribution Function, D(k), determines the partition of energy between states of different velocities

$$D(k)_B \sim \rho(k) \exp[-E(k)/kT]$$

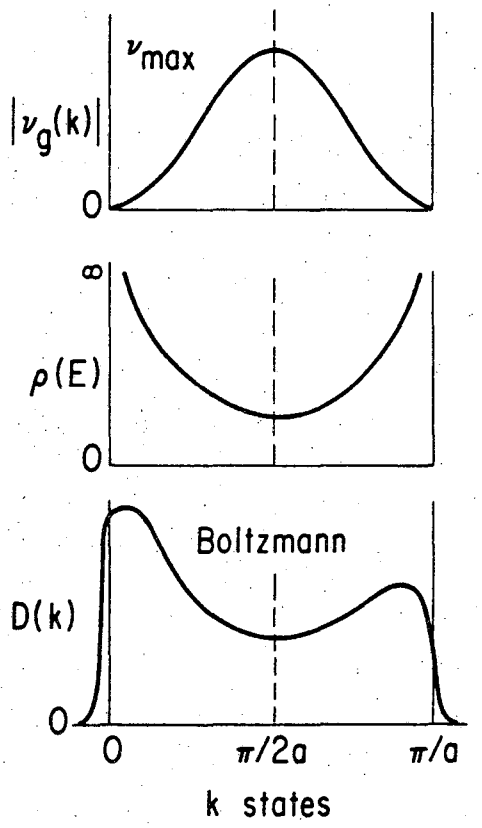

XBL 734-394

Figure 1

from certain k-states, a distinctly non-thermal distribution may result. In either case, it is useful to define the average group velocity $\langle V_g \rangle$ as a statistical average of $V_g(k)$ over this distribution.

It should be noted that the interactions which provide this thermalization mechanism also serve to limit the exciton coherence by limiting the mean free exciton propagation time to some value $\tau(k)$.[16] This scattering also implies a coherence length or mean free path which is given by the distance the excitation travels coherently before being scattered into a new linear combination of k-states with a new group velocity and direction of propagation. As was done with the group velocity, average coherence time τ_c and coherence length $\langle \ell \rangle$ can be used to characterize the dynamics. These quantities are related by

$$\langle \ell \rangle \lesssim \langle V_g \rangle \tau_c. \tag{5}$$

When the coherence length $\langle \ell \rangle$ decreases until it approaches the lattice spacing, a, the delocalized or coherent picture loses its utility. The dynamics begin to approach a random walk limit wherein the excitation is localized and moves from molecule to molecule in a hopping fashion. Thus, a measurement of the coherence length is important in the process of characterizing the coherent nature of exciton propagation. In the experiments described below, measurements of the exciton trapping rate were used to deduce a lower bound for the coherence length in 1,2,4,5-tetrachlorobenzene crystals at liquid helium temperatures. In order to obtain this result from the trapping measurements, the different roles of phonon-exciton scattering, trapping, the mechanisms for detrapping

or promotion of localized excitations to the delocalized states of the exciton band, and the triplet state radiative and nonradiative depopulating channels must be considered. It is also important to examine the role temperature plays in determining the dynamics.

In the coherent limit the rate at which mobile excitons are localized by a trap site (trapping rate constant) is given for one dimensional systems by the expression

$$K_i = \alpha \, (\langle V_g \rangle / d) \qquad (6)$$

where d is the average distance between traps, and i indicates that the excitation is going into the trap.

This is a temperature dependent quantity due to the presence of $\langle V_g \rangle$. The values of $\langle V_g \rangle$ vary only weakly with temperature between 1° and 4° K when the exciton bandwidth is less than 5 cm^{-1}, whereas it may change by a factor of two in the same temperature range for bandwidth of 25 cm^{-1}. Clearly, it is conceivable that not every exciton-trap encounter need lead to trapping of the exciton. The constant α represents the probability that such an encounter actually results in localization of the excitation on the trap molecule. This probability is presumably related to the exact form of the linear combination of k-states which makes up the exciton, the length of time the exciton interacts with the trap, and the availability of a channel or channels for dissipation of the trap-exciton energy difference in the form of phonons. In view of little or no information related to these details, the magnitude of α is difficult to estimate.

On the other hand, the localized limit is characterized by a frequency of exciton-phonon scattering which is much greater than the nearest neighbor interaction ($\beta/\hbar$). In this case, one expects that the exciton migration will be characterized by a random walk or hopping motion with the step length equal to the intermolecular spacing, a, and with the average time per step given by $t = h/4\beta$, where β is the is the intermolecular interaction matrix element. This picture results in a trapping rate constant (the inverse of the average time to reach a trap) on the order of

$$K_i = a^2/td^2 \tag{7}$$

which is <u>independent</u> of temperature. It should be mentioned that the value of β which is appropriate in the localized picture may be much smaller than in the delocalized limit. This results from an increased effective mass due to the lattice distortion which may accompany localization of the exciton.[3] This has the effect of <u>reducing</u> K_i in this limit.

In the intermediate regime where exciton-phonon scattering is of insufficient frequency to completely localize the excitation but does serve to diminish the coherence time of the exciton, the effect of this interaction must be included in an estimation of K_i. For example, a simple model is to assume that the exciton migration can be characterized by a random walk motion with a step length equal to the average coherence length $\langle \ell \rangle$, and a step time given by τ_c. With these assumptions and eq. (5) one obtains

$$K_i = \alpha \langle \ell \rangle^2 \tau_c d^2 \leq (\langle V_g \rangle/d)(\langle \ell \rangle/d) . \tag{8}$$

The important point to note is that the measurement of the trapping or localization rate constants provides a method of determining whether or not coherence is an important consideration in energy transfer processes and to determine a semiquantitative value for the coherence length. To this end, short light pulses (~ 5 nsec) obtained from a tunable dye laser have been utilized to selectively excite band or localized states of one-dimensional systems while monitoring the time dependence of the light emitted from the various states. Although this experimental approach would apply equally well to systems of higher dimensionality, the choice of the simple systems, 1,2,4,5-tetrachlorobenzene (TCB) and 1,4-dibromonaphthalene (DBN), serves to give an ideal case because both TCB[9] and DBN[17,18] have been shown to exhibit behavior characteristic of essentially one-dimensional triplet excitons at liquid helium temperatures. This interesting situation is due to the crystal structures of these materials which result in strong intermolecular interactions in only one direction in the crystal. The interpretation is therefore simplified in that the group velocity and coherence time directly reflect the in-chain dynamics of the exciton.

II. Experimental

A. Sample preparation

DBN was purchased from Eastman Organic Chemicals and zone refined for 125 passes at 1 in./hr. TCB obtained from Eastman was vacuum sublimed into a zone-refining tube and zone refined to 1800 passes. Both crystals were then grown from the melt using Bridgman techniques.

B. Experimental arrangement

For temperatures above 4.2°K, the crystals were mounted on a brass holder and placed in a Janis Research Corp. variable temperature dewar where the sample was cooled by a flow of helium vapor. The temperature was monitored using a carbon resistor in contact with the crystal holder and could be regulated to ± 0.05° K. The carbon resistor was calibrated against a lead-germanium thermometer. For temperatures below 4.2°K the sample was immersed directly in the liquid helium bath, either in the Janis dewar or in a homemade dewar where temperatures below 4.2°K were reached by pumping on the helium bath with a Kinney model KTC-21 vacuum pump or a Leybold-Heraus Type DK-200 vacuum pump.

For the time-resolved phosphorescence experiments, the first excited triplet origin or vibronic level was populated with a laser pulse of approximately 5 nsec duration from a Molectron Corp. UV-1000; DL-200 nitrogen laser-dye laser combination. PBD in p-dioxane and coumarin 102 in ethanol were used as the lasing dyes (obtained from Eastman Organic Chemicals) for TCB and DBN, respectively. The population of the triplet exciton or trap levels was monitored via their phosphorescence emission to the ground state origin or vibronic level using a Spex 3/4 m monochrometer and cooled (-20° C) EMI 6256S photomultiplier at right angles to the excitation beam. The phosphorescence signal was time averaged using a Northern NS-575 signal averager or a Biomation model 8100 transient recorder interfaced to the NS-575, depending on the desired time resolution.

For the phosphorescence temperature dependence of TCB, the crystal was excited using a 100 W mercury arc lamp, filtered by a water filter and Schott 3100 Å interference filter. The phosphorescence was scanned

using a 3/4 m Spex monochrometer in second order with a resolution of approximately 0.2 Å at 3131 Å. The temperature was controlled by varying the rate of pumping on the liquid helium and was monitored during the recording of the spectra using the calibrated carbon resistor. Phosphorescence spectra of DBN were recorded in a similar manner.

C. Phosphorescence of TCB

The phosphorescence spectrum of TCB at 1.5° K and at 4.2° K (0,0 origin only) is shown in Fig. 2. At 4.2° K the phosphorescence intensity is essentially due to exciton emission. As the temperature is lowered, the x-trap (spectroscopic trap depth = 21 cm^{-1})[19] population increases until at 1.5° K the x-trap electronic origin emission is roughly 16 times as intense as that of the exciton origin. Although their exact nature is not known, the x-traps are thought to be TCB molecules whose triplet energy is modified due to proximity to an impurity or crystal defect. In addition to the exciton and x-trap electronic origin, several vibrational progressions are observed in the phosphorescence spectra. In particular, for many of the pulsed excitation experiments, emission from the x-trap or exciton b_{2g} vibronic origin was monitored (see Fig. 2).

D. Phosphorescence of DBN

Phosphorescence spectra of DBN consisted of emission due to the exciton[17] and at least five trap states with spectroscopic trap depths of 28 cm^{-1} (Trap I), 38 cm^{-1} (Trap II), 67 cm^{-1} (Trap III), 120 cm^{-1} (Trap IV), and 146 cm^{-1} (Trap V). These observations were identical to those previously reported,[20] with the exception of the 120 cm^{-1} trap.

Figure 2. Phosphorescence spectra of neat 1,2,4,5-tetrachlorobenzene. The exciton origin (0,0) is at 3748 Å and b_{2g} vibronic origin at 3781 Å. The x-trap origin (0,0) is at 3751 Å and the b_{2g} vibronic origin of the x-trap is at 3784 Å. The inset shows the exciton emission at 4.2° K.

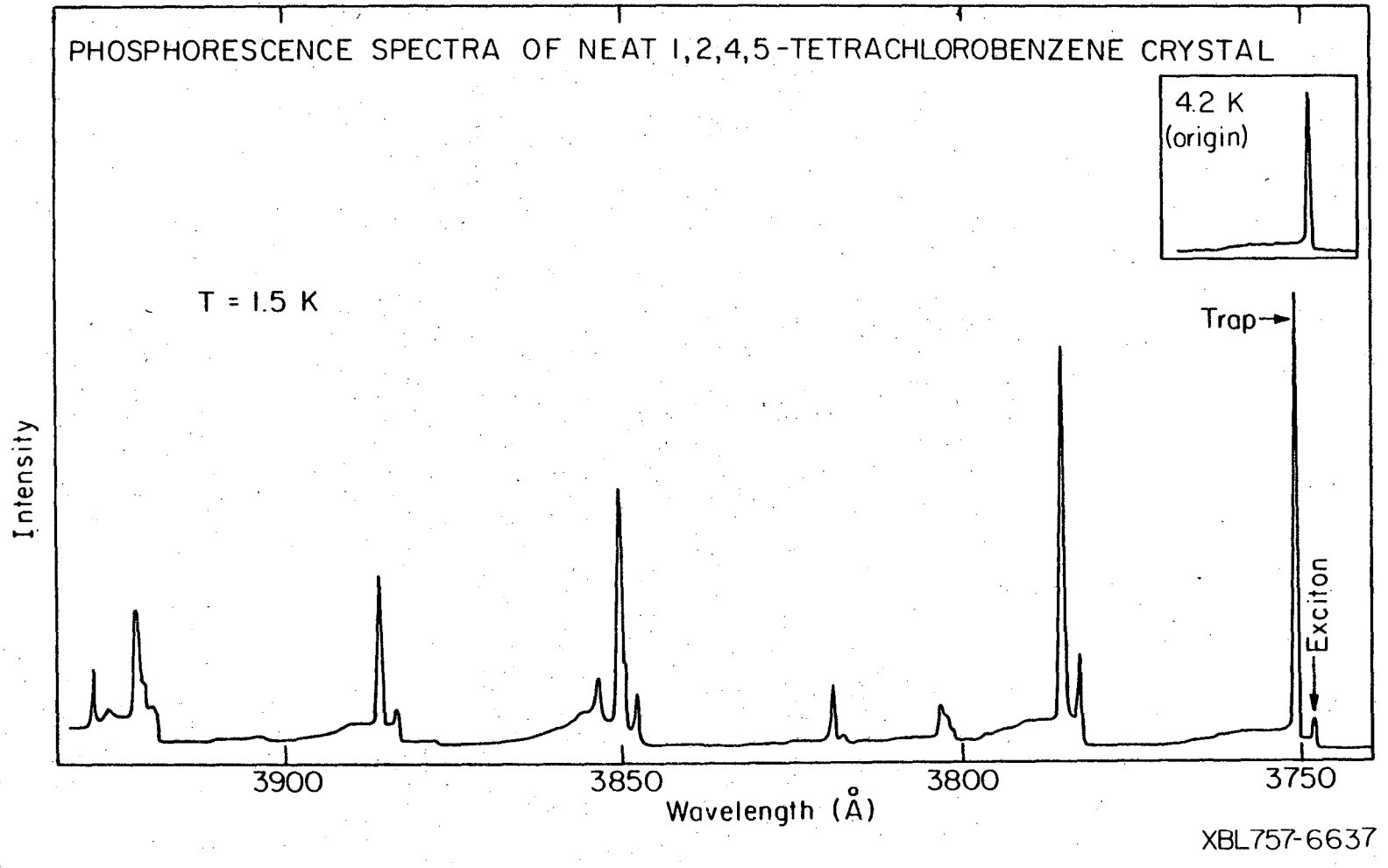
PHOSPHORESCENCE SPECTRA OF NEAT 1,2,4,5-TETRACHLOROBENZENE CRYSTAL
4.2 K
(origin)
T = 1.5 K
Trap
Exciton
Intensity
3900
3850
3800
3750
Wavelength (Å)
XBL757-6637

Figure 2

Above 15° K only exciton emission is observed. As the temperature is lowered, the intensity of this emission increases, and trap emission appears. At 9° K the spectrum consists of emission due to the exciton, Traps IV and V. At 4.2° K Trap III is also seen in emission, and at 3° K emission from all five traps is observed. At 2° K the most intense lines are those due to the two shallowest traps (I and II) and the exciton, the other trap emissions having become weaker. In all the above spectra, the vibronic progression characteristic of DBN was observed.

III. Results and Discussion

A. Kinetic model for coupled band-trap system

The expected phosphorescence response to a short laser pulse will be discussed in terms of the simplest possible kinetic model consisting of a system with a single trap species and an exciton band of N levels.[21] The band and trap levels are coupled with the rate constants K_i and K_0, and the exciton and trap populations decay to the ground state via rate constants K_e and K_t (see Fig. 3). If the processes indicated in Fig. 3 occur among the molecules in the one-dimensional chains and are thus spin independent, the magnetic fine structure of the triplet state plays no role in the kinetics.

The temperature dependence of the kinetics is influenced most strongly by that of the detrapping rate constant K_0. This rate constant has been described and investigated experimentally by Fayer and Harris.[14] According to their model, the magnitude of K_0 at a given temperature will be proportional to the square of the matrix element of the parts of the

Figure 3. Kinetic model for a coupled system of one trap and a one-dimensional triplet exciton band. K_i and K_0 are the trapping and detrapping rate constants, respectively, while K_e and K_t are rate constants for decay to the ground state of the exciton and trap levels, respectively.

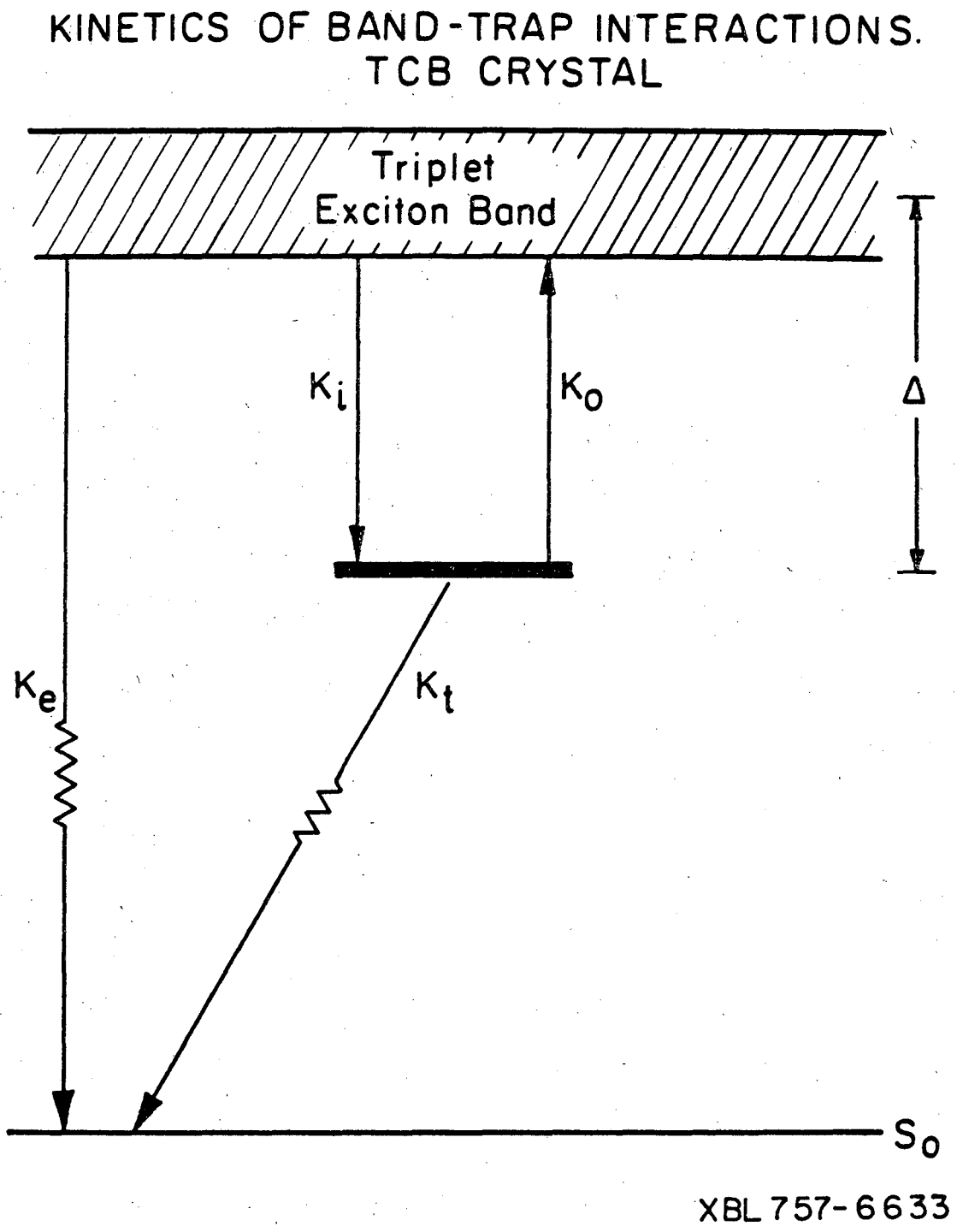
KINETICS OF BAND-TRAP INTERACTIONS.
TCB CRYSTAL
Triplet
Exciton Band
K_i
K_o
Δ
K_e
K_t
S_o
XBL 757-6633

Figure 3

Hamiltonian responsible for the interaction of the trapped excitation with the lattice vibrations ($H_{\tau p}$) and decay of the resulting intermediate into some linear combination of delocalized band states (H_{ie}), weighted by the exciton density of states at the energy of the intermediate $\rho_e(E_i)$. K_0 will also reflect the number of phonons present in the crystal with sufficient energy to mediate the formation of the intermediate state. This phonon distribution will be given by the Planck distribution weighted by the phonon density of states:

$$\langle n(\varepsilon)\rangle = \rho_p(\varepsilon)/[\exp(\varepsilon/kT)-1]\,. \tag{9}$$

The resulting expression must be integrated over all phonon energies greater than or equal to E_i, the energy of the intermediate, and over the values of E_i coincident with the exciton band to give the following expression for K_0:

$$K_0 = \frac{2\pi}{\hbar}\int d\varepsilon\{\rho_p(\varepsilon)/[\exp(\varepsilon/kT)-1]\}\int dE_i\ \rho_e(E_i) \times |\langle \tau, P|H_{\tau p}|i,P'\rangle\langle i,P'|H_{ie}|e,P'\rangle|^2 \tag{10}$$

where the states involved are the trapped excitation plus a phonon state of energy ε, $|\tau,\ P(\varepsilon)\rangle$, the intermediate state of energy E_i plus a phonon of energy $\varepsilon - E_i$, $|i,P'(\varepsilon - E_i)\rangle$, and the linear combination of exciton states which results from the decay of the intermediate, $|e,P'\rangle$. This expression, which includes the interaction of the trap with single phonons only, was obtained from the Golden Rule by summing over all phonons and intermediate states. At low enough temperatures, if the linear portion of the acoustic phonon branch is populated so that ρ_p is essentially constant, and

if $E_i >> kT$, we can write $\langle n(\varepsilon)\rangle \sim \exp(-\varepsilon/kT)$. For intermediates which contribute significantly to K_0 and cover a small energy range compared to the trap depth, one obtains the simple expression for the detrapping rate constant,

$$K_0 = C\,\rho_e(E_i)\,\exp(-E_i/kT) \tag{11}$$

where C is a temperature independent constant. This result would be obtained, for example, if $\rho_e(E)$ is sharply peaked at some energy E_i, if the exciton bandwidth is very narrow compared to the trap depth, or in the case of one-dimensional excitons with a peak in $\rho_e(E)$ at the bottom of the band, if the band is wide compared to kT. The above equation indicates that K_0 will vary radically in the low temperature region (T ~1° to ~10°K) for trap depths on the order of tens of reciprocal centimeters.

The dynamics of the coupled band-trap system can be described with the kinetic equations for N_e and N_t, the number of excitations in the exciton and trap levels.

$$\begin{aligned}\dot{N}_e(t) &= -(K_i + K_e)\,N_e(t) + K_0\,N_t(t)\\ \dot{N}_t(t) &= -(K_t + K_0)\,N_t(t) + K_i\,N_e(t).\end{aligned} \tag{12}$$

In writing these equations, the excited state concentration is taken to be sufficiently small that interactions of the triplet excitations with themselves may be ignored. This precludes such effects as bi-excitonic annihilation. The solutions of these equations are of the form:

$$N_e(t) = N_e^+ \exp(\alpha_+ t) + N_e^- \exp(\alpha_- t)$$
$$N_t(t) = N_t^+ \exp(\alpha_+ t) + N_t^- \exp(\alpha_- t) \quad (13)$$

where

$$\alpha_\pm = \{1/2\}\{-(K_0 + K_i + K_e + K_t) \pm [(K_i + K_e - K_t)^2 + K_0^2 + 2K_0(K_i - K_e + K_t)]^{\frac{1}{2}}\} \quad (14)$$

and N_e^+, N_e^-, N_t^+, and N_t^- are determined by the initial conditons. The initial conditions of interest for the experiments to be described are $N_e(t=0) = N_o$ and $N_t(t=0) = 0$, which results in the following expressions for the populations as a function of time:

$$N_e(t) = N_0\{[(\alpha_- + K_i + K_e)/(\alpha_- - \alpha_+)]\exp(\alpha_+ t) + [(\alpha_+ + K_i + K_e)/(\alpha_+ - \alpha_-)]\exp(\alpha_- t)\} \quad (15)$$

$$N_t(t) = [(K_i N_0)/(\alpha_+ - \alpha_-)][\exp(\alpha_+ t) - \exp(\alpha_- t)] \quad . \quad (16)$$

In order to predict the kinetics of energy transfer, it is useful to graph the decay constants and pre-exponential factors resulting from solution of the above equations as a function of K_0 for various values of the other parameters. From Figs. 4-6, one observes the following behavior. The exciton population decays as a biexponential. It is dominated in the slow-detrapping regime by the fast [$\alpha_- \approx -(K_i + K_e)$] component due to the combined effects of trapping and decay to the ground state, but still exhibits a long ($\alpha_+ = -K_t$) tail of lesser magnitude as a result of some small detrapping rate. In this regime the trap builds up as the exciton decays and then decays with its characteristic decay constant K_t, as

should be noted from eq. (16). In the fast-detrapping regime the triplet population spends little time in the trap, and the decay of the exciton is dominated by the slow component ($\alpha_+ \approx -K_e$) at the decay rate characteristic of the exciton. The trap population is minimal. It builds up very fast ($\alpha_- \approx -K_0$) and then decays with a rate equal to that of the exciton decay owing to the rapid communication with the exciton band.

This model has been presented for the simplest case of a single trap. It should, however, be equally applicable to systems with multiple trap species, although a cubic or higher order equation for the decay constants will result. While this is not particularly formidable, extraction of the parameters K_i, K_0, etc., from experimental data may be more difficult.

One can also use this simple model to calculate the expected steady-state populations under conditions of continuous illumination. If population is fed to the exciton band with constant rate R, the kinetic equations in the steady state become

$$\begin{aligned} \dot{N}_e(t) &= 0 = R - N_e(K_e + K_i) + N_t(K_0) \\ \dot{N}_t(t) &= 0 = -N_t(K_0 + K_t) + N_e(K_i). \end{aligned} \tag{17}$$

The solutions are given by

$$N_t = K_i\, R/(K_eK_0 + K_eK_t + K_iK_t) \tag{18}$$

and

$$N_e = (K_0 + K_t)\, R/(K_eK_0 + K_eK_t + K_iK_t). \tag{19}$$

A useful ratio which gives the fraction of trap population is

$$N_t/(N_e + N_t) = 1/[1 + (K_0/K_i) + (K_t/K_i)]. \tag{20}$$

Figure 4. Prediction of the kinetic model for the variation of α_- (the fast exciton decay component and trap build-up rate) with detrapping rate constant. The curves correspond to different values of K_i, the trapping rate constant.

Figure 5. Prediction of the kinetic model for the variation of α_+ (exciton and trap decay rate) with the detrapping rate constant for different values of the trapping rate constant.

Figure 6. Prediction of the kinetic model for the magnitude of the fast component of the exciton decay compared with the initial exciton population N_0. The functional dependence of the ratio N_e^-/N_0 on the detrapping rate constant is displayed for different values of the trapping rate constant.

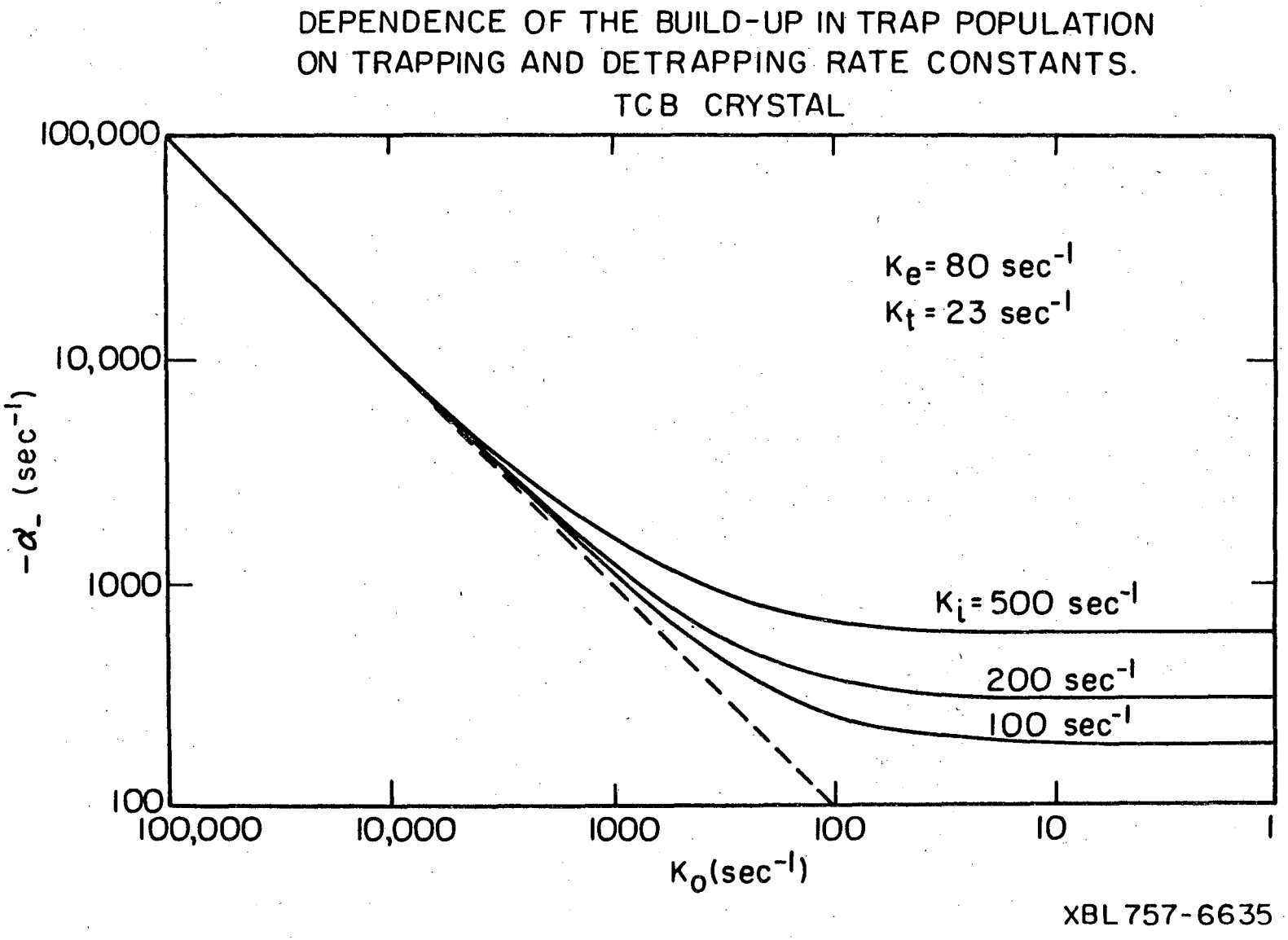
DEPENDENCE OF THE BUILD-UP IN TRAP POPULATION
ON TRAPPING AND DETRAPPING RATE CONSTANTS.
TCB CRYSTAL
100,000
10,000
1000
100
$-\alpha_-$ (sec^{-1})
K_e= 80 sec^{-1}
K_t = 23 sec^{-1}
K_i= 500 sec^{-1}
200 sec^{-1}
100 sec^{-1}
100,000
10,000
1000
100
10
1
K_o(sec^{-1})
XBL 757-6635

Figure 4

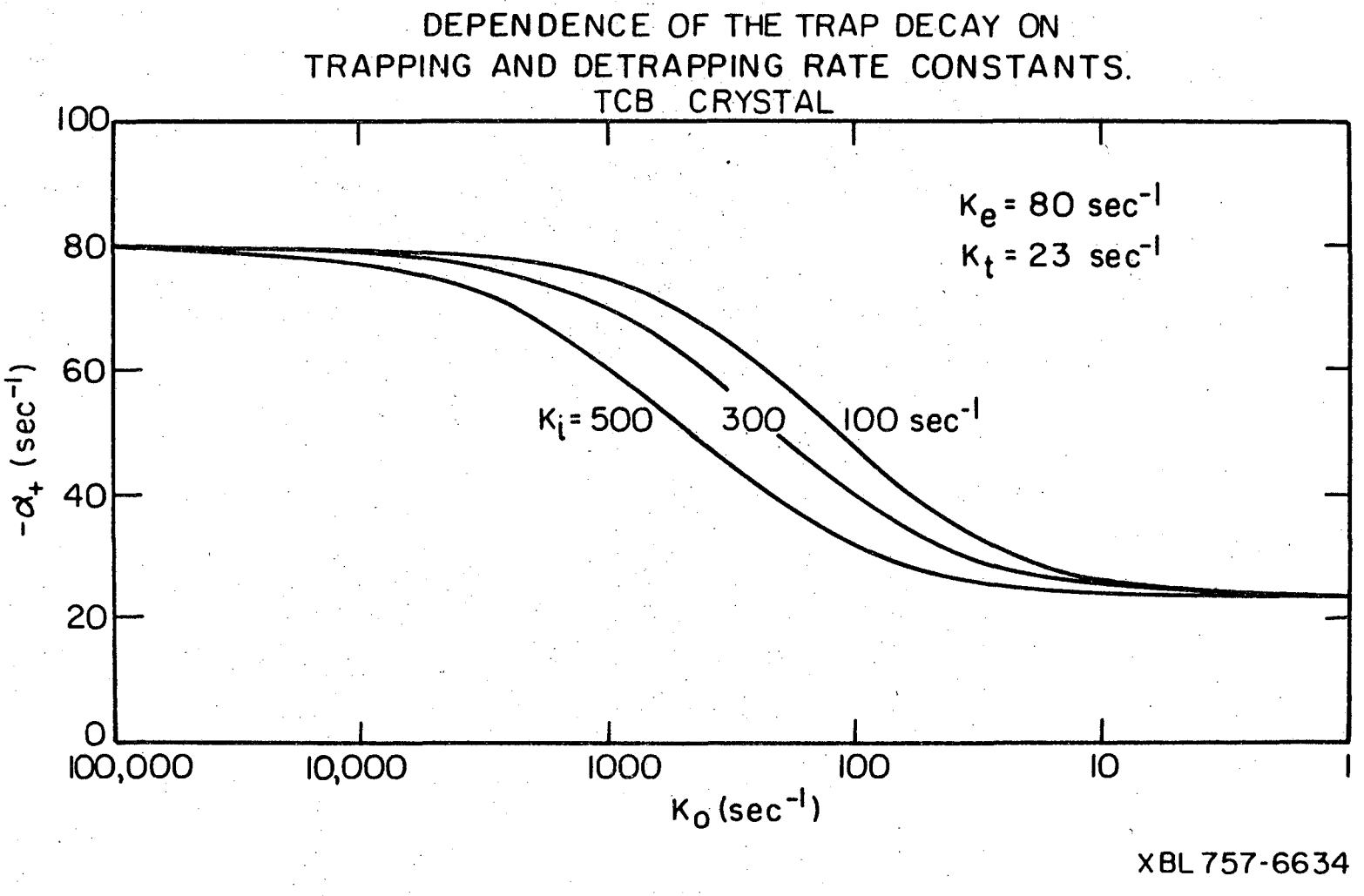
DEPENDENCE OF THE TRAP DECAY ON
TRAPPING AND DETRAPPING RATE CONSTANTS.
TCB CRYSTAL
K_e = 80 sec^{-1}
K_t = 23 sec^{-1}
K_i = 500
300
100 sec^{-1}
$-\alpha_+$ (sec^{-1})
100
80
60
40
20
0
100,000
10,000
1000
100
10
1
K_0 (sec^{-1})
XBL 757-6634

Figure 5

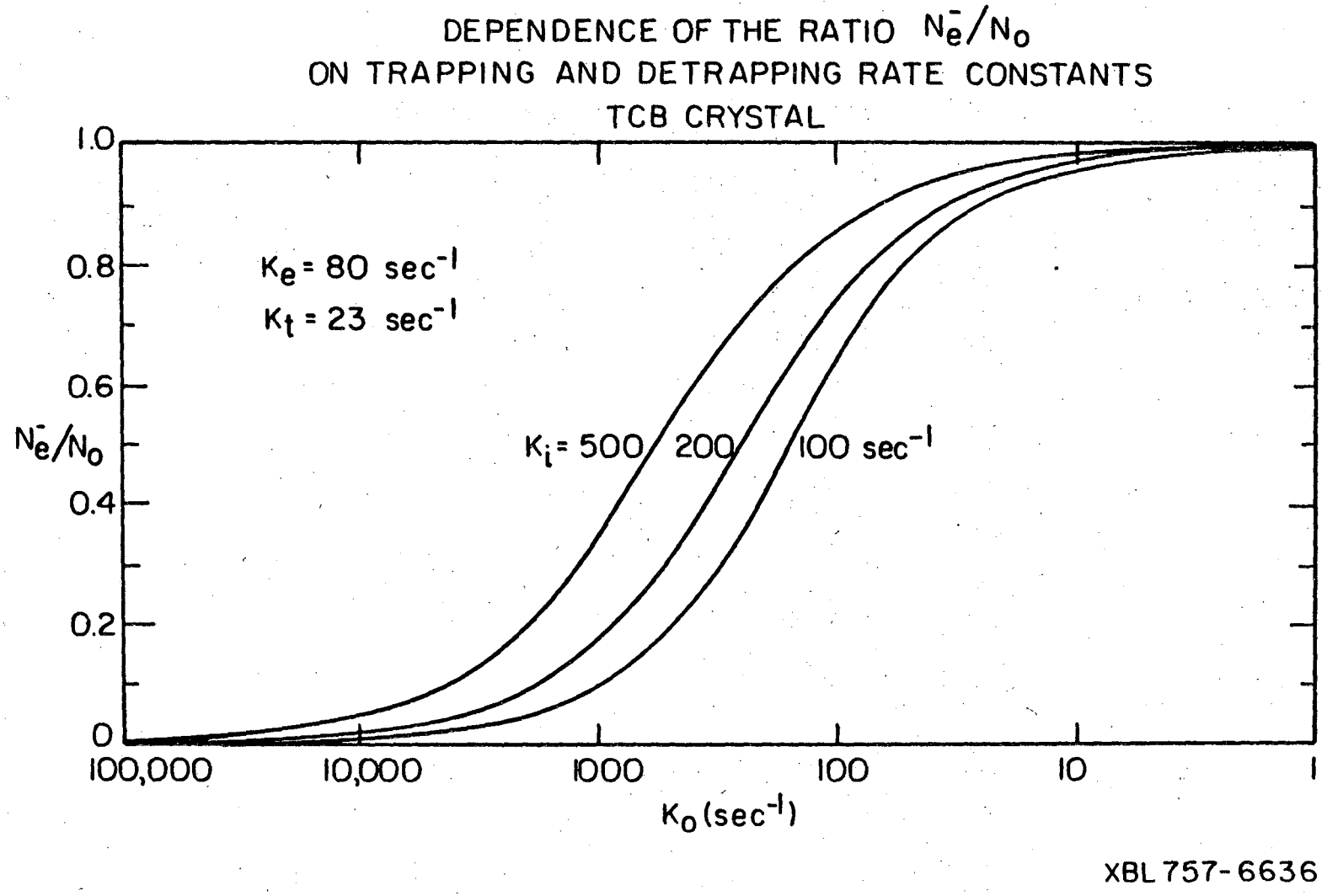
DEPENDENCE OF THE RATIO N_e^-/N_o
ON TRAPPING AND DETRAPPING RATE CONSTANTS
TCB CRYSTAL
1.0
0.8
0.6
0.4
0.2
0
N_e^-/N_o
$K_e = 80\ sec^{-1}$
$K_t = 23\ sec^{-1}$
$K_i = 500$ 200 100 sec^{-1}
100,000
10,000
1000
100
10
1
$K_o (sec^{-1})$
XBL 757-6636

Figure 6

In the Boltzmann regime, this ratio will be determined by the one excitation partition function of the system[7] (single trap and N exciton levels), i.e.,

$$N_t/(N_e + N_t) = \exp[- E_{trap}/kT] / Z \tag{21}$$

and

$$Z = \exp[- (E_{trap}/kT)] + \sum_k \exp[- E(k)/kT]. \tag{22}$$

If Δ is the trap depth below the $k = 0$ level of a one-dimensional exciton band, $E(k)$ takes the simple form in eq. (3) and Z is given by

$$Z = \exp[- (2\beta - \Delta) / kT] + \sum_k \exp[- (2\beta / kT) \cos ka] \tag{23}$$

where the sum is over the N exciton band levels, and the zero of energy is taken as the center of the exciton band. This result [eqs. (21) and (23) is to be compared with eq. (20) under the condition necessary to produce thermal equilibrium among the trap and band states, namely that the excitation sample both band and trap states with sufficient rapidity that equilibrium can be attained during its lifetime. In other words, K_0 and $K_i >> K_t$ and K_e, and therefore

$$K_0 / K_i >> K_t / K_i. \tag{24}$$

As noted in eq. (11), K_0 can be approximated as

$$K_0 \alpha N \exp(- \Delta/kT) \tag{25}$$

where the density of exciton states is replaced by the number of exciton levels, N. If the system is in Boltzmann equilibrium, it must be true

that $K_0/K_i = N_e/N_t = N \exp(-\Delta/kT)$. Thus, eq. (20) becomes

$$N_t/(N_e + N_t) = 1/[1 + N \exp(-\Delta/kT)] \quad (26)$$

which is equivalent to eq. (21) if the bandwidth is small compared to the trap depth, i.e., $4\beta << \Delta$. In fact, the parameters of the model do not include the bandwidth, and k-dependent processes are not considered. It is therefore expected to be most applicable in the narrow band and/or large trap depth limits.

B. Experimental determination of the kinetic parameters

1,4-Dibromonaphthalene

Pulse excitation-time resolved phosphorescence measurements of build-up and decay rates for the trap states in DBN were made at several temperatures from 2°K to 9°K. The results of these measurements using an excitation wavelength of 4789 Å (688 cm^{-1} above the exciton origin) are shown in Fig. 7.

The behavior of the phosphorescence response from some of the traps qualitatively conforms to that predicted by the kinetic model. At 2° K, Traps I, II, and IV all exhibit phosphorescence which builds up at the exciton decay rate and decays at the trap decay rate. At 3° K similar behavior is observed, except for Trap I, which has shortened decay rate. At 4.2° K, detrapping from Traps I and II is sufficiently rapid that the build-up rate is extremely fast and the decay rate is that of the exciton, indicating that complete equilibration of the traps and band has taken place. However, the detrapping rate from Trap IV is not sufficient to produce similar behavior either at 4.2° K or at 9° K, and

Figure 7. This figure shows the build-up (circles) and decay (dots) rates for the exciton and trap populations in neat 1,4-dibromonaphthalene as a function of trap depth at four different temperatures. The excitation wavelength was 4789 Å. The dashed lines indicate the exciton decay constants for comparison with the trap constants.

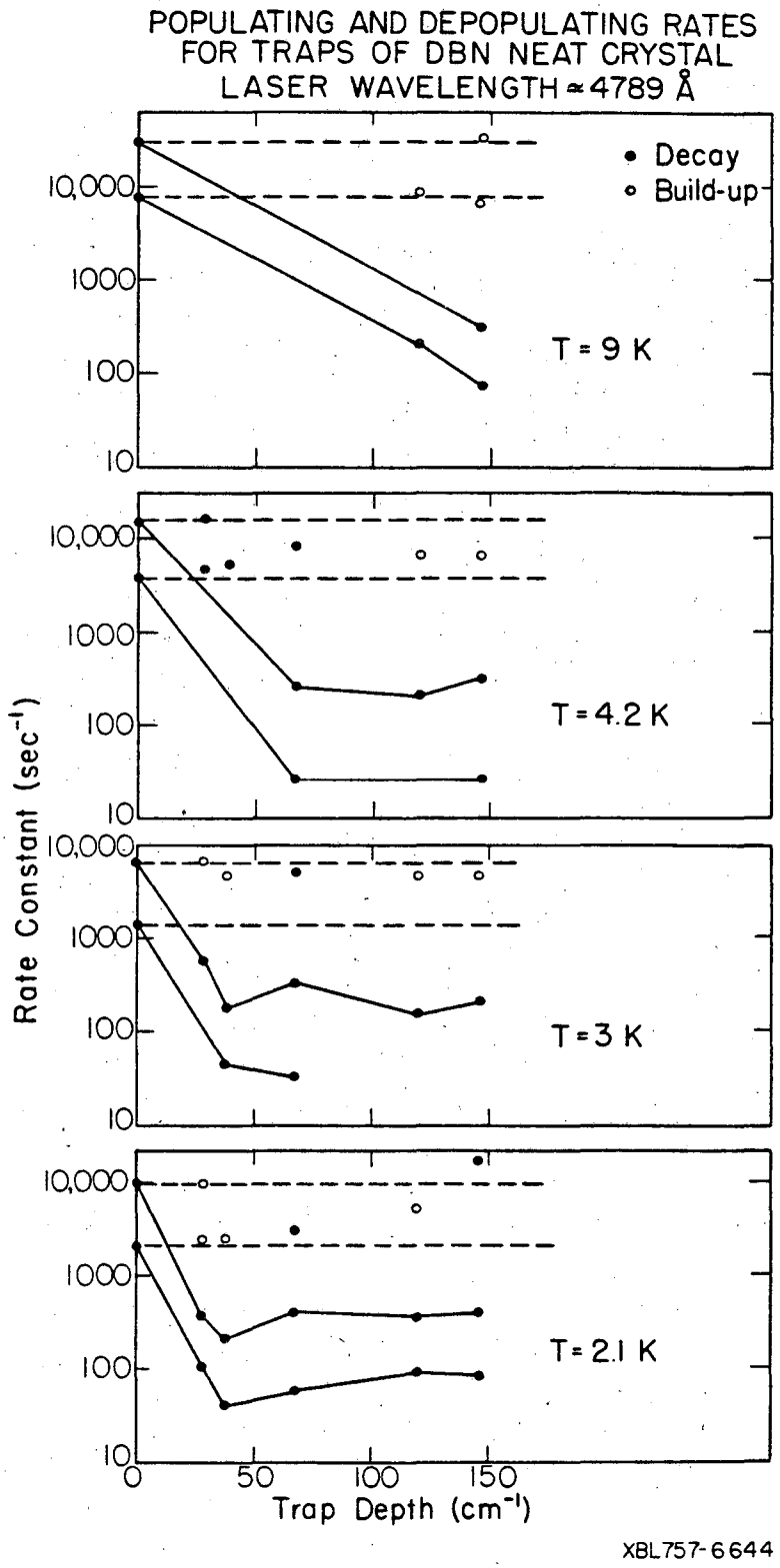
POPULATING AND DEPOPULATING RATES
FOR TRAPS OF DBN NEAT CRYSTAL
LASER WAVELENGTH ≃ 4789 Å
• Decay
○ Build-up
T = 9 K
T = 4.2 K
T = 3 K
T = 2.1 K
Rate Constant (sec⁻¹)
10,000
1000
100
10
0
50
100
150
Trap Depth (cm⁻¹)
XBL757-6644

Figure 7

the trap build-up rate is equal to the exciton decay rate. These features of the band-trap equilibria appear to be qualitatively consistent with the simple viewpoint and model presented above.

However, there are some difficulties with the interpretation of certain other qualitative features. A build-up of Trap III phosphorescence was not observed at any temperature. Population appeared very quickly (within 1 μsec) and three decay components were observed, one with a decay rate similar to the exciton, and two with decay rates similar to those of other traps. On the other hand, Trap V seems to behave as expected except at 2°K, where the build-up becomes very fast, in contrast to its behavior at higher temperatures. Thus, the extraction of specific information relating the exciton dynamics to the observed phosphorescence response is difficult within the context of this unsophisticated model owing to the increased complexity of the DBN band-trap system compared to TCB. However, the observed transient and steady state phosphorescence behavior clearly shows that communication between the exciton band and the traps does exist, and that it takes place on a timescale which is considerably shorter in some cases than the exciton phosphorescence decay time. Thus, it is important to interpret investigations of exciton dynamics in terms of a coupled band-trap system and not ignore the effect of the traps.

The original purpose of this investigation was to use the band-trap equilibrium as a probe of the exciton dynamics. In the case of DBN, the simple model which has been adopted is incapable of completely describing this complex multiple trap system. It is therefore not possible to demonstrate the importance of coherence in this system with this approach. Such is not the case, however, with the simpler TCB system.

1,2,4,5-Tetrachlorobenzene

Direct laser excitation of the triplet exciton origin in TCB resulted in the exciton and x-trap phosphorescence response shown in Figs. 8 and 9 for temperatures of 1.25°K and 4.2°K. The system clearly exhibits the general features of our kinetic model for a coupled band-trap system. At 4.2°K, phonon-assisted promotion (detrapping) of a trapped excitation to the exciton band is rapid; both exciton and trap populations decay at a rate which is characteristic of the exciton, and the build-up of the trap phosphorescence is very fast. In the slow-detrapping regime (1.25°K), the trap population builds up as the exciton decays, and it then decays with a rate constant characteristic of the trap excited triplet lifetime. The exciton decay rate reflects the exciton lifetime and the trapping rate.

Such measurements have been made over a range of temperatures, and the time-resolved phosphorescence decay was decomposed into a sum of exponentials. Build-up and decay rates as well as the relative intensity of each exponential component were then obtained as a function of temperature. These data for the TCB neat crystal are shown in Tables I, II, and III. The rate constants are listed as a function of temperature for excitation wavelengths corresponding to the exciton origin and two shorter wavelengths. By relating this temperature dependence to that predicted by the model, the rate constants, K_0, K_i, K_e, and K_t, can be determined and related to the energy transfer dynamics in the crystal.

The fitting of the calculated temperature dependence to the experimental data was approached from two directions. First, K_e and K_t were estimated from the high and low temperature limits of the trap and/or exciton decay rates. K_i was estimated from the trap build-up rate in

Figure 8. Phosphorescence response of neat TCB to pulsed laser excitation in the low temperature-slow detrapping regime. Note that the exciton decay and trap build-up rates are similar. Excitation was to the exciton (0,0) origin (3748 Å).

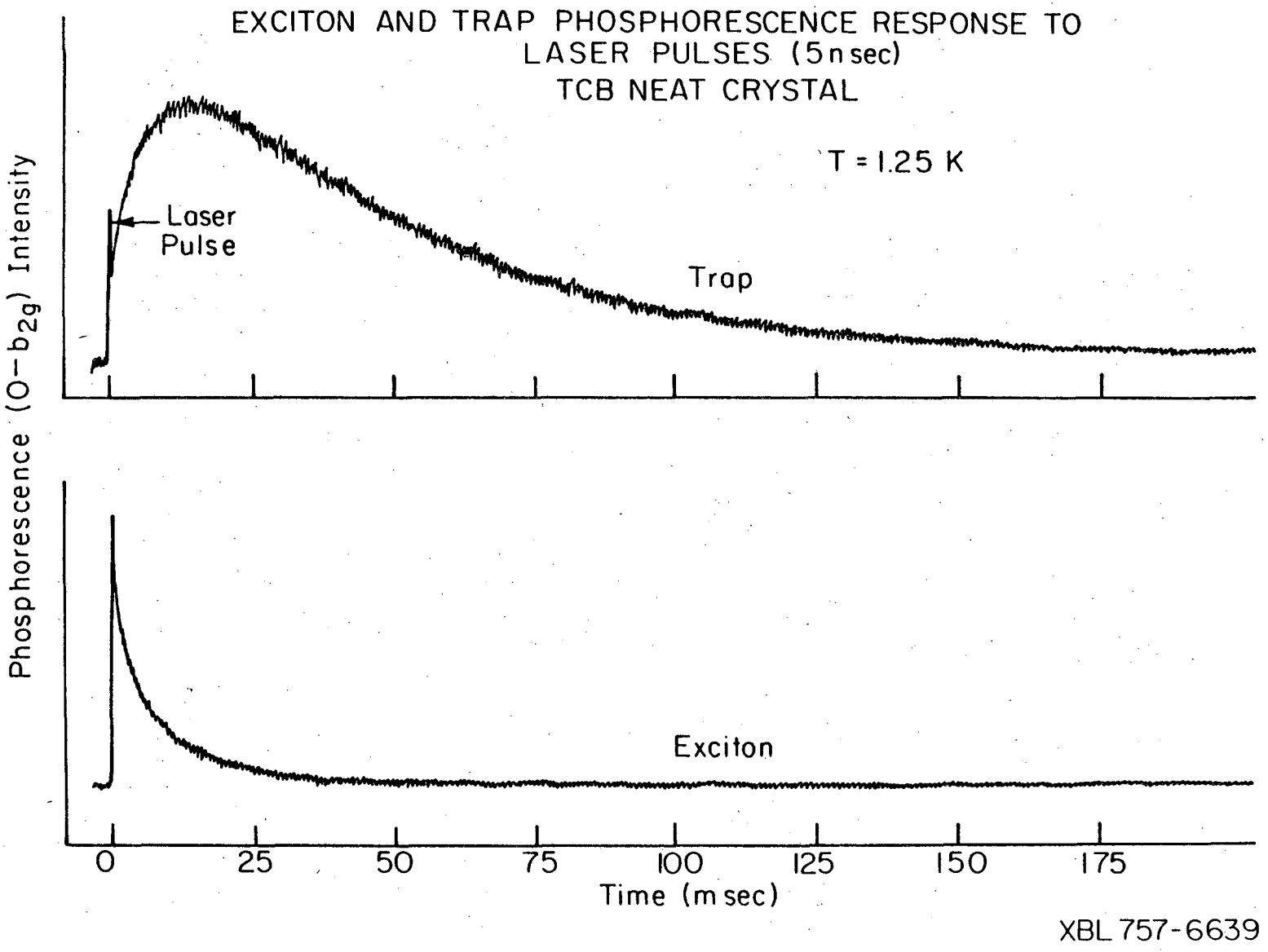
EXCITON AND TRAP PHOSPHORESCENCE RESPONSE TO
LASER PULSES (5 n sec)
TCB NEAT CRYSTAL
T = 1.25 K
Laser
Pulse
Trap
Exciton
Phosphorescence (O-b2g) Intensity
0
25
50
75
100
125
150
175
Time (m sec)
XBL 757-6639

Figure 8

Figure 9. Phosphorescence response of neat TCB to pulsed laser excitation in the high temperature-fast detrapping regime. Note that the exciton and trap decay at the same rate and that the trap build-up is too fast to be observed on this time scale. Also note that the trap emission is very weak. Excitation was to the exciton (0,0) origin (3748 Å)

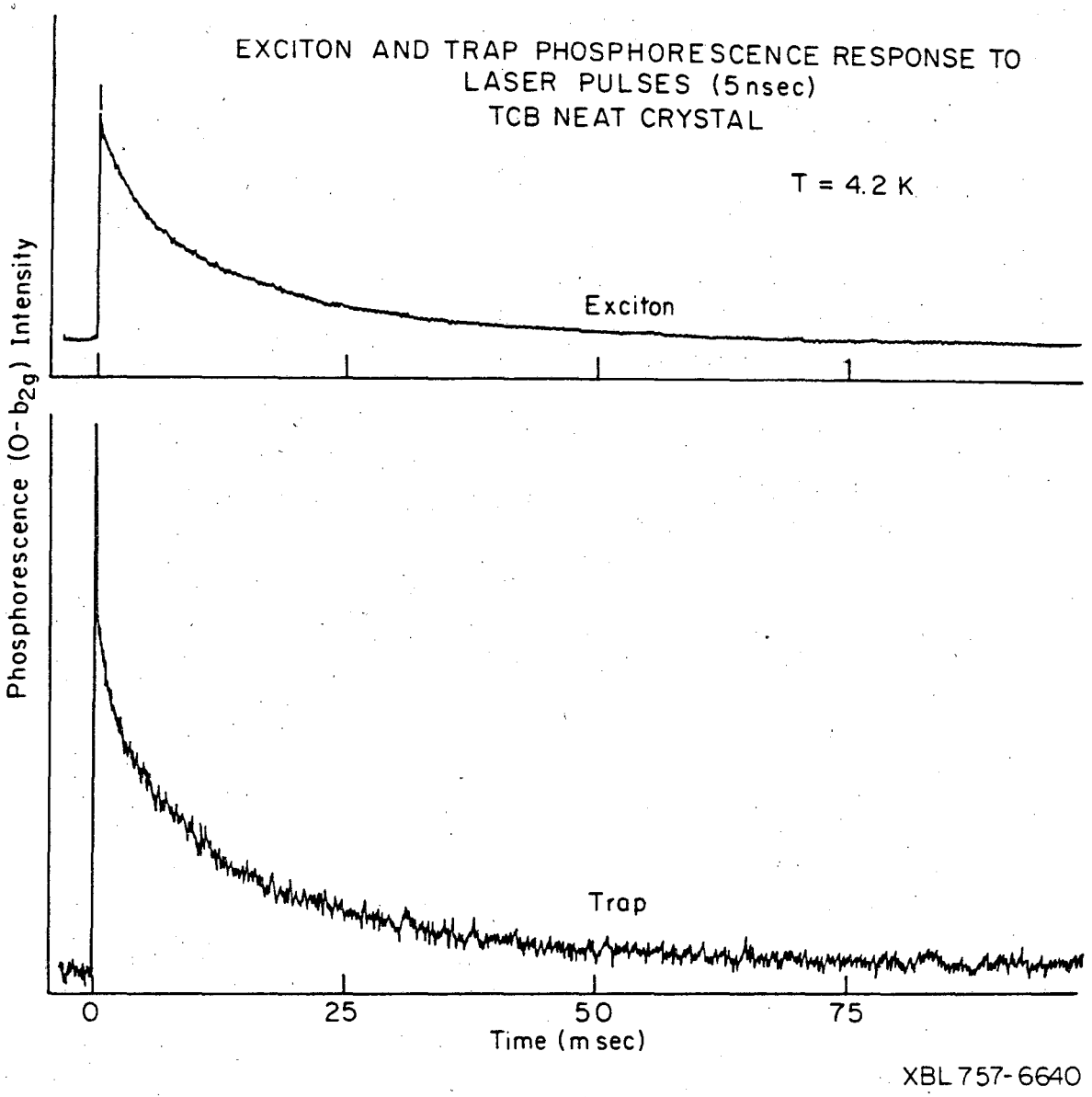
EXCITON AND TRAP PHOSPHORESCENCE RESPONSE TO
LASER PULSES (5nsec)
TCB NEAT CRYSTAL
T = 4.2 K
Exciton
Trap
Phosphorescence (O-b2g) Intensity
0
25
50
75
Time (msec)
XBL 757-6640

Figure 9

TABLE I. Phosphorescence build-up and decay rate constants for neat TCB: excitation wavelength = 3748 Å [exciton origin (0,0)].

Temperature (°K)	Exciton decay rates b_{2g} origin $(sec^{-1})^a$		α Trap (b_{2g} origin) buildup (sec^{-1})	Decay $(sec^{-1})^a$	
1.25	104	(1)	128	22.5	
	884	(0.69)			
1.50	23.3	(0.09)	204	25.2	
	166	(1)			
1.75	16.0	(0.05)	254	25.8	
	216	(1)			
2.00	17.8	(0.10)	354	26.6	
	283	(1)			
2.25	17.3	(0.34)	453	13.5	(0.53)
	62.9	(0.25)		44.7	(1)
	476	(1)			
2.50	265	(1)	1480	18.2	(0.46)
	843	(0.71)		47.3	(1)
2.75	20.3	(0.97)	4123	33.7	
	53.8	(1)			
	1180	(0.76)			
3.00	23.9	(1)	---	26.7	(1)
	65.1	(1)		106	(0.89)
3.25	23.5	(0.69)	---	19.4	(0.5)
	71.4	(1)		79.0	(1)
3.50	22.5	(0.59)	---	26.3	(0.8)
	70	(1)		137	(1)
3.75	36.7	(1)	---	33.7	(0.72)
	135	(0.78		169	(1)
4.00	37.9	(1)	---	51.9	
	128	(0.91)			
4.20	35.2	(0.72)	---	46.7	(1)
	158	(1)		239	(0.87)

[a] Numbers in parentheses give the relative intensity corresponding to each decay component (pre-exponential factor).

TABLE II. Phosphorescence decay and build-up rate constants for neat TCB: excitation wavelength = 3733 Å [108 cm^{-1} above exciton (0,0)].

Temperature (°K)	Exciton Decay Rates (sec^{-1})				x-Trap Rates (sec^{-1})			
					b_{2g} Origin		(0,0) Origin	
	b_{2g} Origin		(0,0) Origin		Buildup	Decay[a] (sec^{-1})	Buildup	Decay[a] (sec^{-1})
22.5	255	(0.36)						
	990	(1)						
10.45	103	(0.29)						
	467	(1)						
8.0	99.8	(1)	439					90.5 (0.86)
	681	(0.69)						599 (1)
4.2	46	(1)	42.7	(1)				52.3
	170	(0.13)	265	(0.18)				
2.8	26.9	(1)	34.7	(1)	5540	30	3090	36.2
	84.3	(0.44)	130	(0.34)				
	4000	(0.67)						
2.1	29.6	(0.17)	44.4	(0.18)	349	33.1	378	32
	406	(1)	317	(1)				
	6185	(0.72)	1855	(0.38)				

[a] Numbers in parentheses give the relative intensity corresponding to each decay component (preexponential factor).

TABLE III. Phosphorescence decay and build-up rate constants for neat TCB: excitation wavelength = 3744 Å [26 cm^{-1} above exciton (0,0)].

Temperature (°K)	Exciton Decay Rates[a] (sec^{-1})				x-Trap Rates (sec^{-1})			
	b_{2g} Origin		(0,0) Origin		b_{2g} Origin		(0,0) Origin	
					Buildup	Decay[a]	Buildup	Decay[a]
4.2	27.9 75.7	(0.62) (1)	28.1 79.0	(0.57) (1)				
1.25			67.5 273	(0.86) (1)	133	20.6	128	21.2

[a] Numbers in parentheses give the relative intensity corresponding to each decay component (pre-exponential factor).

the low temperature limit. A curve for N_e^- as a function of K_0 was then calculated, and the value of K_0 corresponding to each temperature was found by matching the experimental values of N_e^- to this curve. A plot of $\ln K_0$ vs 1/T then gives ΔE, the effective energy difference between the localized trap state and the states to which detrapping is taking place. Also this allows calculation of α_+ and α_- to be made and compared with the experimental data. The various parameters are then adjusted for the best overall fit. This procedure gives $K_e = 80\ \text{sec}^{-1}$, $K_t = 23\ \text{sec}^{-1}$, $K_i = 250\ \text{sec}^{-1}$, and $\Delta E = 15\ \text{cm}^{-1}$. The fits to the experimental data and the plot of K_0 vs 1/T are shown in Figs. 10-12 (solid curves).

The second approach to fitting the data was based on the fact that the trap build-up rate α_- approaches the detrapping rate constant K_0 in the high temperature limit. Thus, a straight line through this region of the experimentally determined values of α_- directly gives K_0 vs 1/T and a value of $\Delta E = 20\ \text{cm}^{-1}$. The best fit to N_e^- and α_- is obtained with $K_e = 80\ \text{sec}^{-1}$, $K_t = 23\ \text{sec}^{-1}$, and $K_i = 150\ \text{sec}^{-1}$ (see Fig. 12, dotted curve).

It must be noted that while the model calculations predict very little variation of α_- with 1/T in the low temperature limit, the experimental values slowly increase with increasing temperatures. One possible source of this discrepancy is an increasing value of the exciton decay constant K_e with temperature. In fact, from Table II one can see that the exciton decay constant(s) does continue to increase with temperature above 4.2°K where only exciton emission is observed. This effect could, for example, be the result of a thermally activated nonradiative

Figure 10. Calculated fits to experimental data for the ratio N_e^-/N_0. The solid curve corresponds to the best fit for N_e^-/N_0, and gives the values of K_0 vs 1/T shown in Fig. 11. The dotted curve corresponds to values of K_0 obtained from the plot of α_- vs 1/T (see Fig. 12).

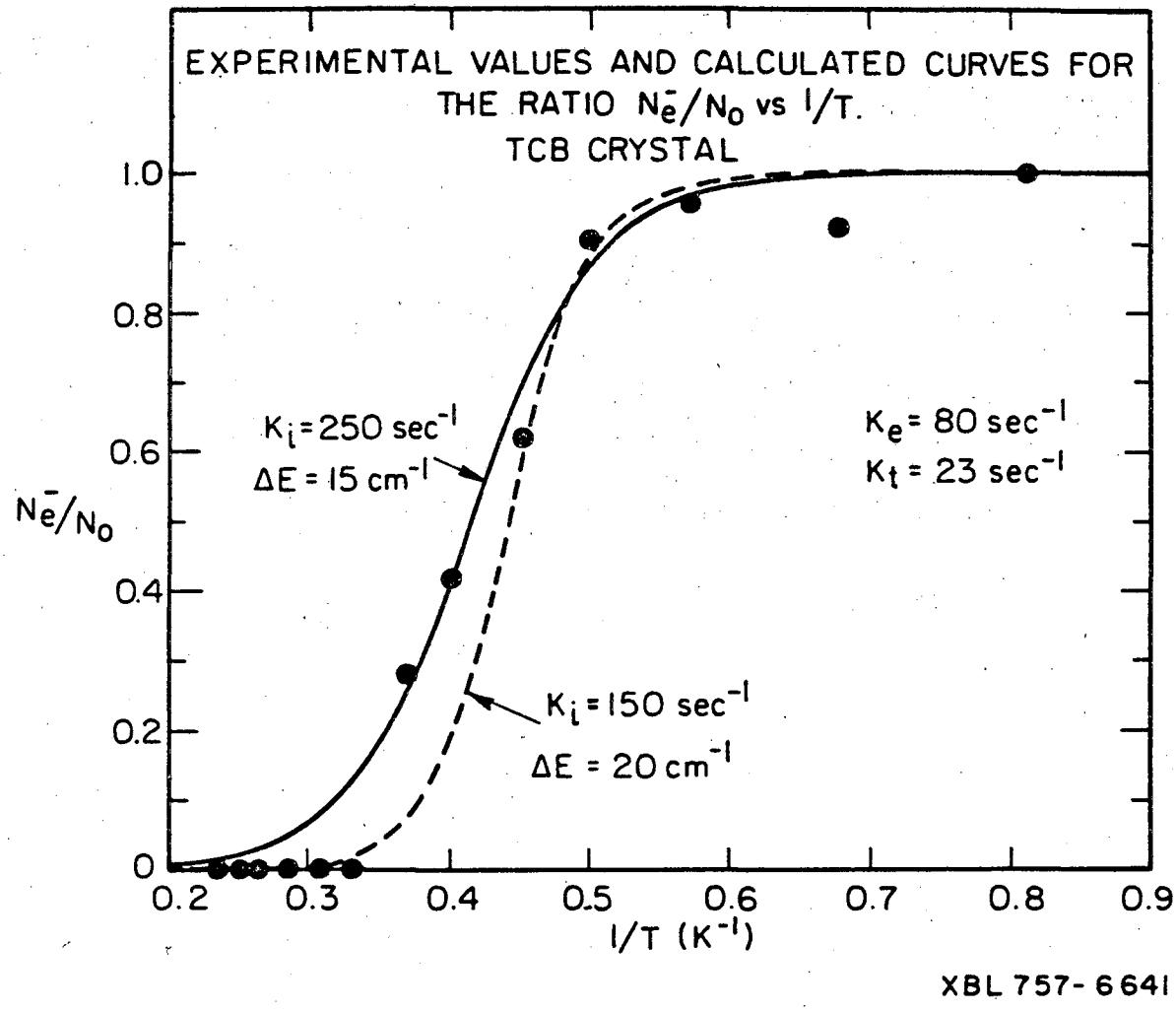
EXPERIMENTAL VALUES AND CALCULATED CURVES FOR
THE RATIO N_e^-/N_0 vs $1/T$.
TCB CRYSTAL
$K_i = 250\ sec^{-1}$
$\Delta E = 15\ cm^{-1}$
$K_e = 80\ sec^{-1}$
$K_t = 23\ sec^{-1}$
$K_i = 150\ sec^{-1}$
$\Delta E = 20\ cm^{-1}$
N_e^-/N_0
1.0
0.8
0.6
0.4
0.2
0
0.2
0.3
0.4
0.5
0.6
0.7
0.8
0.9
$1/T\ (K^{-1})$
XBL 757-6641

Figure 10

Figure 11. Detrapping rate constant vs 1/T obtained from the solid curve in Fig. 10 and calculations based on the kinetic model: ΔE represents the energy difference between the trap level and the intermediate which is assumed to be active in mediating phonon-assisted detrapping.

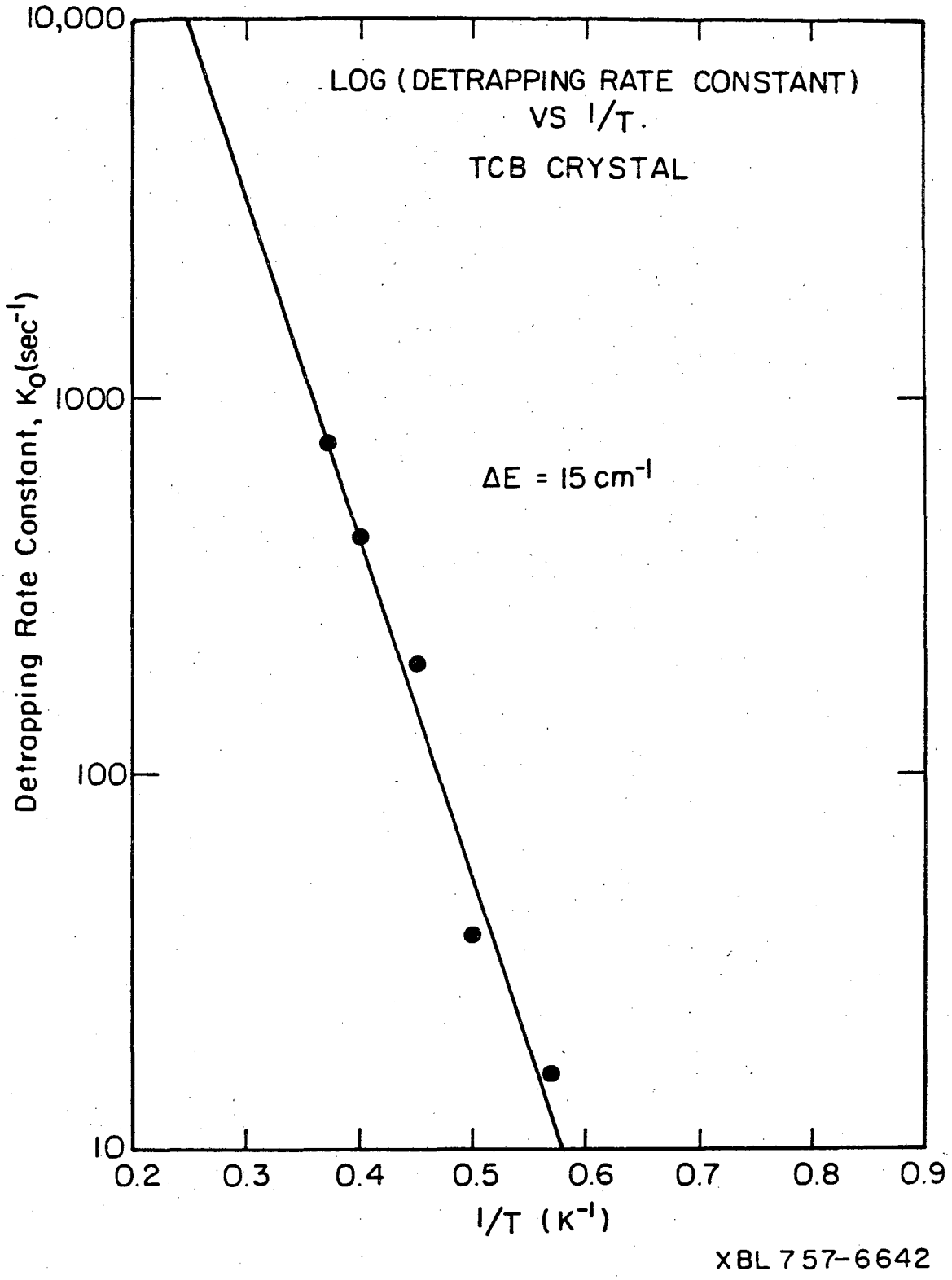
LOG (DETRAPPING RATE CONSTANT)
VS 1/T.
TCB CRYSTAL
ΔE = 15 cm⁻¹
Detrapping Rate Constant, K₀(sec⁻¹)
10,000
1000
100
10
0.2
0.3
0.4
0.5
0.6
0.7
0.8
0.9
1/T (K⁻¹)
XBL 757-6642

Figure 11

Figure 12. Calculated fits to the data for α_- vs 1/T. The solid curves were calculated from the model equation using the values of K_0 vs 1/T from Fig. 11. The curve for K_i = 125 sec^{-1} corresponds to $K_e = K_t$ = 23 sec^{-1} rather than the values shown in the figure. The dotted curve is the best fit to α_-, and the corresponding values of K_0 vs 1/T were used to calculate the dotted curve in Fig. 10. These latter calculations give a value of ΔE of 20 cm^{-1}.

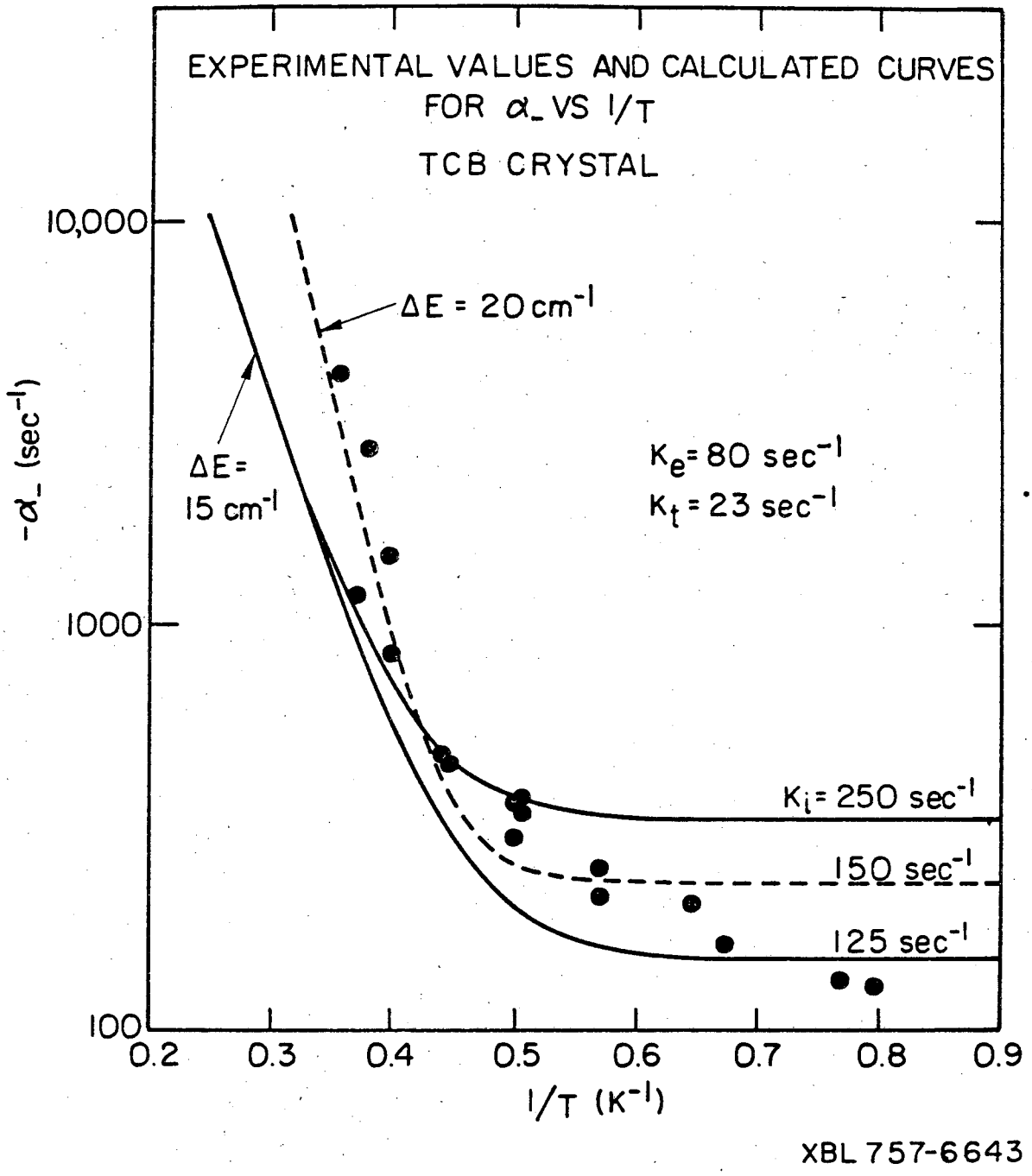
EXPERIMENTAL VALUES AND CALCULATED CURVES
FOR α_ VS 1/T
TCB CRYSTAL
10,000
1000
100
-α_ (sec⁻¹)
ΔE = 20 cm⁻¹
ΔE = 15 cm⁻¹
Ke = 80 sec⁻¹
Kt = 23 sec⁻¹
Ki = 250 sec⁻¹
150 sec⁻¹
125 sec⁻¹
0.2
0.3
0.4
0.5
0.6
0.7
0.8
0.9
1/T (K⁻¹)
XBL 757-6643

Figure 12

decay channel. In order to illustrate this effect, Fig. 12 also shows a calculated curve for α_- using $K_e = K_t = 23\ sec^{-1}$ and $K_i = 125\ sec^{-1}$. If K_e increases with increasing temperature, deviation from the calculated curve in the positive direction is expected until the limit is reached where α_- is dominated by the increasing detrapping rate.

Based on the above considerations, one can set a limit on the trapping rate constant of $K_i = 100\text{-}300\ sec^{-1}$ and on the detrapping energy of $\Delta E = 15\text{-}20\ cm^{-1}$. These limits reflect both the uncertainty in the estimates of K_i and ΔE due to the experimental uncertainty in the measurements themselves as well as the "best fit" to the model calculations. For the purpose of this analysis, it was found that the temperature dependence of K_0 was adequately described by

$$K_0 \propto N \exp(-\Delta E/kT). \qquad (27)$$

The obtained value of ΔE is to be compared with a spectroscopically measured trap depth of $\Delta = 21.3\ cm^{-1}$.

It should be noted that the existence of three triplet spin sublevels with different decay times to the ground state has been largely ignored. For example, in the determination of experimental values of N_e^-/N_0 (Fig. 10) all decay components except those corresponding to trap buildup times were lumped together. This sort of treatment of the data should have little effect on the interpretation, since it depends most strongly on the build-up rates (and thus on the values and temperature dependence of K_i and K_0 rather than K_e and K_t) which are presumably the same no matter which sublevel is involved.

C. Trapping rate and coherent energy migration: Coherence length

The measurement of the trapping rate constant becomes especially significant once the trap concentration is known. The concentration of x-traps in the crystal (i.e., the average number of exciton states per trap) can be approximately determined by assuming that the steady state x-trap population obeys Boltzmann statistics and fitting the experimentally determined phosphorescence temperature dependence to a curve obtained from eqs. (21) and (23). Using an integral approximation to the sum in eq. (23) and applying the formula (for the zero-order modified Bessel function of the first kind):

$$I_0(\zeta) = (1/\pi)\int_0^{\pi} \exp(\zeta \cos\theta)\, d\theta \tag{28}$$

one obtains an expression for the trap probability:

$$P_{trap} = \frac{\exp[-(2\beta-\Delta)/kT]}{\{\exp[-(2\beta-\Delta)/kT]+NI_0(2\beta/kT)\}} \tag{29}$$

where N is the number of exciton states per trap. The experimental data and calculated curves for $\beta = 0.25\ cm^{-1}$, the various values of N, and the tabulated values of $I_0(\zeta)$ are shown in Fig. 13. Thus, the chain length is estimated to be 256000 molecules.[22]

These two pieces of information (the x-trap concentration and trapping rate constant) can result in increased insight into the coherent nature of exciton propagation in these crystals. An x-trap concentration of 1/256000 implies a one-dimensional exciton chain length of 9.6×10^5 Å on the average. The thermally averaged group velocity, which varies less than 6% in the temperature range 1-4° K, can be calculated from the exciton

Figure 13. Temperature dependence of steady state phosphorescence emission of the x-trap origin in the TCB neat crystal used in these investigations. The circles represent measurements of the recorded height of the peak, while the dots represent the corresponding areas of the peaks. The solid curves were calculated from eq. (29), for $4\beta = 1\ cm^{-1}$ and $\Delta = 21.3\ cm^{-1}$.[19] It should be noted that the calculated curves are insensitive to β in the narrow band limit ($4\beta << \Delta$), although they may be somewhat sensitive to the value of Δ used. We estimate the uncertainty in the value of the number of exciton states to be better than a factor of 2.[23]

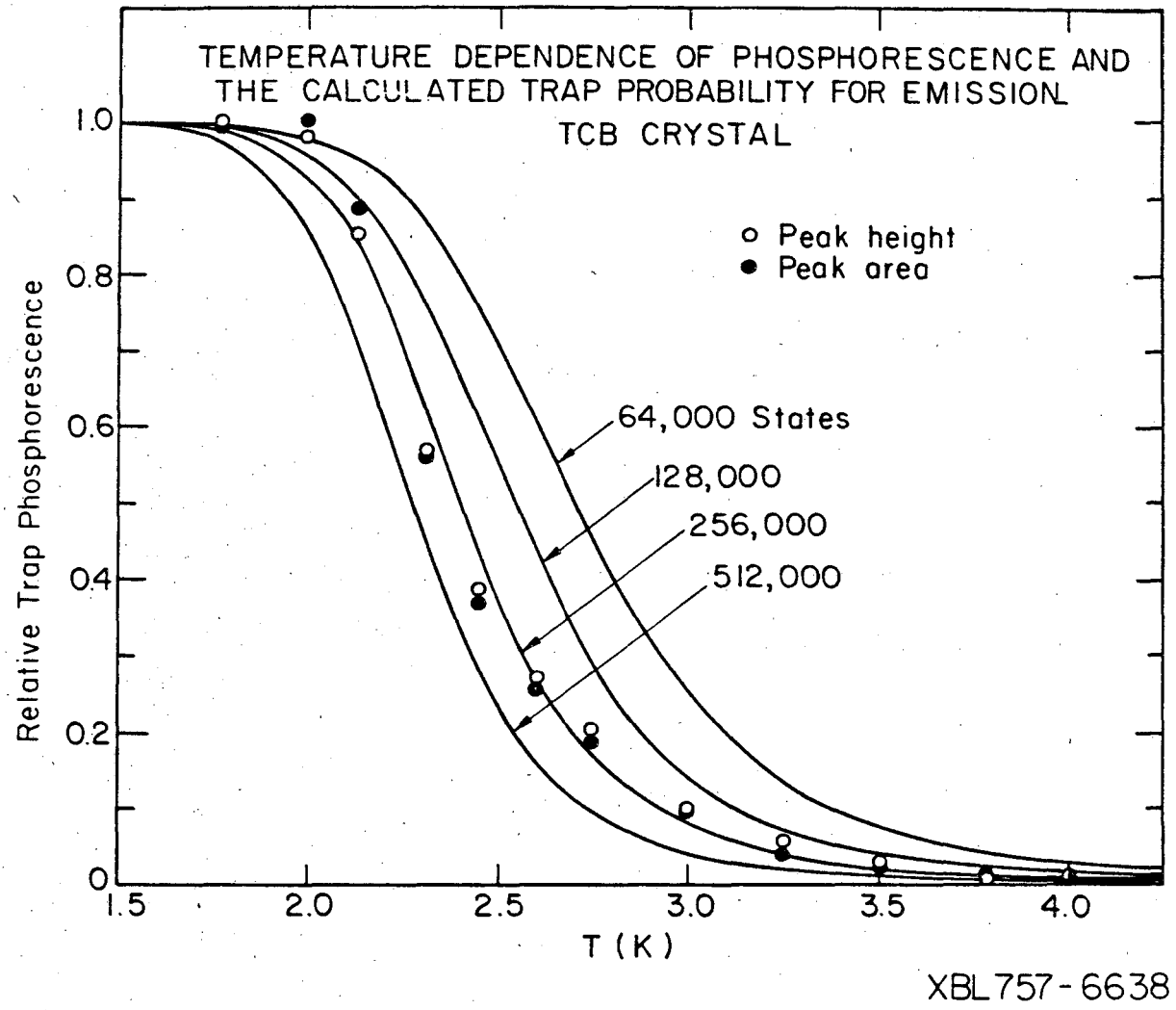
TEMPERATURE DEPENDENCE OF PHOSPHORESCENCE AND
THE CALCULATED TRAP PROBABILITY FOR EMISSION
TCB CRYSTAL
o Peak height
● Peak area
64,000 States
128,000
256,000
512,000
Relative Trap Phosphorescence
1.0
0.8
0.6
0.4
0.2
0
1.5
2.0
2.5
3.0
3.5
4.0
T (K)
XBL757-6638

Figure 13

dispersion: $\langle V_g \rangle = 2700$ cm/sec at 1.3°K. If one takes $K_i = 200\ \text{sec}^{-1}$, the completely coherent limit [eq. (6)] gives $\alpha = 7 \times 10^{-4}$ for the trapping probability per exciton-trap encounter, a value that seems quite low. On the other hand, the random hopping model [eq. (7)] estimates a trapping rate constant on the order of $K_i = 0.46\ \text{sec}^{-1}$, which is too small to be reconciled with the experiments. However, in the intermediate regime represented by eq. (8), one sees that the measurement of K_i allows a minimum coherence length to be assigned to the exciton motion; with $K_i = 200\ \text{sec}^{-1}$, one finds that:

$$\langle \ell \rangle \gtrsim 700\ \text{Å} = 186\ \text{molecules}. \qquad (30)$$

It is clear that the incoherent limit cannot give a value of K_i that is consistent with experiment, even when possible uncertainties in β and d are considered. For a change in d of a factor of 2 (the estimated possible error) K_i increases to $1.84\ \text{sec}^{-1}$ which is still two orders of magnitude less than the measured value.

It follows from eq. (5) and average group velocity that the minimum coherence time is $\tau_c \gtrsim 2.6 \times 10^{-9}$ sec. This coherence time is consistent with the correlation time for scattering obtained from the exciton ODMR spectrum by Francis and Harris[9] and that for dimers of proto-TCB in a deutero-TCB lattice measured by Zewail and Harris.[11] Using $\tau_c = 10^{-7}$ sec. (from Ref. 11), one notices that the minimum coherence length reported here is considerably smaller than the maximum value $\langle V_g \rangle \tau_c = 27000$ Å. There are several possible sources of this discrepancy. For example, the factor α in eq. (8) is not necessarily near 1.0. If one assumes $\langle \ell \rangle = \langle \ell \rangle_{max} = 27000$ Å, then the resulting value of α

indicates that as few as 3% of exciton-trap encounters actually result in trapping of the excitation. One should also keep in mind that the coherence length has been derived in an indirect and average way. The details of exciton propagation and interaction with phonons were not explicitly considered. For example, optical excitation initially excites only levels near $k = 0$. Thermalization and evolution of these states into propagating excitons was assumed to be fast compared to the trapping process. Similarly, the nature of the mixing of k-states due to scattering of phonons might play an important role in determining how far the exciton moves before the next scattering event such that the coherence length is significantly different from $\langle \ell \rangle_{max}$.

The question of to what extent specific mechanisms determine the coherence of the exciton motion is left unanswered. However, it seems certain that exciton-phonon interactions and scattering of the excitons from crystal imperfections other than those responsible for the x-traps themselves play important roles. At the lowest temperature investigated (1.15°K), emission from a trap with an approximate trap depth of 8 cm^{-1} was observed. This is the first time to the author's knowledge that this trap has been seen. It seems likely that other similar departures from perfect lattice periodicity perturb the exciton density of states to an extent sufficient to significantly effect the exciton dynamics but not to manifest themselves in the emission spectrum. However, the concentration of disturbed molecules must be relatively high to effectively shorten the coherence length to the extent observed. Hence, exciton-phonon coupling is expected to contribute significantly to the loss of

coherence. These questions might be partially resolved by measurement of the coherence length as a function of temperature. However, the extraction of this temperature dependence from the data using the model presented here would be difficult. In fact, in this relatively low temperature limit, it has been assumed that K_e, K_t and K_i are temperature independent.

IV. Summary and Conclusions

Short light pulses from a tunable dye laser have been utilized to study the nature of exciton-phonon and exciton-trap interactions in molecular solids (1,2,4,5-tetrachlorobenzene and 1,4-dibromonaphthalene) at different temperatures. The following conclusions can be drawn from these studies:

(1) The time-resolved phosphorescence response reflects the dynamics of exciton-trap equilibria.

(2) In the TCB system where the triplet exciton is essentially one-dimensional and only one trap is interacting with the band, the dynamics can be described by a simple kinetic model. On the other hand, the presence of multiple "localized" states in the one-dimensional DBN system helped in exploring the many routes of communications between the band and traps which are essential in understanding coherence in this system.

(3) The steady state phosphorescence of TCB x-traps indicated the presence of thermal equilibrium with the band states, and thus a chain length of 960000 Å (= 256000 molecules X 3.76 Å) was obtained from the temperature dependence of the emission intensity.

(4) The trapping rate constant obtained from the time resolved phosphorescence at different temperatures together with the chain length measurement enabled us to obtain for the first time a minimum coherence length for triplet excitons of molecular solids at low temperatures: $\langle \ell \rangle$ = 700 Å = 186 TCB molecules.

(5) The measured coherence length indicates that exciton-phonon coupling plays an important role in shortening the coherence length for very long linear chains.

In spite of the fact that many of the details of exciton propagation were ignored, the simple model accounts quite well for the observed data in the case of TCB. Thus, although this work does not necessarily give an accurate determination of the coherence length, it quite probably gives a correct lower limit for $\langle \ell \rangle$.

Finally, it is worth while to point out that tunable dye laser spectroscopy has far greater potential utility in the study of molecular crystals than that which has been used in these investigations. In principle, the laser is able to prepare a well-defined $k=0$ state of the crystal whose dynamics might be very revealing if the proper instrumentation and experimental timescale is available. The coherence of the laser radiation has also only recently been made use of in the study of molecular crystals,[24,25] and the possibility of extending the pulsed magnetic resonance experiments mentioned earlier into the optical frequency range in these systems is quite promising and exciting. The details of the dynamics of individual k-states or wave packets remain very elusive and poorly understood. It is hoped that these kinds of techniques may succeed in more fully describing the detailed role of coherence in the dynamics of exciton propagation.

PART TWO

Picosecond Spectroscopy

I. Introduction

Many aspects of dynamics and relaxation of molecules remain relatively unexplored due to the lack of appropriate experimental probes. Until fairly recently, one such area has been the study of the many interesting molecular processes which occur on a timescale shorter than about 10^{-8} seconds. Examples of such processes include primary events in photochemistry, electron transfer, fast chemical kinetics, molecular predissociation, and radiationless transitions. Condensed phase molecular systems provide many additional examples. These systems are characterized by relatively strong intermolecular interactions with short correlation times, and many dissipation, relaxation, and energy transfer processes occur on the sub-nanosecond timescale. Information about these processes can in principle often be obtained via studies of the appropriate spectral lineshapes. However, practical problems such as spectral congestion or incomplete resolution often make such measurements very difficult. In addition, there are usually several mechanisms which together determine the observed lineshape, and study of individual processes is not possible.

In 1965 the development of the mode locked solid state laser[26] provided the necessary tool for direct time-domain measurements of such molecular dynamics on the picosecond timescale. It was found that a

saturable dye with a short recovery time placed inside the laser cavity resulted in an output in the form of a train of extremely short pulses separated from one another by the time required for light to traverse the laser cavity. This resulted due to the simultaneous oscillation of the laser in many longitudinal modes in such a way that the relative phases of the electric field in these modes was zero. Since the temporal width of these mode-locked pulses depends (through a Fourier transform) on the frequency range of the participating cavity modes, one would expect that the emission linewidth of the laser transitions in ruby and neodymium glass lasers would give pulse widths of about 10^{-12} seconds. In fact, early measurements of pulse widths of mode-locked pulse trains gave values in the range 3-30 psec.[27,28]

As the characteristics of pulses produced in this way became more well-defined experimentally, it became clear that they deviated considerably from ideal mode-locked behavior, particularly in the case of Nd:glass lasers. The shot-to-shot reproducibility of laser output characteristics such as pulse train intensity, length and shape was generally lacking. The appearance of more than one or even many pulses per cavity round trip time was common, and the transverse mode structure was difficult to control. Furthermore, measurements of spectral quality indicated a frequency width several times more broad than needed to account for the pulsewidth of a few picoseconds.[27,28] Since complete temporal coherence would result in a spectral width consistent with the Fourier transform of the observed or postulated pulse shape, this implied the possibility of undetected amplitude or phase substructure. These characteristics often made the experimental application of these pulses

difficult and the results more ambiguous.

A major part of the effort in applying these light sources to the study of molecular dynamics has been expended in understanding and overcoming these difficulties and learning to live with others. For example, since the spectral broadening was found to be greater for pulses in the later part of the train, pulses with nearly transform-limited coherence can be obtained by selection of a single pulse from the early part of the pulse train with an electro-optic shutter.[29] Furthermore, this single pulse technique allows the investigation of samples in which the molecular system would not fully recover during the time between two adjacent pulses in the train. The reproducibility problem can be partially alleviated through careful design and control of experimental conditions. However, the presently understood theory of mode-locking by saturable absorbers[30] indicates that a certain amount of statistical behavior is characteristic of the mode-locking process. Other problems which arise in the application of these light sources more directly effect the design of the experiment itself. One of the most restrictive of these is the lack of tunability of the Nd:glass laser. This can be partially overcome by the use of non-linear effects such as harmonic generation and stimulated Raman scattering to generate picosecond pulses at additional wavelengths, but an interesting experiment is often difficult or impossible because the necessary wavelength is not available. Recent development of mode-locked pulsed and continuous dye lasers has helped in this area. However, these tunable sources also possess certain disadvantages, notably their relatively low peak powers. Secondly, since

photodetectors and electronic signal processing equipment with sufficient bandwidth to observe picosecond risetimes are essentially non-existent, indirect methods of detection must be employed. Typically,[39] a portion of the laser pulse itself is used to probe the dynamical state of the system after some fixed delay. As discussed later, this makes it imperative to develop techniques which can overcome the poor reproducibility of the laser so that data obtained on different laser shots is comparable. Lastly, the propagation of very high intensity light in matter results in many non-linear effects (e.g., self-focusing[62] and self-phase-modulation.[64] These phenomena may interfere with the successful execution of the experiment and must be avoided or compensated for.

In spite of these problems, the field of picosecond spectroscopy is growing rapidly. Areas of recent activity in the field of chemical problems include vibrational relaxation in liquids,[31] radiationless transitions,[32] vision chemistry,[33] photosynthetic energy conversion,[34] reorientation in liquids,[35] electron solvation,[36] and cage effect in solutions.[37] Many clever probe pulse techniques have been devised and non-linear effects utilized to increase the versatility of the technique. For example, one of these allows the simultaneous time and wavelength resolution of a sample's absorption spectrum with a single laser shot.[38] Since there are several good review articles[5,39] which describe these and other experimental applications, they will not be more extensively discussed here.

The coherence of laser light has led to one of the most exciting and interesting aspects of laser spectroscopy, namely the optical analogues to pulsed radio-frequency spectroscopy. These experiments

depend on the ability of laser light to coherently excite molecules to well-defined non-stationary states and have led to the observation of phenomena such as photon echoes,[40] optical nutation[41] and self-induced transparency.[42] Such experiments lead to insight into the mechanisms and interactions responsible for the loss of coherence in molecular systems. In principle at least, application of the full repertoire of pulsed NMR techniques in the optical regime could be invaluable in separating and studying the various contributions to the observed spectral lineshape of the molecules. Recent advances in this area have been made on the 10^{-8} second or longer timescale through the use of pulsed tunable dye lasers[25] and dye laser frequency switching.[24,43] Although the information yielded by such techniques in the picosecond regime would undoubtedly be of considerable value, there have been almost no experiments of this type reported. The one exception is the studies of vibrational dephasing in liquids[44] and optical phonon lifetimes in solids[45] done by the Kaiser group. The main reasons for this absence of picosecond pulsed coherence measurements lie in the properties of the light source, namely the poor tunability, low reproducibility, and questionable coherence properties.

With the aim of investigating some of these problems in molecular physics, the design and construction of a mode-locked laser system was undertaken. In spite of the inherent difficulties in the areas just mentioned, a Nd:glass laser source was chosen. The great body of picosecond work has been done with these lasers, and their high pulse intensities are a great advantage. However, for the study of molecular coherence, coherence properties of the laser light such as its spectral bandwidth and transverse mode structure must also be carefully controlled.

As discussed above, these are not the strong points of glass lasers. During the course of learning to operate this system, it became clear that the success of these experiments depended on the ability to at least partially alleviate these problems. The remainder of Part Two represents an attempt to synthesize as much as possible of the knowledge, understanding, and black magic that has gone into making this system workable. The hope is that at least some trial and error will be eliminated for other users, at least until the system is replaced with one which is more versatile.

In section II the mode-locked laser system is described and a synopsis of valuable alignment and operation procedures is presented. A brief overview of the theory of mode-locked operation is also included. Section III discusses some considerations involved in the design of a picosecond experiment. Various approaches to the probe pulse technique are presented and the closely related topic of design of the method of detection is discussed. Several measurements of the properties of the picosecond pulse such as pulse width and spectrum are presented in an attempt to characterize the pulses produced by this laser system as fully as possible. Finally, some comments on the design of experiments which utilize high intensity light pulses are offered.

II. The Mode-Locked Laser System

A. Principle of operation

In order to appreciate the problems involved in the design and operation of a mode-locked laser oscillator, it is helpful to keep in

mind some of the principles of its operation. The goal is to develop a feeling for the manner in which the physics of these devices and their physical construction interact to determine the actual behavior of the system. Only in this way is the operator able to systematically modify the behavior of the laser system so that it is useful as an experimental tool. In practice however, this goal is relatively remote and has only been partially attained, at least by this experimenter, and a relatively large amount of trial and error is also involved. The following represents a brief discussion of the principles of passive mode-locking only. No attempt is made to deal with the operation of lasers in general, the theory of cavity modes, non-linear optics, etc., since these subjects are well covered in standard texts and reference works.[46]

One can think of a laser cavity as a Fabry-Perot interferometer which has resonances (modes) separated in frequency by $\pi c/L$. These modes represent configurations of the electric field in the laser cavity which have low diffraction loss and propagate unchanged in form. A laser cavity of typical size ($L = 1$ meter) will then have many such modes within the emission linewidth of a typical laser medium. In Nd:glass for example, the emission linewidth is about 200 cm^{-1}, and the number of modes within this bandwidth is on the order of 10^4. Thus, the laser is able to oscillate simultaneously at a number of discrete frequencies. A laser is said to be mode-locked when the radiation in all these modes has relative phases of zero. In other words, the electric field has the following mathematical form:[52]

$$E(z,t) = (1/4)\{-i \exp[-i(\omega_m t - k_m z)] \sum_n E_n \exp[-i(n-m)(t/t_c - \pi z/L)] + i \exp[-i(\omega_m t + k_m z)] \sum_n E_n \exp[-i(n-m)(t/t_c + \pi z/L)] + c.c.\} \quad (31)$$

where the sum is over all modes which receive gain from the laser medium and the center frequency of the field is at mode m. $t_c = 2L/c$ is the cavity round trip time where L is the cavity length. This equation describes a pulse of light bouncing up and down in the laser cavity, leading to the appearance of a train of pulses beyond the partially reflecting output mirror.

The presently accepted theory of mode-locking by a saturable absorber in the laser cavity is due to Letokhov.[30] It describes the mode-locking process in the time domain as the evolution of the radiation in the cavity under the influence of the saturable dye and the gain medium. The process is broken into three stages for the purpose of discussion. The linear amplification stage begins as the pumping radiation increases and the laser first reaches threshold for a substantial number of modes. Oscillation in each mode is initiated randomly so that no initial phase relationship exists among the electric fields of different modes. This results in an electric field which fluctuates randomly in time due to interference and beating of the multi-mode field. The duration of the fluctuations of the field (auto-correlation time) depends on the frequency spread of the excited modes and is on the order of the cavity round trip time divided by the number of participating cavity modes (10^{-13} to 10^{-12} sec for a Nd:glass laser). During the linear stage the

saturable absorber has little effect since the radiation is too weak to effectively bleach it. Thus, as amplification continues, gain narrowing causes preferential increase of radiation in modes near the center of the emission line of the laser medium. This process is accompanied by a broadening of the average width of the fluctuations.

The non-linear stage begins when the most intense fluctuation is able to begin to bleach the saturable absorber. It then feels less loss than the weaker pulses and is preferentially amplified at their expense. This stage begins in a Nd:glass laser when the peak intensity reaches $\sim 10^7$ W/cm^2. Furthermore, the saturable absorber tends to absorb the wings of the pulse and pass the more intense center portion resulting in a pulse-shortening effect. The limitation to this shortening is provided by the finite recovery time of the saturable absorber, leading to inefficient absorption of the trailing wing of the pulse. It was pointed out[30] that the statistical nature of initiation of laser operation and selection of the most intense fluctuation is an inherent limitation of the passive mode-locking process. This may provide a partial explanation of the variability of the output of such lasers as well as observation of several simultaneous pulse trains on some laser shots.

As its intensity increases, the non-linear index of refraction of the optical components, particularly that of the laser rod, can result in self-phase modulation or self-focussing of the picosecond pulse circulating in the cavity. The dispersion of the laser rod can then distort the temporal structure of the pulse due to this frequency modulation. The effect is deterioration of the coherence of the pulses toward the center and end of the pulse train.

To summarize, there are several characteristics of mode-locked pulses which can be understood on the basis of this theory of ultra-short pulse production. The first is the statistical nature of the passive mode-locking phenomenon. However, calculations have indicated that this is probably not the major cause of the observed lack of reproducibility. As Letokhov and others have pointed out, difficult to control experimental conditions such as the transverse mode structure must be considered as well. Secondly, the gain profile in the linear amplification stage causes the pulses to be broader than the theoretically obtainable minimum. It has been demonstrated that this problem can be alleviated by modifying the gain profile with suitably designed intracavity filters.[66] However, if one is willing to accept the longer pulse width, this is not necessary. Thirdly, the finite relaxation time of the saturable dye limits the obtainable pulse width as well and also leads to an asymmetry of the pulse shape. Finally, the pulses later in the train possess undesirable substructure and lack complete coherence.

From a practical viewpoint, one should keep in mind that good mode-locked pulse trains will be produced whenever the most favorable pathway for release of the stored pumping energy is the production of ultra-short pulses. This depends on a complicated interplay between saturable dye concentration, pumping energy and mode selection. The effects of some parameters can be fairly well understood on the basis of the accepted theory. For example, a higher than optimum dye concentration requires a larger pumping rate to reach threshold and results in more stored energy in the laser rod. Once the non-linear amplification stage begins, the correspondingly greater gain modulation results in

dumping of this stored energy in a shorter time (i.e., shorter pulse trains result). Less than optimum time is available for evolution of a single ultrashort pulse, and the influence of the non-linear refractive index is felt sooner and more strongly. On the other hand, the influence of many parameters such as the transverse mode structure is not well understood. Presumably, the spatial uniformity of the TEM_{∞} mode and its lack of "hot spots" should result in significantly less self-focussing and associated nonlinear effects. However, selection of TEM_{∞} seems in practice to increase the instability of our mode-locked oscillator. The source of this problem is not clear. Many other similar effects exist, and the best combination of conditions for optimum mode locking is most easily reached by a semi-educated trial and error process. The result of this process at its present level of sophistication is described in the following two sections which are concerned with the design of the mode-locked laser system and the procedures used in its alignment and operation.

B. Design and construction of the laser system

To obtain optimum coherence properties from a Nd:glass picosecond laser, it should be operated in a single transverse mode (TEM_{∞}), and a pulse should be selected from the beginning of the pulse train before distortion due to non-linear processes becomes important. Clean single pulses should be produced in a substantial fraction of laser shots, and the surrounding background light level should be as low as possible. Sufficient amplification and harmonic generation capability should be included for maximum flexibility. The system described below has evolved

into a configuration which incorporates these features in a reasonably optimum and convenient way, although there are several areas where improvement is needed. A schematic diagram of this system is shown in Fig. 14.

Laser Oscillator

A minimum mode-locked oscillator includes the laser head, two mirrors which form the cavity, and a saturable absorber. Our Nd:glass laser also includes an intracavity aperture for selection of TEM_{∞} mode. The saturable absorber consists of a solution of Eastman #9860 Q-switch dye in 1,2-dichloroethane. The dye solution is contained in a flowing dye cell which consists of one window and the rear laser reflector so that the dye solution is in contact with the rear reflector. The surfaces of all oscillator components (except the reflecting surfaces of the mirrors) are wedged at a small angle or cut at Brewster's angle to avoid longitudinal mode selectivity due to reflections along the laser axis.

The mechanical design of the oscillator has stability in mind. It is built on a Gaertner Corp. lathe bed type optical bench of 1.5 m length which rests in turn on a 1" thick steel plate table. The mirror holders are Lansing differential screw micrometer angular orientation mounts bolted to the Gaertner carriers. The principle disadvantage of these mounts is their construction from both aluminum and steel so that they are somewhat sensitive to ambient temperature changes. They are specified to have a resetability of 0.1 arc-sec. The laser head is mounted on its own optical bench carrier and possess two kinds of adjustments: one for height and "tilt" of the laser rod in the vertical plane,

Figure 14. The laser oscillator is formed by a resonant cavity consisting of reflectors M_1 and M_2, and the Brewster-angled Nd:glass laser rod, L. The aperture, A, selects for TEM_∞ mode, and the laser is mode-locked by a saturable dye, D, whose flow is indicated schematically. The laser system is aligned with a 5.0 mW helium-neon laser. The pulse selection system consists of an ultra-fast shutter formed by two Glan-Thompson polarizers, GP, and a Pockel's cell, PC, which is energized by a spark gap triggered by the rejected pulse train, SG. The single 1.06 μ pulse traverses the amplifier rod, A_1, twice and the second amplifier, A_2, once. It then passes through a saturable dye cell (not shown) which serves to remove any low intensity background radiation which might be present. Generation of a second harmonic pulse at 5300 Å is possible in a KDP (potassium dihydrogen phosphate) crystal.

MODE LOCKED Nd-GLASS LASER SYSTEM

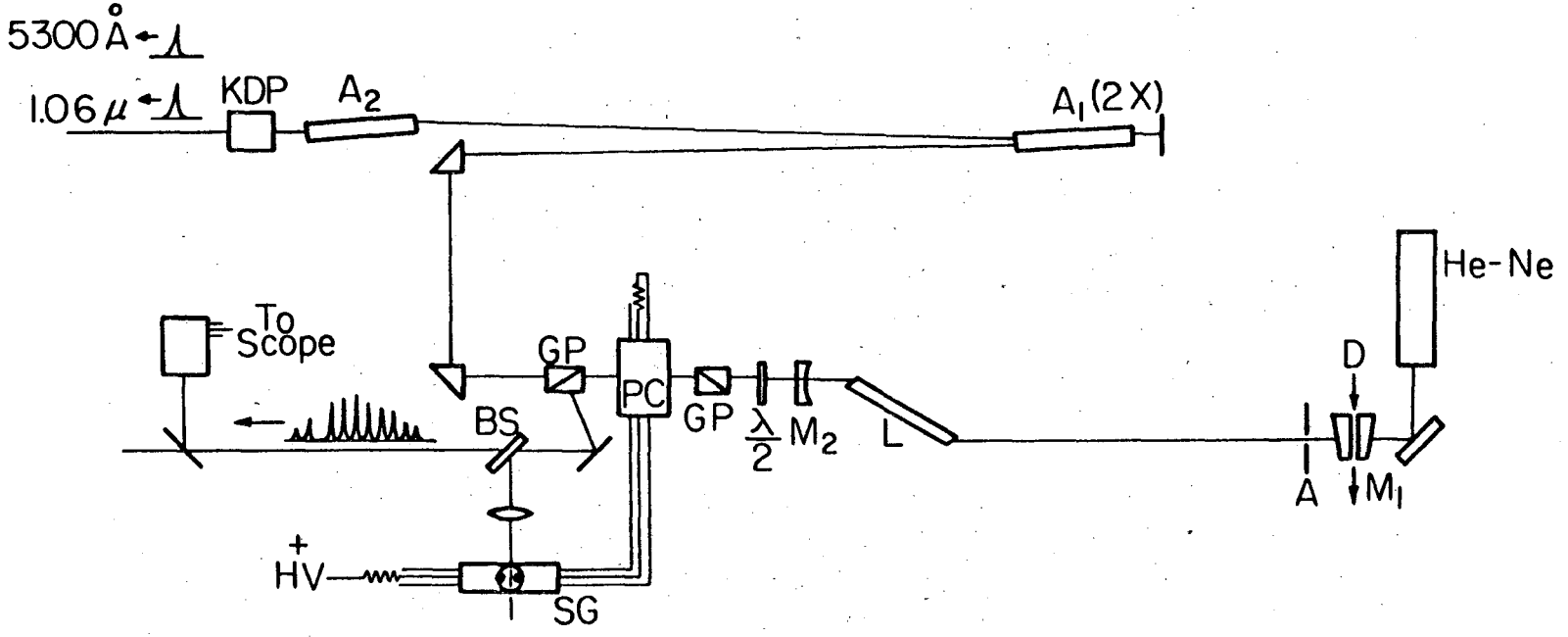

Figure 14

and one for the angle in the horizontal plane with respect to the optical bench. The mode selecting apertures are mounted in the cavity using a modified mechanical microscope stage to provide adjustment in the plane perpendicular to the laser axis. An adjustable aperture and several fixed sizes in the vicinity of about 2-3 mm diameter are available.

The laser cavity is an approximately semi-confocal configuration. The cavity length is approximately 1.5 m. It consists of an output mirror of 3.0 m radius of curvature and 30% reflectance at 1.06 microns and a flat rear reflector with 99.9% reflectivity. The reflectors are of the "hard" dielectric coated type and were purchased from Coherent Radiation. These coatings stand up quite well, and it was not necessary to use the more expensive "super hard high power" type. Other cavity configurations were tried as well, ranging from two flat mirrors, to one with 10 m radius of curvature and the other flat, to 6 m and flat, to the one described above. With each set of mirrors, the position of the laser head and aperture as well as the cavity length were varied to determine optimum mode-locked operation. In general, the longer the cavity and the shorter the radius of curvature of the mirror (within the range described), the easier to select for TEM_{∞} mode. However, such a configuration also tends to decrease the size of the transverse mode and thus increase the power density in the cavity, leading to increased probability of damage to the laser rod and coatings. The configuration described above is about optimum. It was found that the laser rod should be positioned near the curved mirror and the dye concentration kept as low as possible or one risks damaging the laser rod. This damage when observed took the form of tiny, almost invisible bubbles in the laser rod and was very detrimental to

consistent mode locking.

The laser rod consists of a 1/4" diameter core of Owens-Illinois type ED-2 glass surrounded by ED-5 cladding for an overall diameter of 3/8". The clad rod gave lower threshold and generally superior performance compared with an earlier unclad ED-2 rod. The output power is about the same in either case, since the TEM_{∞} mode is small compared to either diameter. The rod is 5-3/4" long with Brewster angle faces and is pumped over 5" of its length by four EG&G FX 47C-5 linear flash lamps. The laser head is of the cloverleaf design and is an adaption of a Lawrence Livermore Lab prototype. It was machined from a brass block, polished, and finished with nickel and gold plating. This head is very easy to machine and gives approximately uniform illumination of the laser rod. A cross-sectional view of this pumping arrangement is shown in Fig. 15. A double elliptical design using two linear flashlamps was also experimented with and resulted in markedly lower threshold pumping rates. However, the focused pumping light seemed to give greater instability in mode-locked operation compared to the uniform illumination provided by the cloverleaf head. The laser head and flashlamps are cooled by circulating de-ionized water through the head itself and through water jackets surrounding each flashlamp. The temperature of the cooling water is maintained by a Lauda K2/R constant temperature bath.

The flashlamps are driven by an approximately critically damped capacitor discharge circuit ($C = 240\ \mu f$, $L = 110\ \mu H$) resulting in a flashlamp pulse of approximately 300 μsec width at half height. The capacitor is charged by a Lawrence Berkeley Lab designed 5 kV power supply which is regulated by an op-amp feedback circuit to give reproducible

Figure 15. The cloverleaf head is easily machined, since each "leaf" of the clover is cylindrical rather than elliptical. The flashlamps, F, are mounted off-center to provide approximately uniform illumination of the rod, R.

CLOVERLEAF LASER HEAD

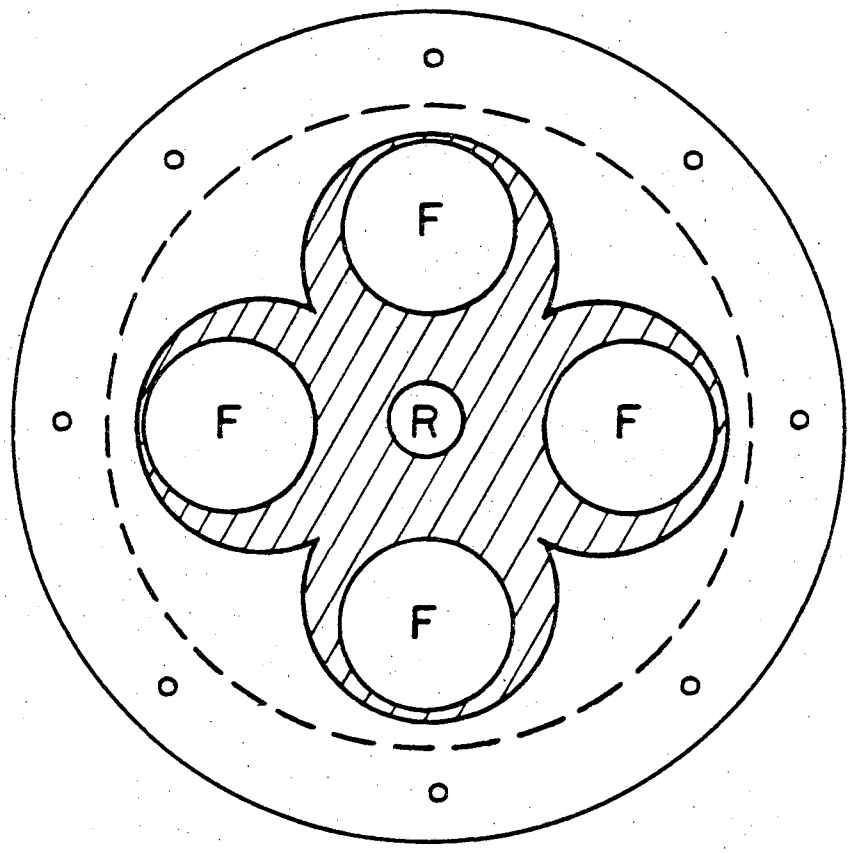

XBL7711-6479

Figure 15

charging voltage to about one part in a thousand. This supply is capable of reaching full charge in about 15 seconds. The lamps are triggered using the series injection triggering method. The trigger pulse is produced by a EG&G TR 136B trigger transformer switched by a cold cathode krytron switch tube.

The mode-locking dye cell consists of a stainless steel housing, a fused silica optical flat which is anti-reflective coated on its outermost surface, the rear laser reflector and a teflon spacer and gasket. An exploded view of this assembly is shown in Fig. 16. The spacer is selected to give a (single pass) path length of 0.1-0.2 mm, and the inlet and outlet ports are arranged to result in even flow of the solution across most of the face of the mirror. The entire assembly fits directly into the 2" Lansing mount. This "contacted" dye cell configuration is said to decrease the occurrence of satellite pulses.[53] Such satellites come about due to the simultaneous presence of two counterpropagating pulses which cross at the location of the dye cell. This allows the dye to be more easily bleached than by a single pulse. Other cell configurations which were tried include non-contacted, non-flowing models and flowing, non-contacted models. Flowing the dye solution seemed absolutely necessary to avoid rapidly deteriorating laser performance. The flow rate of the dye need not be very fast, since the repetition rate of the laser is once per minute, and the pump speed was kept low for minimal transmission of vibrations to the rear mirror mount. The non-contacted configurations often gave clean trains if the cell path length was not smaller than about 5 mm.

Figure 16. This figure shows the dye cell and rear mirror assembly. The cell is formed by the laser reflector, LR, and window, W, contained in a stainless steel housing, HF and HR. The thickness of the cell is determined by the gasket, G, which provides a seal between the two halves of the housing and is partially cut away to allow the dye flow to enter the space between the mirror and window. O-rings provide seals at the front and rear of the housing.

CONTACTED FLOWING DYE CELL

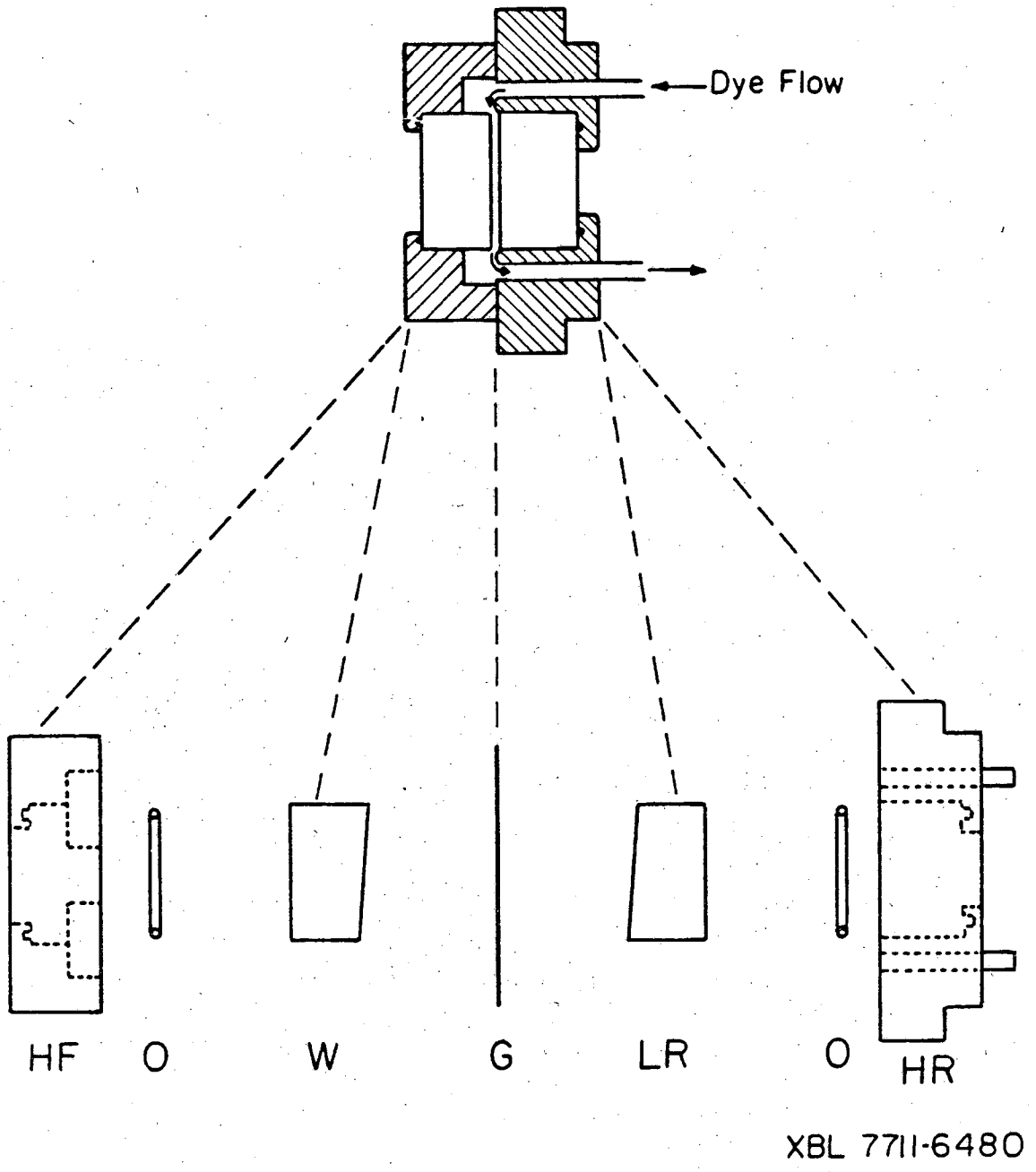

Figure 16

However, the contacted cell seemed to improve the spectral width of the pulses somewhat. The dye solution is contained in a reservoir of about 50 ml capacity and slowly circulated by a Micropump gear-type pump. It is important that only relatively inert materials such as stainless steel, teflon and nylon come in contact with the dye solution. Otherwise both the solution and material may be rapidly degraded with detrimental effects on the laser operation. It is also a good idea to use only the solvent supplied by Eastman Organic Chemicals for the Q-switch dye, since solvent from other sources often contains impurities which cause rapid decomposition of the dye molecules.

For the purpose of alignment, a 5.0 mW Helium-Neon laser beam is directed into the cavity through the rear reflector-dye cell (see below for alignment procedures). This beam is used to align the laser cavity and other optics which the laser pulse will pass through, including the amplifiers and the experimental set-up.

Pulse Selection, Amplification and Harmonic Generation

As discussed above, pulse selection is necessary to obtain a pulse of optimum coherence. In addition, it allows the study of kinetics which require more than one cavity round trip time to return to the initial state. A further shortening of pulsewidth and compensation for less than perfect contrast ratio of the pulse selector can be obtained by passing the pulse through a non-linear absorber. The non-linear absorber consists of a cell containing a relatively concentrated solution of 9860 mode-locking dye. This solution effectively eliminates the low intensity parts of the laser output. Amplification is helpful to increase the

fairly meager energy content of the selected pulse, and three amplifier stages are used in this laser system.

The pulse selector consists of a Lasermetrics ring electrode, dual crystal KD*P Pockel's cell between two Glan-Thompson Q-switch type polarizers. The input polarizer is set to pass the incoming pulse train, and the output polarizer is orthogonal to this so that the shutter is opened to select the single pulse by energizing the Pockel's cell. Although the laser output is polarized due to the Brewster faces of the laser rod, two polarizer are necessary to obtain the maximum contrast ratio (the ratio of shutter open transmittance to shutter closed transmittance). The Pockel's cell is mounted in a gimbal mount to facilitate alignment. The pulse selector is driven by a laser triggered spark gap system similar to that described by von der Linde.[54] The gap itself is of a simple design. It consists of two electrodes of 1/16" radius of curvature mounted on Reynolds Type 167-3517 high voltage connectors. One electrode is threaded to allow adjustment of the width of the gap. The high voltage connectors then screw into an aluminum housing fitted with windows to admit the laser radiation and a port to pressurize the housing with nitrogen gas. A schematic diagram of the spark gap circuit is shown in Fig. 17. Cable A is charged by the power supply to 6.0 kV which is twice the half-wave voltage of the Pockel's cell. Approximately half of the light rejected by the second polarizer is directed by a beamsplitter and 75 mm focal length lens to a focal point in the nitrogen gas between the spark gap electrodes. When the gas breaks down, the charge in cable A empties into cable B producing an approximately square pulse of voltage 3.0 kV and duration equal to twice the electrical length of cable A.

Figure 17. The operation of the pulse selection circuit is shown here in more detail as described in the text. The Pockel's cell is a dual crystal model, operated "electrically in parallel and optically in series" to give a $\lambda/2$ voltage half as large as for similar single crystal models. The resistance R_1 = 100 MΩ determines the recharge time of cable A (~ 6 msec). R_2 = 2 MΩ and R_3 = 100 Ω results in an approximately 10 volt pulse which is used to trigger other equipment.

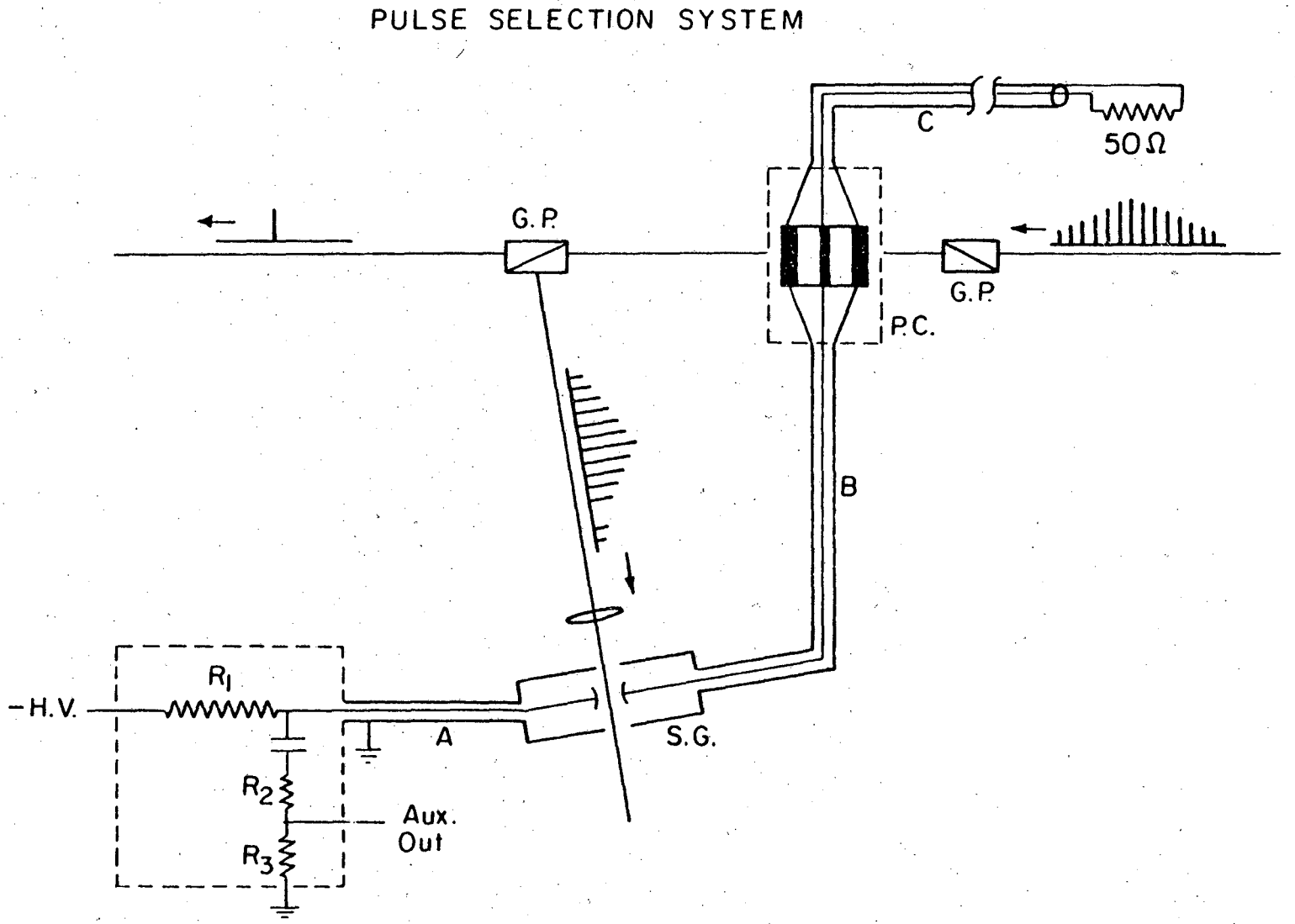
PULSE SELECTION SYSTEM
C
50 Ω
G.P.
G.P.
P.C.
B
R1
-H.V.
A
S.G.
R2
Aux.
Out
R3
XBL 7711-6478

Figure 17

This pulse energizes the Pockel's cell after a delay determined by the length of cable B and is terminated into the long cable C. The Pockel's cell is contained in a copper box for shielding purposes. An AC-coupled voltage divider provides a 10 volt pulse for synchronization of external equipment such as an oscilloscope to the firing of the spark gap.

This arrangement works quite well for selection of a single picosecond pulse from the early part of the train. When Cable A is chosen to give a shutter open time slightly shorter than the time between adjacent pulses in the train, the jitter is such that it fails to select a pulse about 10% of the time. A disadvantage is that adjustment to obtain optimum pulse selection is somewhat inconvenient, since it must be done by varying the incident laser intensity, the nitrogen pressure in the spark gap, etc. However, a pulse selector has been reported[55] which has very good delay and jitter characteristics and is triggered by an electronic signal such as that from a photodiode. It can then be easily set to trigger on a given pulse intensity. Commercial versions are also available, and it seems that these devices may be preferred in the future to the less precise laser triggered spark gap.

The amplifier chain consists of two Mark IX Lawrence Livermore Lab designed amplifier heads and power supply. Each head contains a 1/2"X10" type ED-2 glass rod pumped by a helical flashlamp. Each head is mounted on an arrangement which possesses four degrees of freedom (two rotation and two translation) for adjustment of the rod orientation with respect to the beam. The faces of the rods are cut at an 80 degree angle with respect to the rod axis to avoid feedback of pulse reflections.

Each lamp is driven by a capacitor discharge of approximately 12 kilojoules total energy, and is cooled by forced air. The capacitor bank requires about 1 minute to fully charge. Following the pulse selector, the single pulse is passed through the first rod twice and the second rod once (see Fig. 14). The first two stages give about 10X amplification each while the third gives 5X. The pulse is then passed through a saturable absorber with a small signal transmittance of 10^{-3}. The resulting pulse has an energy of ~ 30 mJ and a beam diameter of ~ 8mm. Non-linear losses[67] in the last amplifier stage are responsible for its lower gain, and further amplification would require beam expansion and larger diameter amplifier rods.

The second harmonic pulse is generated in a Type I angle phase matched KDP crystal purchased from Interactive Radiation. Capability is available to sum the second harmonic and fundamental frequency pulses in a KD*P Type II crystal to produce a pulse at 3530 Å, the third harmonic wavelength. It is also possible to redouble the 5300 Å pulse in an ADP crystal to give a fourth harmonic pulse at 2650 Å. Thus, the fundamental wavelength and its three harmonics provide the basic wavelengths available from this laser system. The path lengths of the harmonic generation crystals are kept fairly short (30 mm or less) to minimize the effects of group velocity mismatch between the input pulse and the generated harmonic pulses.

Experimental Area

The area where the experiment takes place consists of a steel topped table enclosed by black cloth curtains which minimize the stray flashlamp light reaching the detectors. The laser pulse enters through

a small hole in a plywood "wall" at one end of the table. The lenses, beam splitters, etc., which are part of the experiment are held in home-made mountings which are fastened to any convenient place on the table with Enco Model 300 magnetic bases. This makes the placement of optics quite easy and lends versatility to the design of the set-up. In addition to the standard optical components, a Janis variable temperature dewar is also provided for low temperature work. For a discussion of the detection system see section III.A. A detailed description of a typical experimental set-up is given in Part Three in the section on measurements of vibrational dephasing times.

C. Alignment and operation of the laser system

The alignment of the laser system to produce high quality picosecond pulses is more of an art than anything else. Often the laser behaves in a highly irreproducible manner, and the same alignment procedure may work one day and not the next. This problem is mainly the result of the large number of variables and adjustments that can be changed. The frustration is compounded by the low repetition rate and the fact that several laser shots are usually required to evaluate the effect of a particular adjustment. Every worker must expect to have to develop his own "feel" for the process. Perhaps, however, the following description can provide a starting point.

The oscillator is of course the key sub-system. The He-Ne laser beam provides a reference to which the oscillator and other optics can be aligned. Because the laser head is relatively devoid of convenient adjustments, it is important to initially align the He-Ne beam to be as

exactly colinear with the laser rod as is possible. In practice this is done by first tilting the He-Ne beam so it is parallel to the optical bench and then translating it until it enters the center of the laser rod face. Proper alignment is attained when it also exits in the center of the other face. If the laser head must be moved, it is then necessary to readjust the He-Ne beam so it once again enters the center of the rod face. This procedure is iterated until satisfactory alignment of the laser head and He-Ne beam is obtained. This part of the alignment is very inconvenient and could be circumvented by modification of the laser head mounting to include the necessary adjustments of tilt and translation. With the present arrangement, any adjustment of the laser head position necessitates complete realignment of the oscillator.

To align the laser mirrors, one adjusts the front (output) mirror so that the back-reflection from the coated surface is aligned with the incoming He-Ne beam. This is monitored by observing the back-reflection at a pinhole located immediately in front of the He-Ne laser and centered on the beam. The back mirror is then made parallel to the front by superimposing the two back-reflections. This process is easier if one places an optical flat in the He-Ne beam before it enters the laser cavity to split off a portion of both back-reflections. The reflections can then be projected on a convenient wall or other object and quite accurately superimposed. When the alignment is correct, a circular interference pattern is produced where the two back-reflections overlap. This alignment should be sufficient for the laser to operate in "normal mode," i.e., with solvent only in the mode-locking dye cell. One then fires the laser and monitors the output using the burn pattern on a

piece of blackened Polaroid film. By adjusting the mirrors (the front mirror adjustment is most sensitive) and working for lowest threshold voltage and best mode pattern it is possible to obtain operation in TEM_{∞} mode at about 2050 to 2150 volts on the capacitor bank. All of this is done without use of the aperture. It is sometimes possible with experience to get a clue as to what adjustment of the mirrors is needed from the shape of the burn pattern and its position with respect to the He-Ne beam. However, this is not always true, and no general rule exists in this respect. A fringe-like pattern on one side or the other of the burn spot which cannot be removed by minimal mirror adjustment may indicate misalignment of the laser rod. The alignment of the He-Ne with the rod center should be repeated and the mirrors realigned. Once a fairly uniform TEM_{∞} spot is obtained which is close to being concentric with the He-Ne alignment beam, the aperture is inserted. It should be possible to obtain lasing at around 2500 volts. The position of the aperture is adjusted in the x-y plane until lasing is obtained, and then optimized for lowest threshold. This initial alignment does not always produce satisfactory alignment for mode-locked operation, and it is not absolutely necessary. However, it usually provides a useful starting point.

Enough Eastman #9860 Q-switch dye is now added to the solvent in the dye system reservoir to give a solution with optical density 1.00 to 1.05 at 1.06 μ in a 5 mm path length cell. This corresponds to about 80% transmittance (double pass) in the 0.2 mm path length dye cell. It is necessary to let the dye circulate long enough to ensure uniform mixing. This may take as long as an hour. If the alignment is close,

the oscillator will lase in mode-locked operation with a fairly symmetrical TEM_{∞} burn spot about 1.5 mm in diameter. The voltage required on the capacitor is in the range 2800-2900 volts.

Most likely the laser will not oscillate at this point. It is much more sensitive to mis-adjustment of the mirrors, aperture and laser rod with mode-locking dye present. The best approach at this point is to continue to fire the laser at one minute intervals while searching for the optimum alignment by slowly adjusting first the x-y position of the aperture, then back mirror and finally front mirror over a small range until suitable operation is obtained. Appropriate increments for adjustment are fractions of a mm for the aperture, 5-10 micrometer divisions for the back mirror, and 2-5 divisions for the front mirror. One can sometimes guess the correct direction to turn a mirror adjustment by observing the interference between the back-reflections from the two mirrors. Of course, the various adjustments interact with each other. For example, slight displacement of the aperture can usually be compensated by mirror alignment. It should also be noted that the aperture size and dye concentration seem to interact somewhat. If the dye concentration is too high, the operation is very erratic. For example one might observe very strong output followed by several shots with no output at all. If the concentration is too low the output is very weak and not mode-locked, and the threshold voltage not very well-defined.

Once the oscillator is lasing fairly reliably, the energy can be lowered to a point just above threshold. This should be the operating voltage for doing experiments with the laser, since higher pumping rates tend to favor production of multiple pulse trains, pulses with broad

spectral width, and transverse modes other than TEM_{∞}. The quality of the mode-locked output can be checked with a photodiode and traveling wave oscilloscope (see below for details). A better than typical pulse train is shown in Fig. 18(a). Less desirable operation is shown in (b). Frequent observation of messy trains as in (b) usually indicates some sort of alignment problem, although not a severe one or the laser would not operate at all. Often a switch to the next smaller aperture size will help.

Once aligned, the laser is sufficiently stable to remain operating for several days, and with minor readjustments for up to two weeks. The dye concentration should be checked about once a day since it is subject to decomposition due to ultraviolet light from the flashlamps. If a deterioration in performance is noted, the dye system should be flushed and refilled with fresh dye solution. Another result of dye deterioration due to the laser beam itself is the formation of a film on the rear mirror which in turn results in poor laser performance. Sometimes this film is visible when illuminated from behind by a flashlight and is similar in appearance to a damaged mirror coating. The problem can be partly prevented by circulating the dye solution with the pump at full speed for a few seconds every few shots. Eventually the mirror must be translated to a fresh spot or removed from its holder and cleaned.

If all of these adjustments and efforts are to no avail, or if the quality of the pulse trains suddenly worsens, one can also look for more serious troubles such as dirty or damaged optics, a worn out flash lamp, or damage to the laser rod. Laser rod damage usually appears in

Figure 18. Typical output pulse trains from the laser oscillator described here. These traces were obtained by photographing the screen of a Tektronix 519 oscilloscope connected to a Hewlett-Packard PIN photodiode in the configuration shown in Fig. 20. The trains in (a) appear to be cleanly mode locked, while those in (b) show the presence of multiple pulse trains and/or satellite pulses.

EXAMPLES OF MODE-LOCKED PICOSECOND PULSE TRAINS

(A)

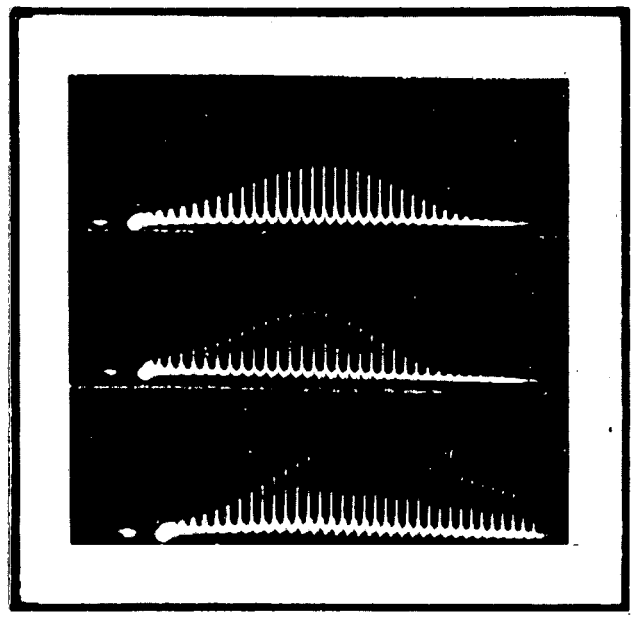

(B)

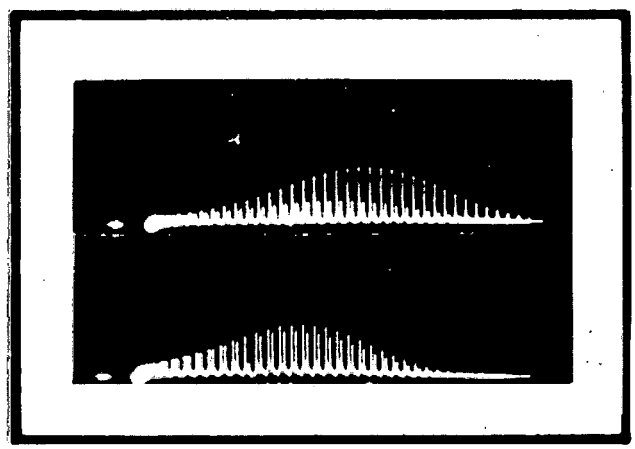

XBB 770-11847

Figure 18

the form of strings of what appear to be tiny bubbles along the beam path within the rod. These are very difficult to see, and are most easily detected by passing the He-Ne beam through the rod. The bubbles appear as bright specks due to scattering of the He-Ne laser light. If, on the other hand, the laser has been operating satisfactorily for a period of time, it is wise to be hesitant to adjust mirrors or aperture. If a problem occurs, one should look elsewhere first and adjust the alignment as a last resort. Even then, it is best to try very small excursions of the various adjustments to begin with. The key to success with this laser is patience and the willingness to accept less than 100% perfect performance. If clean mode-locked pulse trains are produced more than 50% of the time, the oscillator is operating quite well.

Pulse Selection and Amplification

Adjustment of the pulse selector is fairly simple, and it does not usually require periodic readjustment. The only variables are the gap size, the nitrogen pressure, intensity of the incident light and the position of the focal point of the incoming laser beam. The pressure is usually adjusted to slightly above the static breakdown pressure (the pressure at which the gas breaks down with no laser beam present) with a gap width of about 0.5 mm. The position of the switched-out pulse can be adjusted within the train most easily by varying the incident intensity with neutral density filters and to some extend by varying the position of the focal spot. The focus should be approximately centered in the spark gap in all three directions. The laser intensity required to cause breakdown can be lowered somewhat by moving the focus slightly

closer to the negative electrode. However, focusing the radiation directly on the electrode is not advised since significantly higher jitter results. It should be noted that the rejected 1.06 μ pulse train does not exactly follow the He-Ne beam due to the dispersion of the calcite Glan-Thompson polarizer. This complicates somewhat the adjustment of the focus in the gap. The correction necessary to account for this can be determined by monitoring a burn spot immediately before the gap entrance window and comparing with the position of the He-Ne beam. If no missing pulse is observed when monitoring the rejected pulse train with a photodiode, it may help to trigger the scope with the auxiliary output pulse of the spark gap circuit in order to determine at what point in time the spark is actually being triggered. The parameters mentioned above can then be adjusted to time the breakdown appropriately.

The Pockel's cell must be adjusted for minimum transmission when not energized. This is most easily accomplished by initially aligning the back-reflection from the Pockel's cell with the incident He-Ne beam and then minimizing the intensity of the beam transmitted by the second Glan polarizer. The final alignment should be such that the back-reflection does not coincide exactly with the laser axis. If it does, the resulting feedback into the laser cavity will result in poor mode-locked operation or none at all.

In order to align the amplifiers and the optics of the experiment, the polarizer at the input to the pulse selector is rotated by 90° so that the He-Ne beam is transmitted through the output polarizer. It is imperative that the air cooled amplifier rods be fully "warmed up"

by five to ten flashes of the lamps before the final alignment of optics downstream from them. The thermal lens effect due to temperature gradients in the rods is quite noticeable. Although there is very little displacement of the beam due to this effect, the beam size may change considerably. Since the first two amplifier stages are two passes through the same amplifier rod, the beam is adjusted to enter slightly to one side of center and leave slightly to the other side. However, since the displacement between the input and output beams is only ~5 cm over a distance of ~3 m, the angle is very small, and both beams are nearly centered. The third amplifier stage is aligned to accurately center the beam. These adjustments are most easily made by moving the amplifier heads rather than the beam, since their mountings possess all necessary degrees of freedom. A final adjustment that need only be made once is the delay time between the flashlamp discharge of the oscillator and that of the amplifier. This is set to give maximum amplifier gain at the time the pulse passes through. The actual amount of this delay is determined by the laser controller circuit described below. The burn spot of the amplified single pulse is a good check of the final alignment. Distortion of the beam profile due to misalignment of one of the amplifier rods can usually be detected in this manner. The beam profile can be measured more accurately using a photodiode array such as that manufactured by Reticon Corp. The divergence of the laser beam is such that the third stage amplifier rod is approximately filled by the beam, and a beam diameter of ~8mm is measured.

Harmonic Generation

The harmonic generation crystals are aligned by monitoring the input pulse energy and harmonic output energy with suitable detectors and maximizing the ratio by adjusting the crystal orientation. The marks on the input window of the crystal housing must be aligned with the polarization of the input beam. The most sensitive adjustment for Type I phase matching is the angle between the beam axis and crystal axis in the plane perpendicular to the input polarization. This is usually the only adjustment that need be done accurately. An appropriate increment for initial adjustment is about 1 turn on the differential screw micrometer Lansing mount (~ 0.05 degree).

III. Experimental Considerations

A. Probe pulse techniques—Detection and control systems

To explore molecular events on a picosecond timescale with mode-locked lasers, the method of detection must compensate for their inherently low reproducibility and the slow response times of most photodetectors. The second problem has generally been circumvented by using a probe pulse technique.[39] That is, a portion of the picosecond pulse itself is used to probe the dynamical state of the system at a variety of delay times following the excitation pulse. The evolution in time of the ensemble of excited molecules can then be plotted out by monitoring, for example, the absorption or Raman scattering of each delayed probe pulse. The delay time is determined by the difference in the distances traveled by the excitation and probe pulses to reach the sample. This delay is easily varied by mechanical means and provides precision and jitter of a small fraction of a picosecond. With the advent of fast

streak cameras, this method is not necessary for some experiments[35b] such as fluorescence decay measurements. However, these devices are very expensive and are yet in limited use as experimental tools in picosecond spectroscopy.

The problem of reproducibility arises not only from the characteristics of the laser itself, but also from the non-linear interaction of the high intensity pulse with matter. For example if the probe pulse is generated by stimulated Raman scattering, the beam may be distorted by self-focusing in the Raman medium. This distortion may be highly variable from shot to shot, resulting in a fluctuating beam shape. Since the probing process depends on the overlap of this beam with the distribution of excited molecules in the sample, such fluctuations are easily transmitted to the observed signal, and need have no particular correlation with other pulse properties such as intensity. In general, such non-linear processes may tend to magnify the variations (in transverse mode distribution, pulse shape, etc.) present in the input pulses.

These problems have met with various kinds of solutions. The excitation and probing intensities are usually measured for each shot so that the signal can be properly normalized. Several laser shots at each delay can be averaged to reduce the effects of random variations. However, with a repetition rate of one pulse per minute, this becomes quite time consuming. A technique which avoids this problem by recording the entire time evolution of the system in a single laser shot was developed by Rentzepis.[56] In this method, a stepped delay device called an echelon separates the probe pulse spatially into portions which are given different delays. Thus, the sample is probed at several different times in one

shot and the delay time information is converted into spatial position. A graph of the normalized intensity of the echelon pulses vs their spatial position thus displays the transmittance of the sample as a function of time. The intensity and spatial information is recorded with an image detecting device such as a vidicon detector. If the echelon image is projected on the slit of a spectrograph such that the spatial displacement of the probe pulses is along the slit axis, intensity information as a function of both wavelength and delay time is recorded in one shot.[56b] Several other similar techniques have also been developed which provide for ease in normalizing the data and convenient display of spectral information.[57] Whatever technique is used, it should provide capability of normalizing the signal and should minimize the effect of fluctuations which cannot be easily accounted for in the normalization process.

Although the echelon technique has been experimented with in this laboratory, the point by point method was finally settled on for the coherence experiments to be described in Part Three. The reason had to do mostly with the difficulty in controlling the spatial properties of the beam after passage through our home-made echelons. This was an important disadvantage, since a well-collimated and spatially uniform beam is required to satisfy the wave-vector matching conditions in the coherent Raman scattering experiment. In addition, the point by point method allows somewhat greater flexibility in choosing the spacing of the data points in time without changing the optical set-up. Therefore, it was decided that a detection system should be constructed with

the capability of automatically recording the necessary signals, normalizing them, and performing the appropriate averages.

A block diagram of the detection and control systems is shown in Fig. 19. The system is built around an 8080-type microcomputer with 7K of memory. The processor is programmed in machine language and is interfaced to a Netronics scientific calculator for ease in programming floating point arithmetic. The processor can interact with the experiment through two D/A converters and an 8-analog-input data acquisition system (Hybrid Systems Model DAS400). The data acquisition system receives information from the detectors via sample and hold circuits. Once these signals are presented in digitized form to the 8080 microcomputer, they can be manipulated in a variety of ways depending on the capabilities of the software programs. The detectors used vary, depending on the spectral range of interest, from photomultipliers, to Hewlett-Packard PIN photodiodes, to a Au:Ge photoconductive infrared detector. The photomultipliers are preferred due to their large photocathodes. This tends to minimize any error due to fluctuations in the transverse structure of the beam that is incident on the detector. Nine-stage side window types such as RCA 1P28 were typically used when reasonably intense signals were monitored. For more sensitivity when looking for very weak signals, eleven- or thirteen-stage end-on tubes such as EMI 6256S or 9558 were used. The detectors are used with a 1.msec time constant, and the sample and hold circuits are triggered 10 μsec following the laser pulse. Thus, the signal presented to the data acquisition system represents the integrated energy of the pulse. For light signals which are intrinsically of longer duration, such as phosphorescence or fluorescence emission,

Figure 19. The laser controller (upper box) consists of a timer circuit, an interlock and trigger generator circuit, and a delay generator circuit. The interlock circuit accepts trigger commands according to whether or not the timer has signaled it that the proper interval has elapsed, and the delay circuit transmits the trigger to the oscillator and amplifier flashlamp circuits at the appropriate point in time. The gate generator serves to synchronize the operation of the detection system and data processing system (lower box) with the laser. The 8080 microcomputer interacts with the user through a teletype and with the experiment through an analog to digital converter (A/D). The analog signals (heavy black lines) from the detectors, shown here as two photomultipliers (PMT) and a photodiode (PD) are processed by a gated integrator and sample and hold circuits (S&H) before being accepted by the computer.

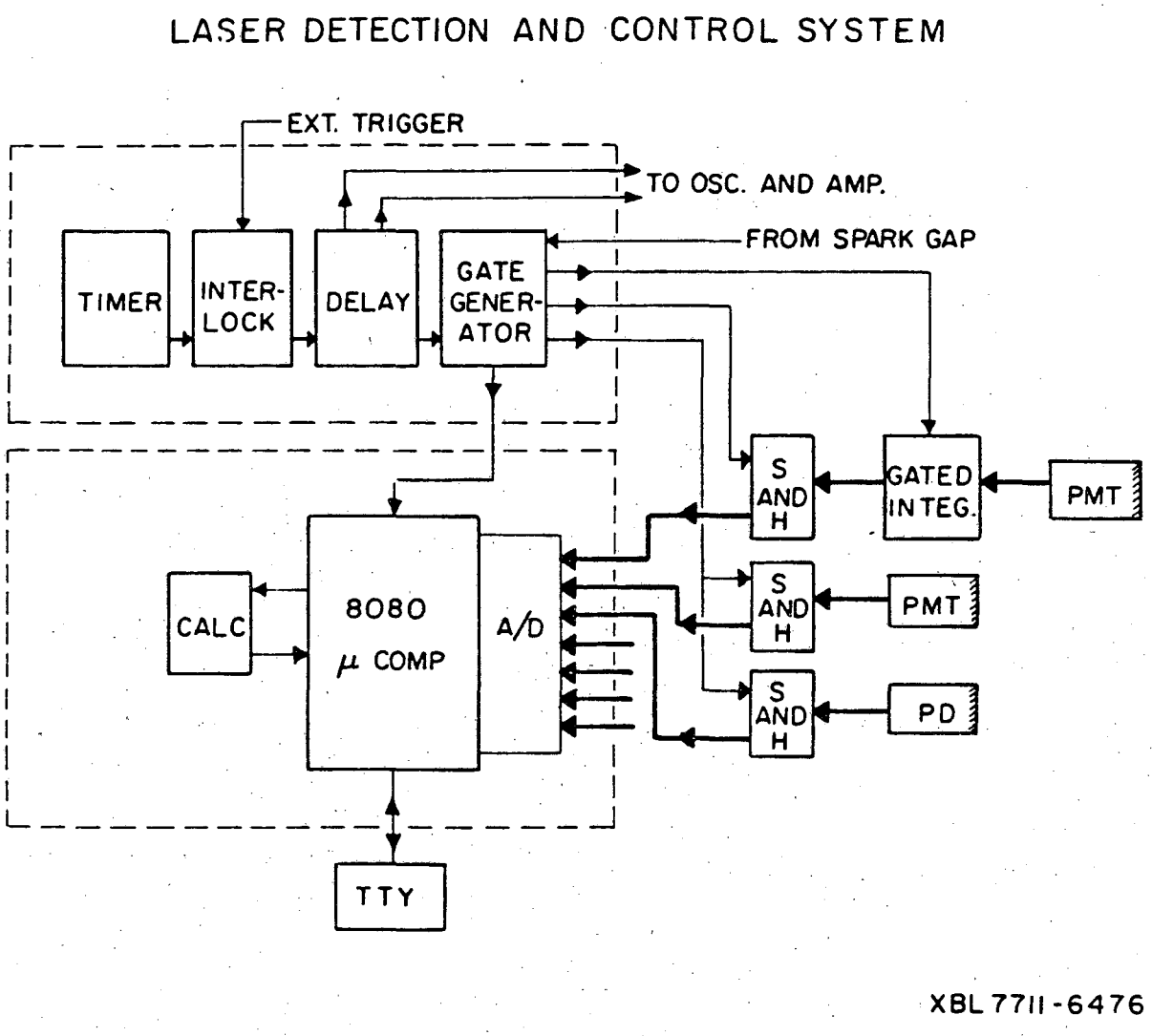
LASER DETECTION AND CONTROL SYSTEM
EXT. TRIGGER
TO OSC. AND AMP.
FROM SPARK GAP
TIMER
INTER-LOCK
DELAY
GATE GENER-ATOR
S AND H
GATED INTEG.
PMT
CALC
8080 μ COMP
A/D
S AND H
PMT
S AND H
PD
TTY
XBL 7711-6476

Figure 19

a gated integrator is also available. This circuit is capable of integrating all or a selected portion of such signals.

The laser and detection systems are controlled and synchronized by a TTL logic circuit. The triggering of the detection system can be synchronized directly to the picosecond laser pulse via the auxiliary output pulse of the spark gap or to any TTL trigger pulse. This trigger signal causes the pulse generator circuit to output appropriately delayed pulses which gate the integrator circuit, trigger the sample and hold circuits, and signal the microcomputer when the data is available to be input and digitized.

The laser controller part of the circuit consists of a timer, an interlock and warning signal generator, a delay circuit for timing the oscillator and amplifier flash lamps, and various delayable auxiliary outputs for synchronizing external equipment. Provision is made for three modes of triggering: 1) Automatically after a set period of time; 2) Manually from a panel-mounted push button; and 3) Remotely from an operator's console or from other external equipment such as an optical multichannel analyzer. In all modes, a timed interlock prevents any trigger signal from being sent to the laser for an operator-set interval following each laser shot. When this interlock is de-activated, an audible alarm sounds for 10 seconds during which period the laser can be triggered. The dye circulation pump is shut off during this time also to prevent any vibrations from reaching the dye cell and mirror mount assembly. These circuits are built in modular form and housed in standard NIM modules for maximum flexibility.

In addition to these detection and control systems, the oscillator output pulse trains must be monitored on each shot to ensure cleanly mode-locked pulses. This requires the use of the fastest detector that is convenient and reasonably economical. For this purpose we have used Hewlett-Packard solid state PIN photodiodes (Type 5082-4203) mounted in a low inductance configuration as shown in Fig. 20. When coupled to a Tektronix 519 traveling wave oscilloscope and biased at 125 volts, this detector exhibits rise and fall times of less than one nanosecond.

B. Characterization of picosecond pulses

It is very beneficial and in many cases imperative to establish the properties of the picosecond pulses one hopes to use in experimental applications. Especially when quantitative results are desired, characteristics such as the pulse shape must be known to properly interpret the data. Because of the lack of suitable instrumentation for picosecond timescales, the determination of characteristics such as pulse width, pulse shape, and intensity are somewhat difficult and must be accomplished by indirect means. Others such as the spatial energy distribution, spectrum, pulse energy, and temporal form of the pulse train can, on the other hand, be fairly simply measured with commonly available methods. When the information from all these measurements is combined, one can obtain a fairly complete picture of the laser pulse including its coherence. This section will describe the results of some of these measurements.

Figure 20. Pulse trains are monitored with Hewlett-Packard PIN photodiodes which are mounted directly to 125 ohm panel connectors to provide fast risetimes when used with a Type 519 oscilloscope. Current to drive the cable and scope is provided by a low inductance capacitor formed by a brass sleeve and a brass cylinder which also serves as mounting for the diode itself. The space between the sleeve-and cylinder is insulated with a thin mylar sheet. This arrangement results in rise and fall times of less than one nanosecond.

FAST RISETIME PHOTODIODE

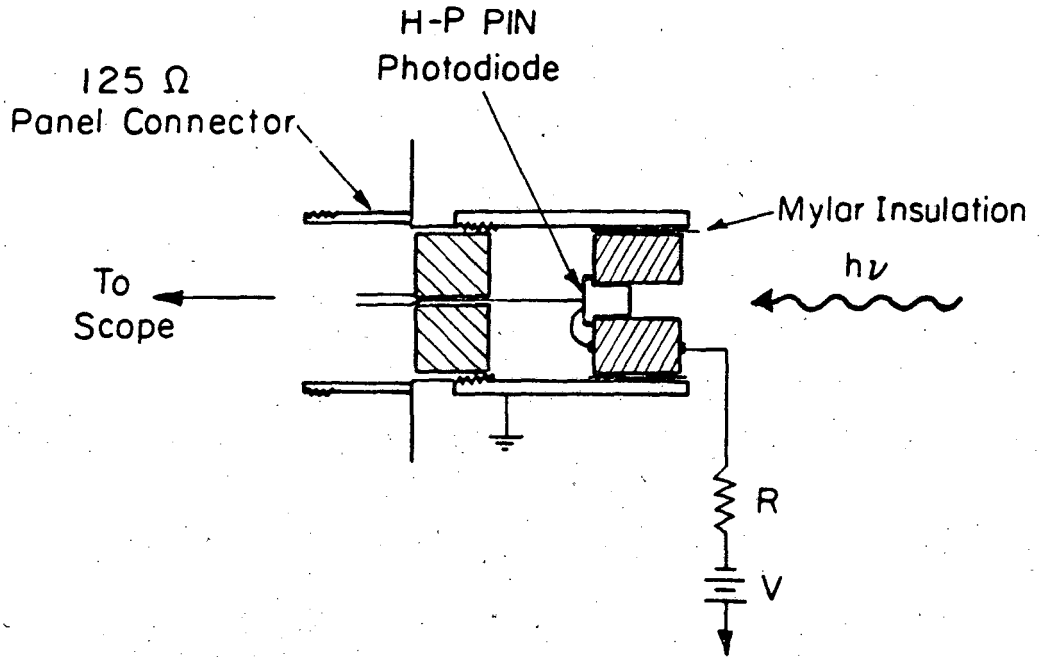

Equivalent Circuit:

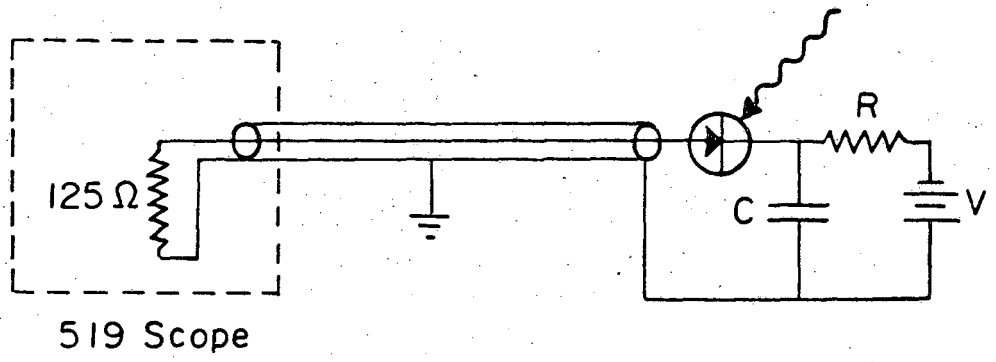

XBL 7711-6477

Figure 20

The most frequently used probes of pulse shape and pulse width involve some form of correlation of the pulse with itself. The most familiar of these is the two-photon fluorescence method[28] which measures the intensity autocorrelation function:

$$G^{(2)}(\tau) = \langle V(t)\, V(t+\tau)\, V^{*}(t)\, V^{*}(t+\tau)\rangle_{t} \qquad (32)$$

where V(t) represents the normalized amplitude of the electric field of the laser pulse. As was pointed out,[29,58] this measurement has several disadvantages. Because it is a second order autocorrelation, it gives incomplete information about the shape of the pulse. In particular, it is unable to display the asymmetry predicted by Letokhov's theory of passive mode locking.[30] The two-photon fluorescence method measures this correlation function by overlapping two oppositely propagating pulses in a solution of a fluorescent dye with an absorption peak at twice the frequency of the laser and which can therefore become excited only by absorbing two photons of laser light. Since the probability of this two-photon process depends on the square of the light intensity, one expects enhanced absorption at the point where the two pulses meet and overlap. This is observed as a bright spot of fluorescence at that point. The width of this spot is related to the pulse width. In addition to its inability to display asymmetries in the pulse shape, this method possesses the further disadvantage that the peak which represents $G^{(2)}(\tau)$ rides on a background from two-photon absorption due to each pulse individually. The ratio of the intensity of the peak to that of the background can be calculated to be 3:1. However, one can also show that random intensity fluctuations with a picosecond correlation

time (i.e., conditions typical of incomplete mode-locking) result in a similar peak, but with a peak to background ratio approaching 1.5:1. Thus, information about the quality and even the true width of the mode-locked pulse may be somewhat difficult to obtain and ambiguous in nature.

In order to avoid these problems, many investigators have turned to more elaborate methods involving higher order correlation functions. For example, Auston[59] measured a fifth order autocorrelation function using a combination of second harmonic generation and four-photon parametric mixing, and von der Linde, et al.,[60] used short vibrational pulses produced by stimulated Raman scattering to probe the shape of their picosecond pulses. These experiments revealed the asymmetry of the pulses and provided a measure of the level of background radiation between the pulses.

Pulses produced by the laser system described in this thesis were examined both with the two-photon fluorescence method and the stimulated Raman method of von der Linde, et al.[60] For the two-photon fluorescence experiment a solution of $\sim 1 \times 10^{-3}$ M Rhodamine 6G in ethanol was used in a cell of 10 cm path length to measure the width of the 1.06 μ single pulses. The standard triangular arrangement[29] was used to provide counterpropagating pulses. The fluorescence streak was either photographed using Polaroid ASA 3000 film, or was imaged on the photocathode of the SIT vidicon of a Princeton Applied Research optical multichannel analyzer (OMA). The OMA is highly superior to the photographic film for recording the fluorescence due to its linear response which simplifies the measurement of peak-to-background ratio. The width of the observed fluorescence spot was calibrated by observing the image of

a ruler placed in the dye cell. The pulse trains were monitored for each shot with a fast photodiode and Type 519 oscilloscope. Photographs of the oscilloscope trace detected most satellite pulses and multiple pulse trains that appeared. Figure 21 shows typical results for a "clean" or apparently well mode-locked pulse train and for a train where satellite pulses were clearly present. Notice the difference in contrast ratio. No perfect contrast ratios of 3:1 were observed, but this could have been due to a slightly fuzzy image on the vidicon since the necessary depth of focus to properly record the entire fluorescence streak is somewhat hard to attain. The average of several clean pulse trains with contrast ratios greater than 2.5:1 gave an average pulse width of 3 ± 1 psec (assuming approximately gaussian pulse shape).

The stimulated Raman measurements of pulse shape were carried out on second harmonic pulses generated in a 30 mm path length crystal of potassium dihydrogen phosphate (KDP) using Type I phase matching. Using the method of refs. 44 and 60 as described below (see pp. 151-157 and Fig. 29) the phase-matched coherent anti-Stokes scattering of these pulses was investigated using ethanol as the Raman-active medium. Briefly, the second harmonic pulse is split into an intense excitation pulse and a weak probe pulse. The excitation pulse excites a C-H stretching mode of ethanol at 2915 cm^{-1} by stimulated Raman scattering. This process results in a short-lived pulse of coherent molecular vibrations which can produce coherent anti-Stokes scattering of the probe pulse. The short dephasing time of this vibration of ethanol ($T_2 = 0.5$ psec) causes the vibrational excitation to rise and fall on a timescale much shorter than the laser pulse.[60] The observed anti-Stokes signal is

Figure 21. Typical two photon fluorescence traces produced by the 1.06 μ laser pulse in a solution of Rhodamine 6G in ethanol and recorded using a PAR optical multichannel analyzer. The top trace corresponds to a pulse train which appeared to be cleanly mode-locked (no satellite pulses or background were observed by monitoring the laser output with a fast photodiode and oscilloscope), and it exhibits a peak-to-background contrast ratio of 2.75:1. The lower trace on the other hand, is for a pulse train which clearly showed the presence of satellite pulses. Its contrast ratio is 1.75:1. Approximately 30-40% of the pulse trains observed failed to obey this correlation between high contrast ratio and apparently clean mode-locking. The distance scale in this figure was calibrated by imaging a ruler on the OMA vidicon with the same optical system.

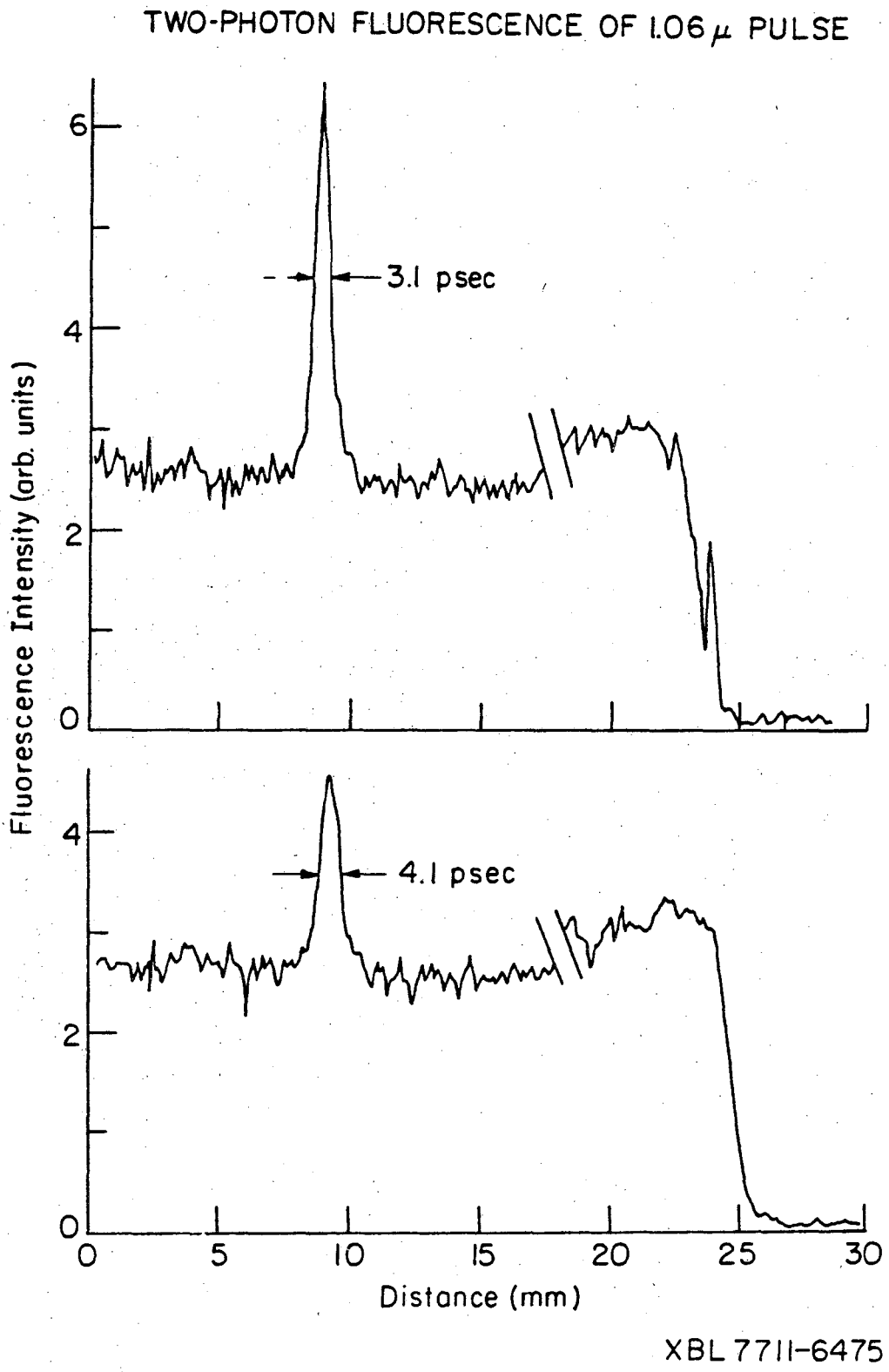
TWO-PHOTON FLUORESCENCE OF 1.06 μ PULSE
3.1 psec
4.1 psec
Fluorescence Intensity (arb. units)
Distance (mm)
0
2
4
6
0
5
10
15
20
25
30
XBL 7711-6475

Figure 21

proportional to a convolution of the probe intensity with the effectively delta-function of vibrational excitation. Thus, a plot of the signal as a function of the probe delay time gives a curve which is very close to the actual pulse shape. The results are normalized to the Stokes and probe intensities and are plotted in Fig. 22. Each point is the average of at least five laser shots. The data indicates a certain amount of asymmetry as shown by the rapidly rising leading edge and more slowly decaying tail. The solid curve is based on a calculation of the stimulated Raman excitation process. The data is well accounted for by a pulse shape of the functional form:

$$I(t) = I_0 \begin{cases} \exp\left[-(t/6.3\ \text{psec})^2\right], & t \leq 0 \\ \operatorname{sech}\left[t/3.9\ \text{psec}\right], & t \geq 0. \end{cases} \tag{33}$$

It was found that this pulse shape was fairly reproducible from run to run if other parameters such as saturable absorber concentration, amplifier gain, and pulse selection were carefully controlled. The uncertainty in the numerical parameters in eq. (33) is about 20%. A further implication of the data involves the level of background radiation before and after the pulse itself. From Fig. 22 one sees that this background must be less than 10^{-3} of the peak intensity. The reason the measurement stopped at this point on the curve was not due to any background, but had to do with the dynamic range of the detector used in the measurement.

The experimentally determined spectral content of these second harmonic laser pulses can now be compared with that expected based on the known pulse shape. For transform-limited fully coherent pulses, we expect a product $\Delta\nu\,\Delta t$ on the order of 1.0 (0.44 for gaussian pulses).[29]

Figure 22. The results of the coherent anti-Stokes experiment in ethanol which were used to determine the pulse shape of the second harmonic picosecond pulses. The time axis represents probe pulse delay time so that the leading edge of the pulse is on the right hand side, and the trailing edge on the left. This pulse shape clearly exhibits some asymmetry, with an approximately gaussian leading edge and exponential tail. Calculations indicate that the observed signal in this experiment should deviate from the pulse shape itself by only a small percentage.

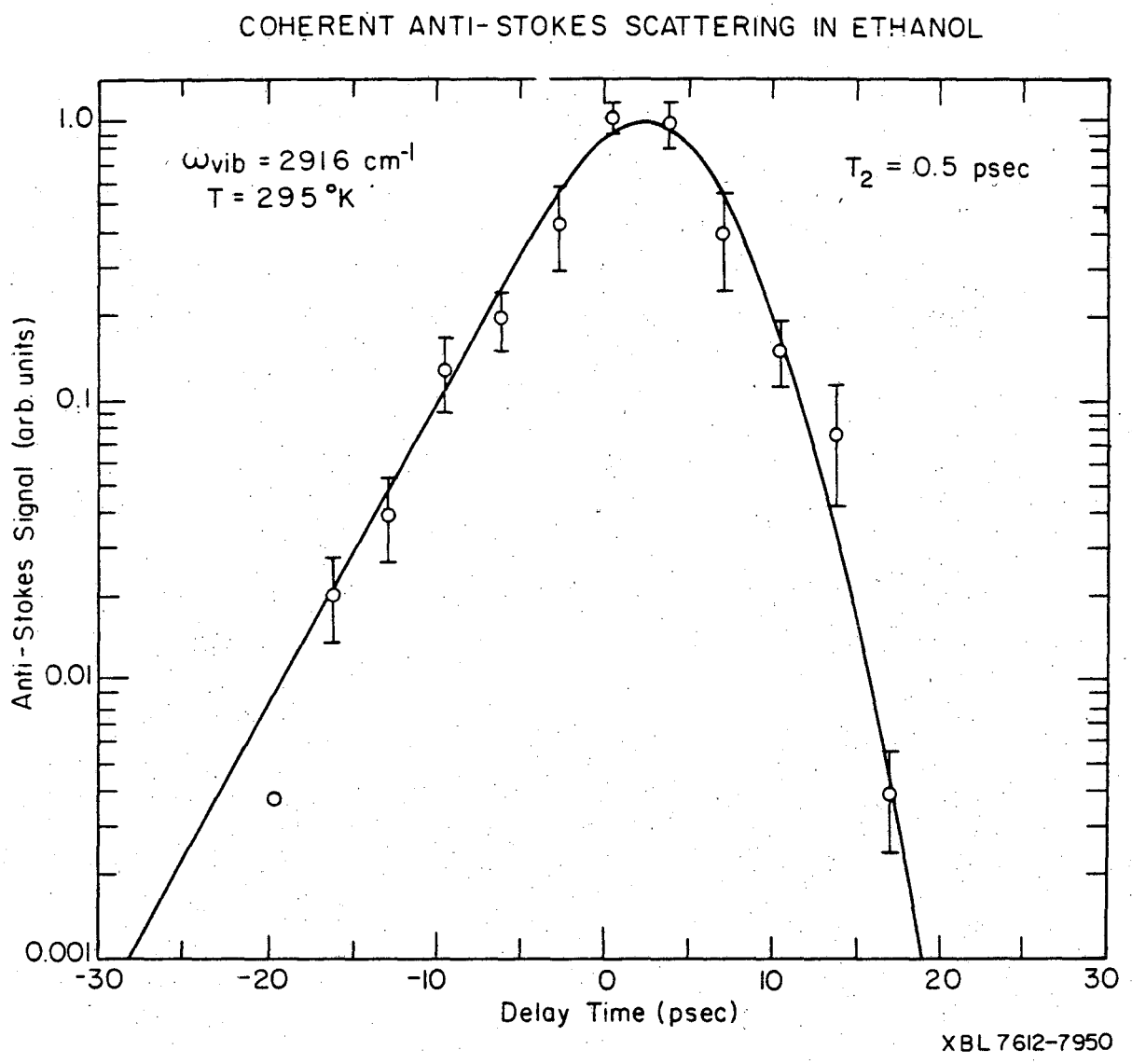
COHERENT ANTI-STOKES SCATTERING IN ETHANOL
ωvib = 2916 cm-1
T = 295 °K
T2 = 0.5 psec
Anti-Stokes Signal (arb. units)
1.0
0.1
0.01
0.001
-30
-20
-10
0
10
20
30
Delay Time (psec)
XBL 7612-7950

Figure 22

If the pulses are not found to be transform-limited, the lack of complete coherence may be accounted for by the presence of sub-picosecond structure. This structure can appear in the form of residual phase modulation or sub-picosecond fluctuations in the amplitude of the electric field. These modulated pulses are less desirable as spectroscopic tools, particularly for experiments where the coherence of the excited molecules is the property of interest. In such an experiment the coherence of the laser pulses must be well known if one is to be sure of measuring the dynamics of the molecules and not the laser light. The spectrum of the pulses was therefore measured using a Spex 3/4m monochrometer and PAR optical multichannel analyzer with an SIT type vidicon. Some typical spectra are shown in Fig. 23 for two ranges of pulse energy incident on the second harmonic crystal. At the higher pulse energies, the effects of non-linear broadening are evident. It seems that the medium responsible for this broadening is either the amplifier rod, or the KDP doubling crystal itself. At lower energies, the spectrum is much sharper. An average of several laser shots gives $\Delta\nu = 6.3\ cm^{-1}$ and (using the pulse width appropriate for eq. (33), the previously determined pulse shape) $\Delta\nu\,\Delta t = 1.9$. Thus under these conditions it is possible to produce picosecond pulses with quite good coherence.

In addition to these measurements which have been discussed here in detail, there are several other techniques which are useful in various experimental situations. For all experiments described here, the quality of the mode-locking was monitored for each shot using a fast photodiode and oscilloscope, and data obtained from pulse trains containing multiple pulses and satellite pulses was rejected. The spatial uniformity of the

Figure 23. Spectra of the 5300 Å second harmonic pulse. The spectra in (a) were recorded with a relatively high power density of about 5.9 GW/cm^2 incident on the KDP doubling crystal, while those in (b) were recorded with a lower intensity of about 10 MW/cm^2. The spectra in (a) show the effects of spectral broadening in either the doubling crystal or the amplifier rod or both, while the widths observed in (b) correspond to those expected for nearly Fourier transform limited fully coherent pulses.

TYPICAL SPECTRA OF SECOND HARMONIC PICOSECOND PULSES

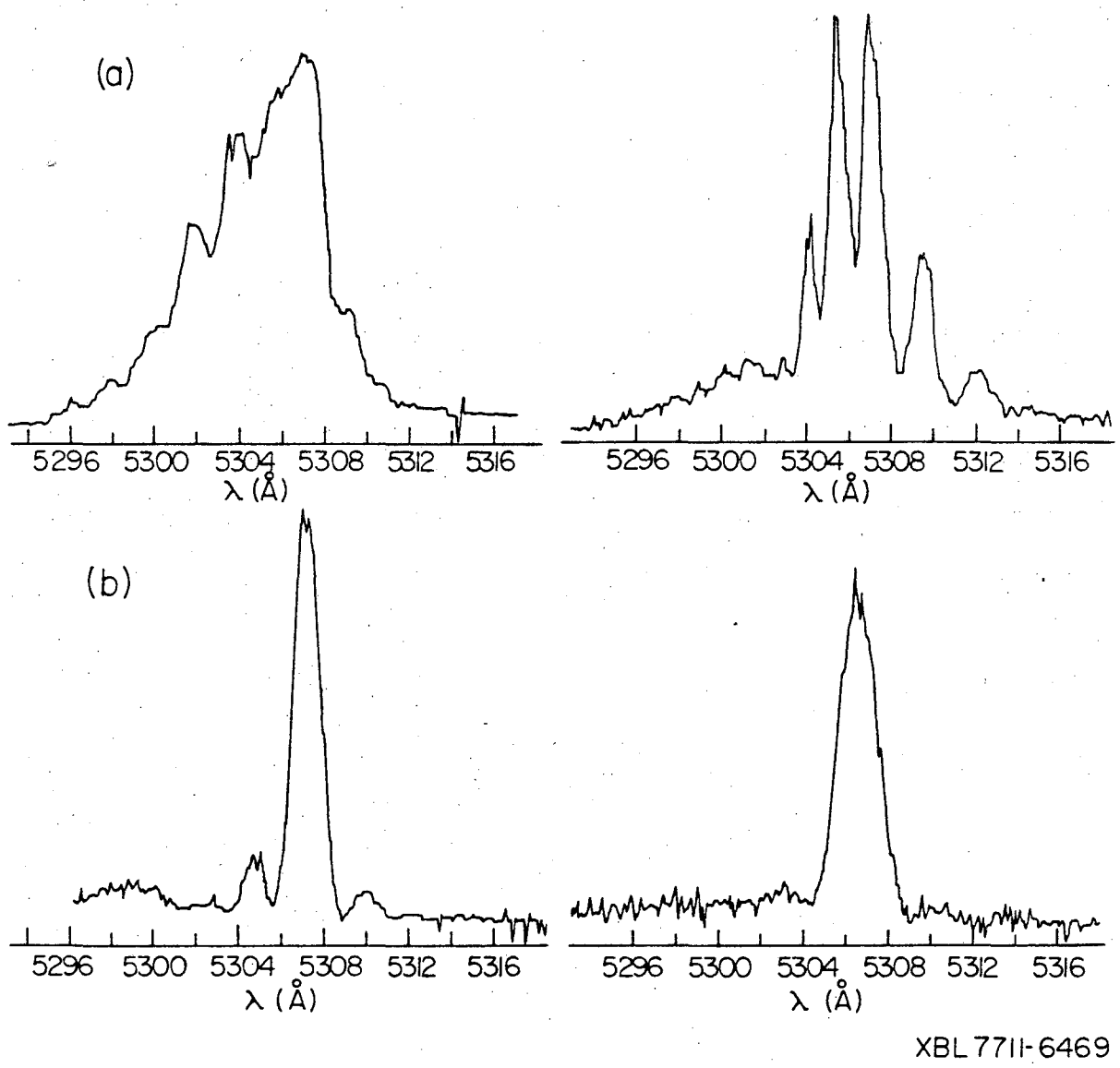

Figure 23

beam was checked with a self-scanning photodiode array (Model RS-4C/512) made by Reticon Corp. This detector consists of a row of 500 photodiodes separated by 0.001", and is also very useful in accurately measuring the diameter of the beam. The output of this device gives a convenient display on an oscilloscope of the beam's intensity cross section. Once its spatial and temporal characteristics are known, one can in principle calculate the peak intensity from a measurement of the energy of the pulse. However, Penzkofer et al.,[61] have shown that the intensity can be directly measured by measuring the energy transmission of a saturable dye solution. They have calibrated this technique and have found that the measurement depends only weakly on other pulse characteristics such as temporal and spatial pulse shape. This method has been found to be quite useful in situations where the intensity must be measured on each shot.

The major difficulty in all of the measurements discussed here is that the pulses are sufficiently irreproducible that the pulse characteristics should ideally be monitored on each shot. In many cases this is impossible and in the case of the pulse shape measurement (which requires many laser shots) even meaningless. Thus, although it is very advantageous to work with well-characterized pulses, it is difficult in practice to do more than partially reach this goal. When results of a picosecond experiment are analyzed and interpreted, the sensitivity of the interpretation to the nature of the pulse must be carefully considered. Estimate of possible errors in experimental measurements must be based on the pulse behavior. This often makes these estimates very difficult. Nevertheless, picosecond pulses have been very useful probes of fast molecular dynamics, and they promise to be so in the future.

C. Experimental use of high intensity laser pulses

The application of high-power pulsed lasers to the study of molecular physics can involve quite different considerations than does the use of other light sources. This is particularly true when non-linear interactions of the radiation with the molecular system are important. In the range of intensities common in picosecond experiments these non-linear processes may be dominant, making the study of other interactions and phenomena more difficult. It is often necessary to work in a relatively narrowly defined range of intensity in order to maximize the effect one wishes to study while minimizing other processes which might interfere. On the other hand, the availability of high light intensity makes possible the study of the non-linear processes themselves as well as the associated molecular dynamics. An example is the use of stimulated Raman scattering to study vibrational relaxation as discussed in Part Three of this thesis. Moreover, these non-linear effects have often been utilized to generate picosecond pulses at wavelengths other than that of the primary laser pulse. The availability of a range of wavelengths greatly increases the variety of possible experiments and adds to the utility of these laser systems in studying the dynamics of molecular systems.

Two of the most pervasive and (usually) undesirable non-linear effects are self-focusing[62] and spectral broadening.[63-65] These effects result in destruction of useful pulse properties such as its smoothly varying transverse intensity distribution and transform-limited temporal coherence. These processes have been observed to occur in a wide variety of condensed phase media and have proven relatively difficult to deal

with both experimentally and theoretically. Self-focusing arises from a non-linear index of refraction of the form

$$n = n_0 + \Delta n \tag{34}$$

where Δn depends on the light intensity (e.g. $\Delta n = n_2|E|^2$ where E is the electric field amplitude). For a laser beam of finite transverse extent, eq. (34) results in a higher index of refraction in the more intense center of the beam and thus causes the focusing effect. The extremely intense field at the focus can cause damage to expensive optical components and leads to the initiation of other non-linear effects such as phase modulation and frequency broadening. That the interaction of a high intensity light pulse with matter can lead to quite extreme spectral frequency broadening has been known for some time. Several explanations of its source have been advanced, including phase modulation by an intensity-dependent refractive index (self-phase modulation)[64] and four-wave parametric mixing.[65] Both approaches have achieved some success in accounting for the observed broadening in certain cases. These "white continuum" pulses have been exploited by Rentzepis,[38] Windsor,[57] and others to record the absorption spectrum of a sample on a picosecond time scale.

However, if broadening takes place in the sample itself, the continuum pulse may render a smaller signal (such as Raman scattering from the probe pulse) difficult to observe. The severity of this problem can be seen when one realizes that the phenomenon is ubiquitous; we have found it to occur to some extent in any material in which it was looked for. For example, Fig. 24 shows portions of the spectrum near

Figure 24. This figure presents some examples of "white continuum" pulses generated by 1.06 μ single pulses in a 5 cm path length cell of ethanol. The upper trace corresponds to an incident intensity of 48 GW/cm^2 and the lower one to 330 GW/cm^2. The laser beam diameter was 0.35 mm. The spectral features seen in these examples are typical but by no means reproducible. For example a strong peak at 490 nm was observed in several shots with similar laser pulse intensities. However, the general features of the lower spectrum were reproduced by several shots, although not on every shot. Clearly, this sort of behavior might easily interfere with rhe observation of an emission signal near, say, 4600 Å, the anti-Stokes wavelength for scattering of 5300 Å pulses by ethanol. The threshold for observation of these broadening effects in ethanol was approximately 10 GW/cm^2.

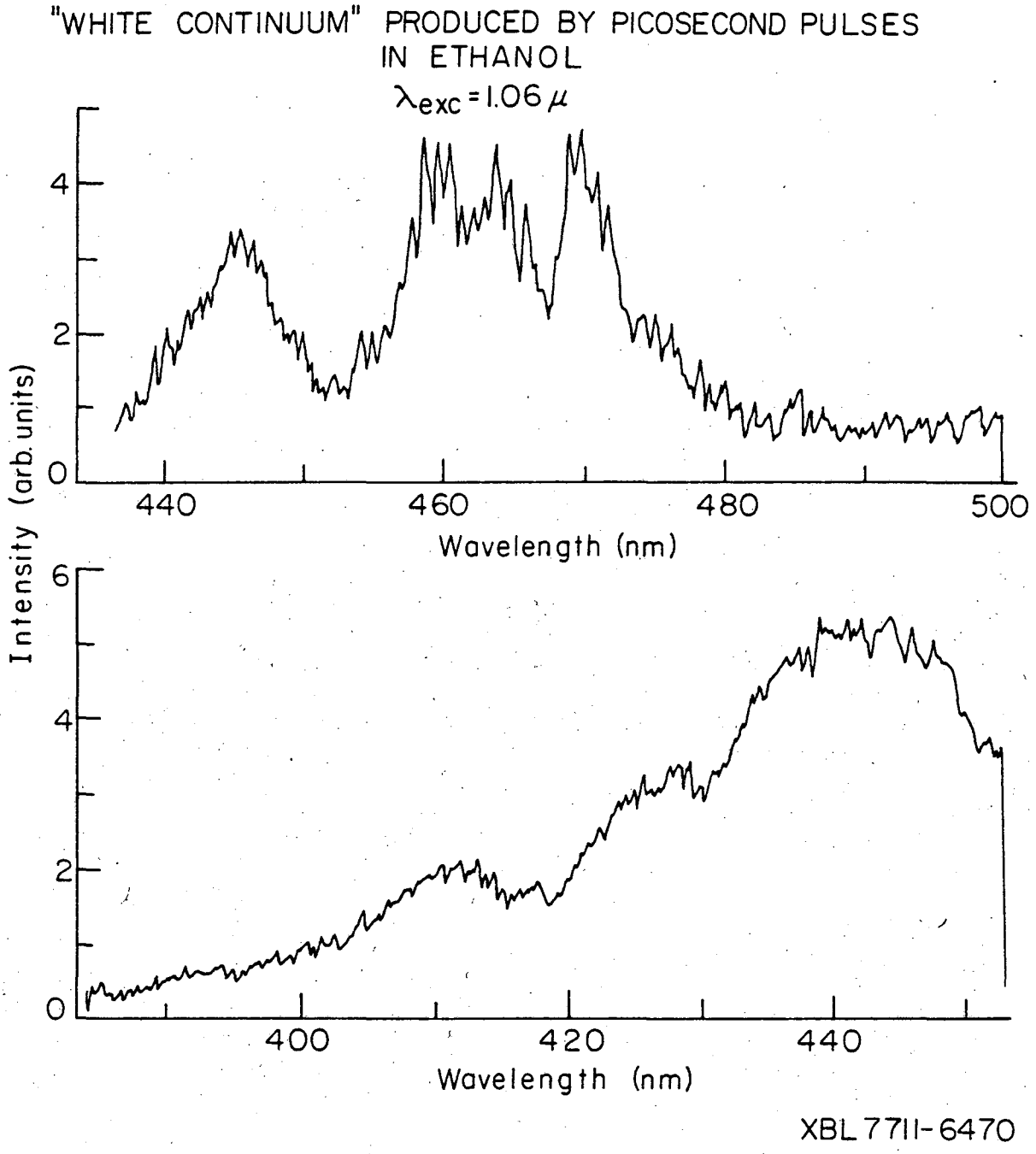
"WHITE CONTINUUM" PRODUCED BY PICOSECOND PULSES IN ETHANOL
$\lambda_{exc} = 1.06\,\mu$
Intensity (arb. units)
0
2
4
440
460
480
500
Wavelength (nm)
0
2
4
6
400
420
440
Wavelength (nm)
XBL 7711-6470

Figure 24

5000 Å of a broadened pulse produced by passing a single 1.06 μ pulse through 5 cm of ethanol. The beam diameter was 0.35 mm (measured using a Reticon photodiode array), and the intensities were calibrated using the saturable absorber method. The spectra were recorded using a Jarrell-Ash 1/4 m polychrometer coupled to a PAR SIT vidicon and optical multichannel analyzer. Some amount of emission was present at essentially all wavelengths extending toward the red from about 4000 Å to the limit of the detector (~ 8000 Å). The intensities of these pulses are within a factor of 100 of the observed threshold for the broadening process (about $1.-5.\times10^{10}$ W/cm^2). At this power level the spectral features observed are not very reproducible, even for pulses of similar intensity.

The major point to be made about these observations (from the point of view of application of picosecond pulses in molecular physics) is that these intensity levels are similar to those necessary to excite ethanol vibrations by stimulated Raman scattering of the 1.06 μ pulse. Thus, the continuum generation could easily interfere with the observation of a weak anti-Stokes signal due to Raman scattering of a 5300 Å probe pulse. We have found that this kind of problem occurs quite often. Thus, it is important that these difficulties be kept in mind during the design and execution of picosecond experiments. Doing so will hopefully reduce the time used to locate weak signals and will increase the ease with which picosecond pulses are used as experimental tools.

PART THREE

Vibrational Relaxation and Dephasing in Condensed Matter

I. Introduction to Vibrational Relaxation

The understanding and characterization of relaxation pathways is an important prerequisite to the understanding of energy transfer dynamics in a given system, since relevant experiments are generally influenced by both kinds of phenomena. Davydov splittings on the order of a few cm^{-1} to a few tens of cm^{-1} have been observed in the vibrational spectra of solids.[68,69] Thus, one expects intermolecular interactions and energy transfer may be of some consequence in the dynamics of vibrational excitations in these systems. This would be particularly true for infrared-allowed modes where strong intermolecular dipole-dipole coupling is possible. However, a major difference between vibrational and electronic excitations, for example, is the timescale imposed by the relevant relaxation times. Clearly then, an investigation of vibrational relaxation mechanisms is important from the point of view of energy transfer as well as providing better understanding of the relaxation processes themselves.

The earliest experimental investigations of vibrational relaxation in condensed phase systems were based on the indirect method of spectral lineshape analysis.[70-73] Work by Gordon[70] and later by Nafie and Peticolas[71] showed that orientational and vibrational correlation functions can be obtained in favorable cases from a Fourier analysis of

the polarized and depolarized components of the Raman spectrum. The resulting vibrational correlation time represents the time for loss of well-defined phase relationships among an ensemble of identically prepared excited molecules. This dephasing results from a variety of mechanisms, including inhomogeneous line broadening, vibrational energy relaxation or redistribution among other degrees of freedom, as well as so-called "pure dephasing" which can result from interactions with other degrees of freedom (either inter- or intramolecular) which modulate the vibrational phase without causing energy redistribution. Thus, the interpretations of spectral lineshape data often relied on difficult to verify assumptions about the dominant source of the broadening.

Direct time-domain studies of these processes was impossible due to the short timescales involved until the techniques of picosecond laser spectroscopy were applied to the problem. Spectral studies indicated relaxation and dephasing times on the order of 0.1 to 100 psec, and the Nd:glass mode-locked laser with its pulse length of 5-10 psec has made significant advances in the field of vibrational relaxation. The dominant work in this area has been by the Kaiser group, although important contributions have also been made by others.[31b,74-76] These experimenters have successfully measured dephasing times in solids[45] and liquids,[44] and energy relaxation and redistribution in pure liquids,[31a] in liquid mixtures,[77] and in solutions.[78] Most recently, these techniques have succeeded in separating the inhomogeneous and homogeneous contributions to dephasing times, and have shown for the first time that inhomogeneous broadening can be substantial in vibrational spectra of liquids.[5] These studies have also shown that the processes

which cause dephasing of coherently prepared ensembles (T_2 processes) are very different from those which cause relaxation of vibrational energy (T_1 processes). The most dramatic example is liquid nitrogen with T_2 = 150 psec[79] and T_1 ~ several seconds.[80]

Molecular crystals are especially interesting candidates for the application of these techniques, although they have been for the most part ignored. For example, measurements of the thermalization of vibrational energy in ground and excited[81] electronic states would be applicable in the theory of radiationless transitions and in the study of electronic energy migration in these systems. From the point of view of coherence a more interesting question is the influence of the crystal periodicity and vibrational energy transfer on relaxation and dephasing processes. As mentioned in the introduction and Part One of this thesis, it may be more appropriate to look at the dynamics from the point of view of either a delocalized or localized picture of the excitation depending on the situation. If resonant energy transfer between an excited molecule and its unexcited neighbors exerts a dominant influence, the effect is to delocalize the excitation over the periodic array of molecules. Scattering by phonons, impurities, and dislocations would play an important role in the dephasing process via their influence on the intermolecular coupling matrix elements and the excited state energy. On the other hand, in the localized picture, the vibrational excitations are restricted to single molecules due to the presence of weak intermolecular interactions or the disruption of these interactions due to uncorrelated thermal motion of the lattice (i.e., strong exciton-phonon scattering). Vibrational dephasing in this picture represents the

loss of the phase relationships established among the excited molecules by the coherent excitation process. This statement also applies to vibrational dephasing in molecular liquids, since their behavior would be expected to be similar in some ways to that described by the localized picture in solids.

With the initial goal of extending picosecond dephasing measurements to include molecular crystals and to eventually begin to answer the questions posed above, a study of dephasing processes has been undertaken in the methylated benzenes 1,2,4,5-tetramethylbenzene (durene) and p-xylene. The first results of these studies are presented in section II. The techniques used are those developed by the Kaiser group and involve excitation of the sample by stimulated Raman scattering of picosecond laser pulses. As discussed below, this feature generally limits the technique to the one mode in a given molecule that is easily excited by stimulated Raman scattering, and the data allows only a limited interpretation to be presented. The data are discussed in terms of the possible contributions to the dephasing <u>including</u> inhomogeneous broadening and are fit to theoretical results obtained by numerical solutions of the differential equations which describe the excitation process. This fitting process allows the determination of dephasing times which are on the order of or somewhat shorter than the laser pulse width.

Studies in the picosecond field have also inspired a flurry of theoretical work[82-88] with the goals of understanding the relevant relaxation pathways and dephasing mechanisms, predicting observed relaxation times, and understanding the large difference between T_1 and T_2. For example, several such models[85-87] treat the system as an excited

harmonic oscillator weakly coupled to a reservoir consisting of a large number of oscillators in thermal equilibrium. The off-diagonal part of the coupling results in decay of the vibrational energy into the reservoir modes, while the diagonal part is responsible for pure dephasing. The dephasing problem has also been treated semiclassically by a model wherein the vibrational phase is modulated by binary collisions with surrounding molecules.[88] These approaches are most applicable to the case of a diatomic molecule in a monatomic solvent or matrix.

In polyatomic molecules, the situation is complicated by the presence of a number of intramolecular degrees of freedom which may interact more strongly with the excited vibrational mode than do the intermolecular modes which comprise the reservoir in the models mentioned above. For example, the redistribution of vibrational energy among other intramolecular modes has been explored experimentally using picosecond techniques,[77,89] and has been shown to play a significant role in even relatively small molecules such as ethanol. However, few theoretical models have incorporated this feature to this author's knowledge. It should be stressed that the inclusion of these effects will be very important for intermediate to large molecules, since the large number of intramolecular modes results in a large density of states at even modest energies. Thus, a large number of potential pathways for the intramolecular redistribution of vibrational energy are present. In addition, it has not generally been realized that interaction with other intramolecular degrees of freedom in polyatomic molecules may dominate dephasing processes as well. This comes about due to random modulation of the vibrational frequency by thermal excitation of low frequency modes

which are coupled to the vibration of interest by intramolecular anharmonic coupling. In Section III experimental support for this statement is presented in the case of dephasing of the C-H stretching vibrations of 1,2,4,5-tetramethylbenzene (durene). The effect of intramolecular modes is monitored using the temperature dependence of the spontaneous Raman spectrum. A theory is outlined which is based on NMR exchange theory and is capable of relating these experimental data to the participating dephasing channels and the nature and strength of the coupling. This approach is also capable of extracting the energy exchange rates in these channels. The formalism is of a general nature and is easily adaptable to situations other than vibrational spectroscopy.

II. Measurement of Dephasing Times by Picosecond Spectroscopy

The ability of intense laser pulses to coherently excite an ensemble of molecules via stimulated Raman scattering[90] is the key to the measurement of vibrational dephasing processes using picosecond spectroscopy.[44] The excitation process is coherent because the stimulated emission of Stokes radiation results in a driving field which excites molecules to a well-defined linear superposition of vibrational states with identical phases (except for phase shifts due to the wavelength of light in the medium). These excited molecules possess the ability to interact with a picosecond probe pulse to produce a coherent beam of anti-Stokes scattered light.[90] This coherent anti-Stokes scattering is emitted toward the direction in space for which the anti-Stokes light scattered by all the molecules is in phase, and its intensity is a measure of the extent of dephasing during the time between the excitation event and the

probing event.

These ideas are illustrated and clarified in Figs. 25 and 26. Speaking in the terminology of the delocalized picture, stimulated Raman scattering excites a vibrational exciton with a well-defined k-vector near k=0 given by $\vec{k}_{vib} = \vec{k}_L - \vec{k}_S$ (see Fig. 25) where $\vec{k}_L$ and $\vec{k}_S$ are the wave vectors of the laser radiation and Stokes radiation respectively. (In the localized picture the wave vector k_{vib} simply represents the well-defined phase relationship among the excited molecules.) Dephasing or T_2 processes are those which cause scattering to a state of different wave vector or mixtures of such states. T_1 processes on the other hand, are those which result in a redistribution of the energy of excitation among other intra- and inter-molecular degrees of freedom. The experimental basis for the measurement of these relaxation times is shown in Fig. 26. The stimulated Raman excitation and probing processes are shown in part (a) of this illustration and the wave vector diagram for the dephasing (T_2) measurement in part (b). In essence, one ensures that the anti-Stokes light is scattered coherently by arranging the experimental geometry such that the wave vectors of the probe pulse ($\vec{k}_p$) and anti-Stokes beam ($\vec{k}_{AS}$) add vectorially to give k_{vib} (which is determined during the excitation process). When this phase-matching condition is met, coherent anti-Stokes light is emitted in the direction $\vec{k}_{AS}$. If the phase matching condition is not met, (i.e., the wave vectors do not add up correctly as in Fig. 26b) only incoherent anti-Stokes scattering can occur. The incoherent scattering depends only on the presence of excited population in the v=1 level and not on any phase relationship. Therefore, its intensity is a measure of the decay or redistribution of vibrational

Figure 25. (a) Some typical dispersion relations for intramolecular vibrations (vibrational excitons) and lattice modes (phonons) are shown schematically. (b) The state prepared by the stimulated Raman scattering excitation process is indicated for this delocalized picture. The double arrows indicate possible relaxation processes. The relaxation time T_1 corresponds to the loss of excited state population to other degrees of freedom, while T_2 corresponds to the loss of phase coherence through scattering of the exciton to other k-states.

DISPERSION AND RELAXATION PROCESSES FOR VIBRATIONAL EXCITONS IN MOLECULAR SOLIDS

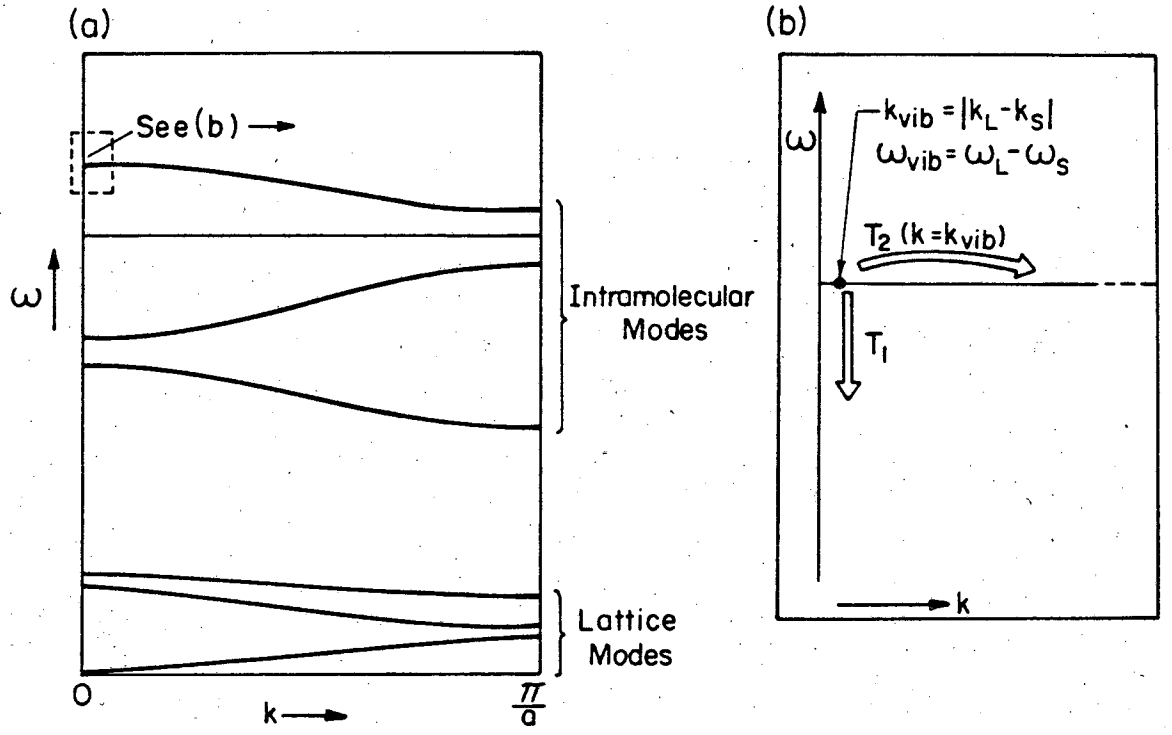

Figure 25

Figure 26. (a) Energy levels involved in Raman excitation and probing are the ground state ($v=0$) and a vibrationally excited state ($v=1$). Excitation involves scattering events in which a laser photon (frequency = ω_L) is absorbed and a Stokes photon (frequency = ω_S) emitted thus transferring population from $v=0$ to $v=1$. In the probing process photons are absorbed from the probe pulse and anti-Stokes photons are emitted (frequencies ω_p and ω_{AS} respectively). Thus the amount of vibrational excitation remaining in $v=1$ can be measured by the intensity of the scattered signal. (b) The wave vector geometry necessary to observe coherent anti-Stokes scattering is shown. k_{vib} is the wave vector of the vibrational excitation prepared by stimulated Raman scattering.

(a) STIMULATED RAMAN SCATTERING: EXCITATION AND PROBING PROCESSES

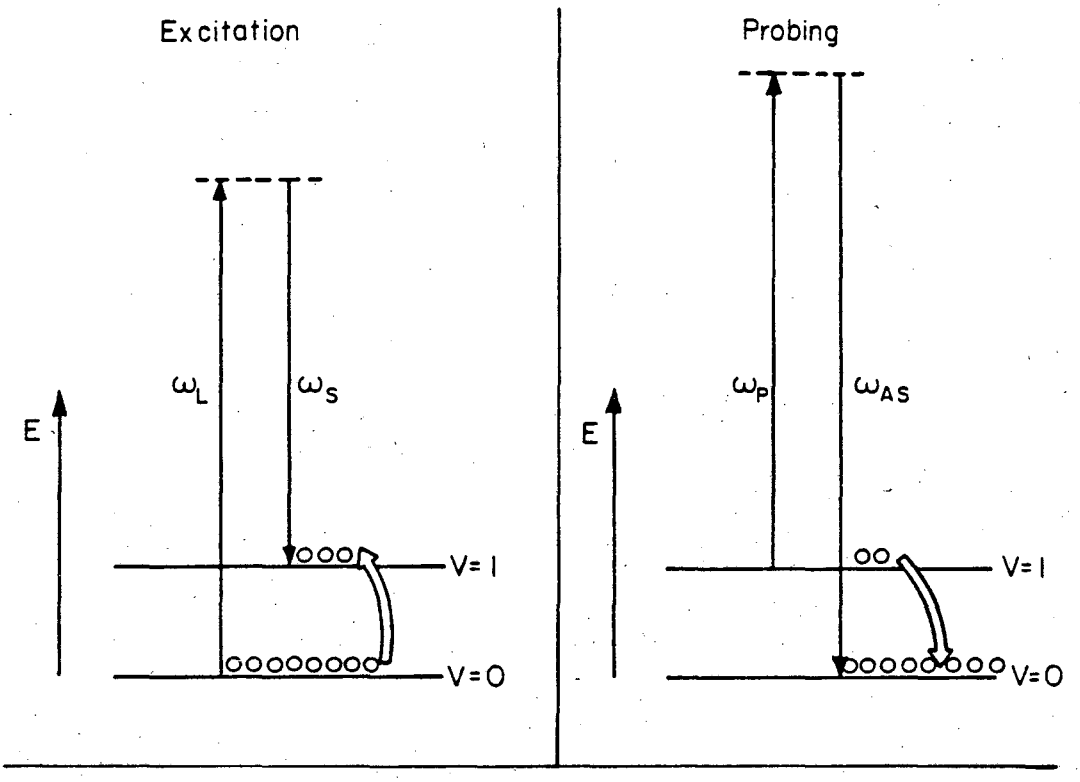

(b) WAVE VECTOR MATCHING GEOMETRY FOR COHERENT ANTI-STOKES SCATTERING

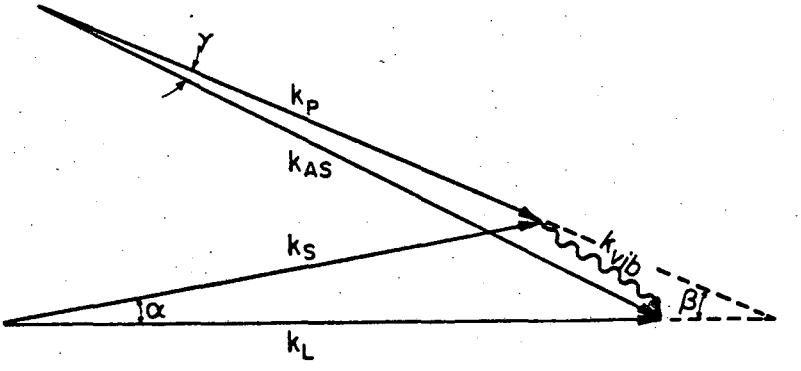

XBL 7612-7944

Figure 26

excitation (T_1 is measured).

The interpretation of these measurements requires an understanding of the stimulated Raman scattering (SRS) excitation and probing processes so that the build-up and decay of vibrational excitation under the influence of the picosecond laser pulse and the intensity of the probe scattering signal can be quantitatively calculated. Therefore, a discussion of these calculations and their theoretical basis is presented in the next section. This is followed by a description of the experimental aspects of the measurement. Finally, in the results and discussion section, the determination of the picosecond pulse shape using coherent Raman scattering in ethanol is described and the dephasing measurements in durene and p-xylene are presented and discussed.

A. Theory of vibrational excitation via stimulated Raman scattering

Raman scattering results due to the modulation of the molecular polarizability by the motion of the nuclei.[91] Quantum mechanically, laser photons of frequency ω_L are absorbed via a "virtual state" with simultaneous emission of a photon of frequency ω_S where $\omega_S = \omega_L - \omega_{vib}$ (see Fig. 26). Classically, the polarizability is modulated at the vibrational frequency, causing side bands to appear in the scattered light at frequencies $\omega_L \pm \omega_{vib}$. If the scattered light is sufficiently intense it can interact with the molecules along with the laser radiation to provide a significant driving force at the beat frequency $\omega_{vib} = \omega_L - \omega_S$. This driving force increases the amplitude of molecular vibration which in turn more strongly modulates the laser radiation. This process results in exponential growth of the Stokes radiation and molecular vibrations

until the laser field begins to become depleted.

The model just described provides the basis for the semi-classical coupled wave description of stimulated Raman scattering. This description has been utilized by many authors since the discovery of SRS,[48,90,92-94] and it follows naturally from a non-linear optics type approach.[51,95] If one hopes to utilize this effect as an excitation source for the purpose of measuring relaxation times it is necessary to be able to calculate the time-dependence of the vibrational excitation. Moreover, this calculation must include the transient response of the molecular oscillator, since the exciting pulse width is on the order of or shorter than the relaxation times. The problem of transient SRS was discussed by Carman, et. al.[94] Because these calculations are crucial in the interpretation of the data to be presented later, this theory will be described here to provide the necessary background.

Theory for Homogeneous Lines

The electric field of the laser and stokes radiation must obey the electromagnetic wave equation:

$$\nabla^2 \vec{E} - (1/c^2) \frac{\partial^2}{\partial t^2} (n^2 \vec{E}) = -\mu_0 \frac{\partial^2 \vec{P}_{NL}}{\partial t^2} \qquad (35)$$

where P_{NL} is the non-linear polarization of the Raman medium and n, the index of refraction of the medium, accounts for the linear polarization of the medium. For the purpose of this calculation the electric field will be represented by a linear combination of infinite plane waves so that the only spatial variation is that in the direction of propagation. Thus, we take:

$$\vec{E}(z,t) = [E_L(z,t) + E_S(z,t)]\,\hat{x} \tag{36}$$

where the laser field is given by

$$E_L(z,t) = 1/2\,\{E_L(z,t)\exp[i(k_L z - \omega_L t)] + c.c.\} \tag{37}$$

and the Stokes field by

$$E_S(z,t) = 1/2\,\{E_S(z,t)\exp[i(k_S z - \omega_S t)] + c.c.\}. \tag{38}$$

The wave equation then reduces to two partial differential equations for the amplitudes E_L and E_S, through the use of the Slowly-Varying Envelope-Approximation (SVEA).[96] In this approximation it is assumed that the amplitudes of the electric field vary little during an optical period so that

$$\frac{\partial^2 E_S}{\partial t^2} << \omega_S \frac{\partial E_S}{\partial t} << \omega_S^2 E_S \tag{39}$$

and similarly for the spatial derivatives. The resulting equation for E_S is:

$$ik_S\left[\frac{\partial E_S}{\partial z} + \frac{n}{c}\frac{\partial E_S}{\partial t}\right]\exp[i(k_S z - \omega_S t)] + c.c. = -\mu_0 \frac{\partial^2 P_{NL}(z,t)}{\partial t^2}. \tag{40}$$

Since in the experiments to be described, the depletion of the laser pulse is only a few percent, it will be assumed that it propagates through the medium undiminished.

The excitation of the molecular vibration is described in terms of an ensemble of two-level systems consisting of the $v=0$ and $v=1$ vibrational levels. This is a realistic approach since:[90] (a) Stimulated

Raman scattering usually only excites the mode with the greatest scattering cross section and therefore the greatest gain for the Stokes radiation, and (b) Anharmonicities prevent levels higher than the v=1 level from participating in the excitation process since $E(v=2) - E(v=1) \neq \hbar\omega_{vib} = E(v=1) - E(v=0)$. The state of the ensemble can be described by a 2×2 density matrix which contains three independent quantities, the magnitude and phase of the off-diagonal elements, and the population difference represented by the diagonal elements. Coherence information is contained in the off-diagonal elements and their relaxation time is given by T_2, the vibrational dephasing time. The experimentally measured quantity is the expectation value of the vibrational displacement which is given by

$$\langle q \rangle = Q[\rho_{01} + \rho_{10}] \tag{41}$$

where $Q = \langle v=1|q|v=0\rangle = (\hbar/2m\omega_{vib})^{1/2}$. This expectation value obeys an equation of motion identical to a classical harmonic oscillator. This can be shown via the Heisenberg equation of motion

$$\dot{q} = i/\hbar\,[\mathcal{H}, q] \tag{42}$$

with the Hamiltonian

$$\begin{aligned}\mathcal{H} &= H_0 - 1/2\,\alpha E^2 \\ &= 1/2\,\hbar\omega_{vib}\,\sigma_3 - 1/2\,(\partial\alpha/\partial q)E^2 Q\sigma_1\end{aligned} \tag{43}$$

where σ_1 and σ_3 are the Pauli matrices for this two-level system. The molecule-radiation interaction term was obtained by expanding the polarizability as a power series in the vibrational coordinate:

$$\alpha = \alpha_0 + (\partial\alpha/\partial q)_0\, q + \cdots \tag{44}$$

and dropping the α_0 term since it cannot cause transitions between the $v = 0$ and $v = 1$ levels.

By applying eq. (42) twice, one obtains

$$\ddot{q} + \omega_{vib}^2 q = \frac{-(n_1 - n_0)}{2m} (\partial\alpha/\partial q)\ E^2 \tag{45}$$

where n_1 and n_0 are the fraction of population in each level. Taking the expectation value and adding a phenomenological damping term, one obtains:

$$\langle \ddot{q} \rangle + 1/T_2 \langle \dot{q} \rangle + \omega_{vib}^2 \langle q \rangle = \frac{-(n_1 - n_0)}{2m} (\partial\alpha/\partial q)\ E^2. \tag{46}$$

To complete the description of the vibrational equation of motion, represent $\langle q \rangle$ as

$$\langle q \rangle = 1/2 \{Q(z,t) \exp[i(k_{vib} z - \omega_{vib} t)] + c.c.\} \tag{47}$$

and calculate E^2 from eq. (36):

$$E^2 = 1/2 \{E_L E_S^* \exp[i[(k_L - k_S) z - (\omega_L - \omega_S) t]] + c.c.\} \tag{48}$$

where only the term which contributes a driving force near ω_{vib} is retained. With these substitutions and with the SVEA for the vibrational field, eq. (46) becomes

$$\frac{\partial Q}{\partial t} (z,t) + Q/T_2 = (i/8\omega_{vib} m)(\partial\alpha/\partial q)\ E_L\ E_S^* \tag{49}$$

where the relations $\omega_{vib} = \omega_L - \omega_S$ and $k_{vib} = k_L - k_S$ have been used. (In other words the physics of the build-up of the vibrational and Stokes waves ensures that $k_{vib} = k_L - k_S$).

To complete the coupled wave description, P_{NL} must be specified in terms of the vibrational excitation. The polarization is given by

$$P_{NL} = \alpha E = N(\partial\alpha/\partial q)\langle q \rangle E \tag{50}$$

where N is the molecular number density. We wish the terms in $(\partial^2 P_{NL}/\partial t^2)$ which vary at the frequency ω_S and thus provide the source term for the Stokes radiation. These are given by

$$-\mu_0(\partial^2 P_{NL}/\partial t^2) = \mu_0 N(\partial\alpha/\partial q)(1/4)\left\{(\omega_L - \omega_{vib})^2 Q^* E_L \right.$$
$$\left. \exp[i[(k_L - k_{vib})z - (\omega_L - \omega_{vib})t]] + c.c.\right\} \tag{51}$$

Thus, the equation for E_S becomes

$$\frac{\partial E_S}{\partial z} + \frac{n}{c}\frac{\partial E_S}{\partial t} = -i\mu_0 N(\partial\alpha/\partial q)(1/4)\frac{\omega_S^2}{k_S} Q^* E_L \tag{52}$$

Equations (49) and (52) are the key equations of this theory. They form a coupled set that have been solved analytically by Carman, et al.[94] The equations are simplified by transformation from the variables z and t to z and t' where $t' = t - zn/c$. E_L is a function only of t' since the laser pulse propagates undepleted, but E_S and Q also depend explicitly on z due to their (approximately) exponential growth. The equations assume the form

$$\partial E_S(z,t')/\partial z = -i\kappa_2 Q^*(z,t') E_L(t') \tag{53}$$

$$\partial Q(z,t')/\partial t' = i\kappa_1 E_S(z,t') E_L^*(t') \tag{54}$$

where

$$\kappa_1 = (1/8\omega_{vib}\, m)(\partial\alpha/\partial q) \tag{55}$$

and

$$\kappa_2 = (\mu_0 N/4)(\partial\alpha/\partial q)(\omega_S^2/k_S) \tag{56}$$

By eliminating one or the other of E_S or Q the equation can be reduced as shown in ref. 94 to a simple form known as the Telegrapher's Equation. The method and details of solution of this partial differential equation are described in ref. 97. The solutions for E_S and Q are:

$$E_S(z,t') = E_S^0(\kappa_1\kappa_2 z)^{\frac{1}{2}} E_L(t') \int_{-\infty}^{t'} dt'' \exp[-(t'-t'')/T_2]$$
$$\left\{E_L^*(t'')\,[\tau(t')-\tau(t'')]^{-\frac{1}{2}}\, I_1\left\{2[\kappa_1\kappa_2 z(\tau(t')-\tau(t''))]^{\frac{1}{2}}\right\}\right\} \tag{57}$$

$$Q^*(z,t') = i\kappa_1 E_S^0 \int_{-\infty}^{t'} dt'' \exp[-(t'-t'')/T_2]$$
$$\left\{E_L^*(t'')\; I_0\left\{2[\kappa_1\kappa_2\, z(\tau(t')-\tau(t''))]^{\frac{1}{2}}\right\}\right\} \tag{58}$$

where $\tau(t') = \int_{-\infty}^{t'} |E_L(t'')|^2\, dt''$, I_0 and I_1 are modified Bessel functions and E_S^0 is a constant which represents the input Stokes field due to spontaneous scattering in the first part of the cell.

One should take note of the approximations and assumptions made in addition to those already mentioned. The medium has been assumed to be dispersionless so that the laser and Stokes waves travel at the same velocity. This is not a severe approximation for most molecular solids and liquids if the path length is only 1 - 2 cm. The requirements on the spatial and temporal coherence of the laser are quite stringent, however,

as several authors have discussed.[45,79,94] For example, in a dispersive medium, the phase modulation and frequency broadening often present in picosecond pulses produced by Nd: glass lasers can strongly effect the SRS gain.[94] Finally, it was assumed that the Raman line consists of a single homogeneously broadened component. This restriction is lifted in calculations discussed below.

Equations (57) and (58) can be easily programmed for the computer using a numerical integration technique such as Gaussian quadrature. An example of the results is shown in Fig. 27. Two points should be noted. First, even when T_2 is short compared to the pulse width, the delay between the maximum of the excitation pulse and the peak of the vibrational excitation depends strongly on the value of T_2. Secondly, when T_2 is short, the build-up and decay of Q^2 is very fast compared to the time variation of the laser pulse itself. As discussed by von der Linde et.al.,[60] this feature is very useful in determining the shape of picosecond pulses.

To calculate the observed signal in the coherent anti-Stokes scattering experiment, the interaction of a picosecond probe pulse with the vibrational amplitude created in the excitation process must be considered.[90] For an incident probe pulse and radiated anti-Stokes wave of the form:

$$E_p(z,t) = \tfrac{1}{2}\{E_p(z,t)\ \exp[i(k_p z - \omega_p t)] + c.c.\} \qquad (59)$$

and

$$E_{AS}(z,t) = \tfrac{1}{2}\{E_{AS}(z,t)\ \exp[i(k_{AS} z - \omega_{AS} t)] + c.c.\} \qquad (60)$$

Fig. 27. (a) Calculated curves for the build-up and decay of the vibrational amplitude, $|Q|^2$, during the stimulated Raman excitation process. These curves were calculated by numerical evaluation of the integral in Eq. (58). Curve #1 corresponds to T_2 = 0.5 psec, #2 to T_2 = 3.0 psec, and #3 to T_2 = 8.0 psec. Notice that the position of the peak of the excitation depends strongly on T_2, and that when T_2 is very short, the pulse of vibrational excitation is much shorter than the laser pulse itself (dotted line). (b) These curves show the expected anti-Stokes probe signal as a function of *delay time* of the probe pulse for the three values of T_2 which were shown in (a). Note that when T_2 is short, it cannot be measured from the decay of this signal, but rather, the signal depends strongly on the shape of the probe pulse. However, T_2 can be obtained semi-quantitatively from the position of the peak signal.

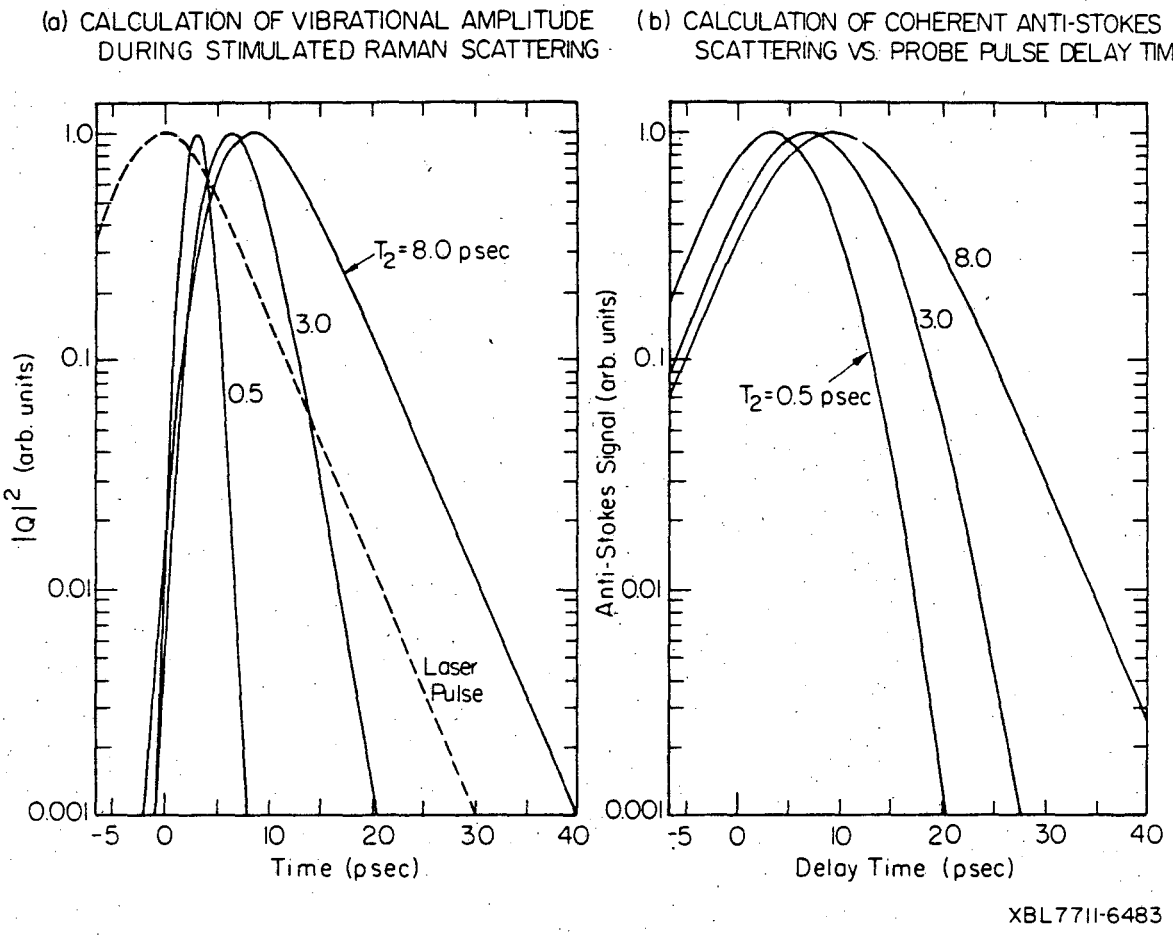
(a) CALCULATION OF VIBRATIONAL AMPLITUDE DURING STIMULATED RAMAN SCATTERING
(b) CALCULATION OF COHERENT ANTI-STOKES SCATTERING VS. PROBE PULSE DELAY TIME
$|Q|^2$ (arb. units)
Time (psec)
T_2=8.0 psec
3.0
0.5
Laser Pulse
Anti-Stokes Signal (arb. units)
Delay Time (psec)
8.0
3.0
T_2=0.5 psec
XBL7711-6483

Figure 27

an equation can be derived for the growth of E_{AS} due to a non-linear polarization resulting from E_P and $\langle q \rangle$. The calculation proceeds along the lines of that leading to Eq. (52) and gives

$$\frac{\partial E_{AS}}{\partial z} + \frac{n}{c}\frac{\partial E_{AS}}{\partial t} = -i\kappa_3 Q(z,t)\, E_P(z,t - t_D)\, \exp[i\Delta k z] \qquad (61)$$

where $\kappa_3 = (\mu_0 N/4)(\partial\alpha/\partial q)(\omega_{AS}^2/k_{AS})$, t_D is the probe pulse delay time, and $\Delta k = k_{AS} - k_P - k_{vib}$. The exponential factor appears since in the probing process phase matching is not automatically provided as in excitation. Since both $Q(z,t)$ and $E_P(z,t)$ are known, this equation can be directly integrated. However, since the main interest is in the value of the time integral for different values of t_D, an approximate z-dependence for $Q(z,t)$ is sufficient. For example, if it is assumed that Q grows exponentially with a characteristic length $\Delta\ell$ one can use:

$$Q(z,t) \approx Q(\ell,t)\, \exp[(z - \ell)/2\Delta\ell] \qquad (62)$$

where ℓ is the path length of the sample. With this substitution the total integrated coherent anti-Stokes signal can be obtained:

$$I_{coh}(t_D) = \int dt' |E_{AS}(t')|^2 \qquad (63)$$

$$= 4\kappa_3^2 (\Delta\ell)^2 [1 + (2\Delta k \Delta\ell)^2]^{-1} \int_{-\infty}^{\infty} dt' \; |E_P(t' - t_D)|^2 \; |Q(t')|^2$$

The z-integration causes a variation in the signal for different values of the wave vector mismatch, Δk, while the t-integration results in a convolution of the probe intensity and the square of the vibrational amplitude. Thus, for T_2 values long compared to the probe pulse, one observes a decay in the signal with a 1/e time of $T_2/2$. When T_2 is short,

$|Q|^2$ acts as a delta function and the anti-Stokes signal can be used to map out the shape of the probe pulse. When T_2 is short enough that the decay cannot be directly measured, it is possible to determine a semi-quantitative value from the delay time between the peak of the excitation pulse and the peak anti-Stokes signal (see Results and Discussion section and Fig. 27(b)).

Theory for Inhomogeneous Lines

If the Raman line is inhomogeneously broadened, it should be kept in mind that the apparent decay time of the coherently scattered probe signal may reflect the inhomogeneous linewidth rather than the true dephasing time of the molecular vibrations. In order to include the effects of an inhomogeneous distribution, the above theoretical description must be modified. This problem has been discussed by Laubereau, et.al.[98] and solved approximately in the limit where the inhomogeneous linewidth is smaller than the reciprocal of the picosecond pulse width. Qualitatively, they find that each individual homogeneously broadened component or "isochromat" builds up and decays almost exactly as if the inhomogeneous broadening were absent, although the vibrational amplitude of each component acquires a slightly different phase from the others. Once the excitation pulse is past, each component evolves at its own vibrational frequency. When the total ensemble average vibrational amplitude is monitored, the effect is a rapid decay due to destructive interference among the various isochromats, or in cases where only a few frequencies are present, an interesting "beating" effect.[98,99]

Since it would be helpful to be able to calculate these effects in more general situations, a slightly different approach is adopted here. Rather than restricting the scope of the calculation to a certain limiting situation in order to facilitate an analytical solution, the coupled equations for the Stokes field and the N_v vibrational amplitudes were solved directly by an iterative numerical computation. The equations to be solved are those discussed above, with modification to include the inhomogeneous distribution. The vibrational amplitude becomes:

$$\langle q \rangle = \sum_{j=1}^{N_V} N_j Q_j \exp[i(k_{vib} z - \omega_{vib} t)] \tag{64}$$

where N_j is the number density of molecules with vibrational frequency $\omega_{vib} + \Delta\omega_j$. The amplitudes Q_j are complex. In the transient limit, one expects the molecules to oscillate with their individual frequencies and Q_j takes on the oscillatory dependence $Q_j \sim \exp[-i\Delta\omega_j t]$, while in the steady state limit the oscillators would follow the driving field, and Q_j would approach a constant complex value. Since each oscillator reacts independently to the driving field, its equation of motion is

$$\frac{\partial Q_j}{\partial t} + \Gamma_j Q_j = i\kappa_1 E_S^* E_L \tag{65}$$

where $\Gamma_j = i\Delta\omega_j + 1/T_2$. The complex part of Γ_j introduces the amount each isochromat is off-resonance from the driving frequency ω_{vib}. The non-linear polarization, on the other hand, has contributions from all of the oscillators. Thus, the equation for E_S is:

$$\frac{\partial E_S}{\partial z} + \frac{n}{c} \frac{\partial E_S}{\partial t} = -i\kappa_2 E_L [\sum_j (N_j/N) Q_j] \tag{66}$$

By transforming to the new time coordinate $t' = t - zn/c$ and differentiating Eq. (65) with respect to z, E_S can be eliminated to give

$$\frac{\partial^2 Q_j(z,t')}{\partial z\, \partial t'} + \Gamma_j \frac{\partial Q_j(z,t')}{\partial z} = i\kappa_1 E_L(t') \frac{\partial E_S(z,t')}{\partial z}$$

$$= \kappa_1 \kappa_2 |E_L(t')|^2 \left[\sum_m (N_m/N) Q_m\right] \quad (67)$$

Integrating with respect to t', one obtains

$$\frac{\partial Q_j(z,t')}{\partial z} = \kappa_1 \kappa_2 \int_{-\infty}^{t'} dt'' \exp[-\Gamma_j(t' - t'')] |E_L(t'')|^2 \left[\sum_m (N_m/N) Q_m(z,t'')\right] \quad (68)$$

which has the form of a coupled set of differential equations in the discreet index j and the continuous index t'. The initial conditions are given by the integral of Eq. (65) with $E_S(0,0) = E_S^o$ = constant:

$$Q_j(0,t') = i\kappa_1 E_S^o \int_{-\infty}^{t'} dt'' \exp[-\Gamma_j(t' - t'')]\, E_L(t'') \quad (69)$$

This problem can be solved by a numerical technique such as Euler's method or the more accurate (but time-consuming) Runge-Kutta method.[100] Finally, the coherent probe scattering signal can be evaluated as a sum of contributions from each isochromat, each of which has its own value of Δk_j, the wave vector mismatch. This mismatch may have a contribution due to the oscillatory dependence of Q_j. The extent of this contribution will depend on whether a given situation more closely approaches the steady-state or transient limit. In the truly steady-state case there is no oscillatory dependence of Q_j because the molecular vibrations follow

the driving field and all oscillate with the frequency ω_{vib}. In the transient limit, however, each isochromat scatters anti-Stokes light with a different frequency shift resulting in a different wave vector for each component of the scattered light, and thus a different wave vector mismatch. In any case, the integrated anti-Stokes signal is given by a calculation similar to that leading to Eq. (63):

$$I_{coh}(t_D) = 2\kappa_3^2(\Delta\ell)^2 \int_{-\infty}^{\infty} dt' |E_P(t' - t_D)|^2 \left| \sum_j \{(N_j/N)\, Q_j(t') \times \exp[-i \tan^{-1}(2\Delta k_j \Delta\ell)][1 + (2\Delta k_j \Delta\ell)^2]^{-1}\} \right|^2 \quad (70)$$

where $\Delta k_j = k_L - k_S - k_{ASj} + k_P$. Experimentally, Laubereau[98,99] distinguishes two situations denoted by "selective" and "non-selective" wave vector matching. By appropriately restricting the experimental geometry, it is possible to make one term in the sum over j in Eq. (70) dominate due to the factor $[1 + (2\Delta k_j \Delta\ell)^2]^{-1}$. This selective geometry monitors the decay of a single isochromat and thus is the basis for a measurement of the homogeneous dephasing time. In a non-selective geometry, all terms in the sum contribute, and effects due to interference of the different isochromats are possible. To illustrate these calculations, an example of the anti-Stokes signals and vibrational amplitudes expected from an inhomogeneous line of eleven isochromats is shown in Fig. 28. These curves were calculated using the numerical solution technique described above. With these computational techniques at one's disposal, it is possible to compare the calculated curves with experimentally measured data for the coherent anti-Stokes scattering experiment.

Fig. 28. (a) The build-up and decay of the vibrational amplitudes for an eleven component inhomogeneous line are shown. The isochromats are separated by 4 cm^{-1} and have equal homogeneous dephasing times of T_2 = 5 psec. The relative intensities of the isochromats are in the ratio 0.22 : 0.31 : 0.45 : 0.67 : 1.0 : 0.67 : 0.45 : 0.31 : 0.22. Curve #1 shows $|Q|^2$ for an individual isochromat while curve #2 shows $|\sum_j Q_j|^2$, the total vibrational amplitude of all components. The frequency of the beats is related to the spacing chosen for the eleven isochromats. The dotted line shows the time dependence of the excitation pulse. (b) The anti-Stokes signal expected from the vibrational amplitudes in (a) is shown as a function of probe pulse delay time. Curve #1 corresponds to the use of selective wave vector matching conditions to observe the decay of a single component, while curve #2 is for non-selective wave vector matching, and contributions from all components are observed. Note that the width of the probe pulse does not allow the beats in (a) to be resolved by the probing process.

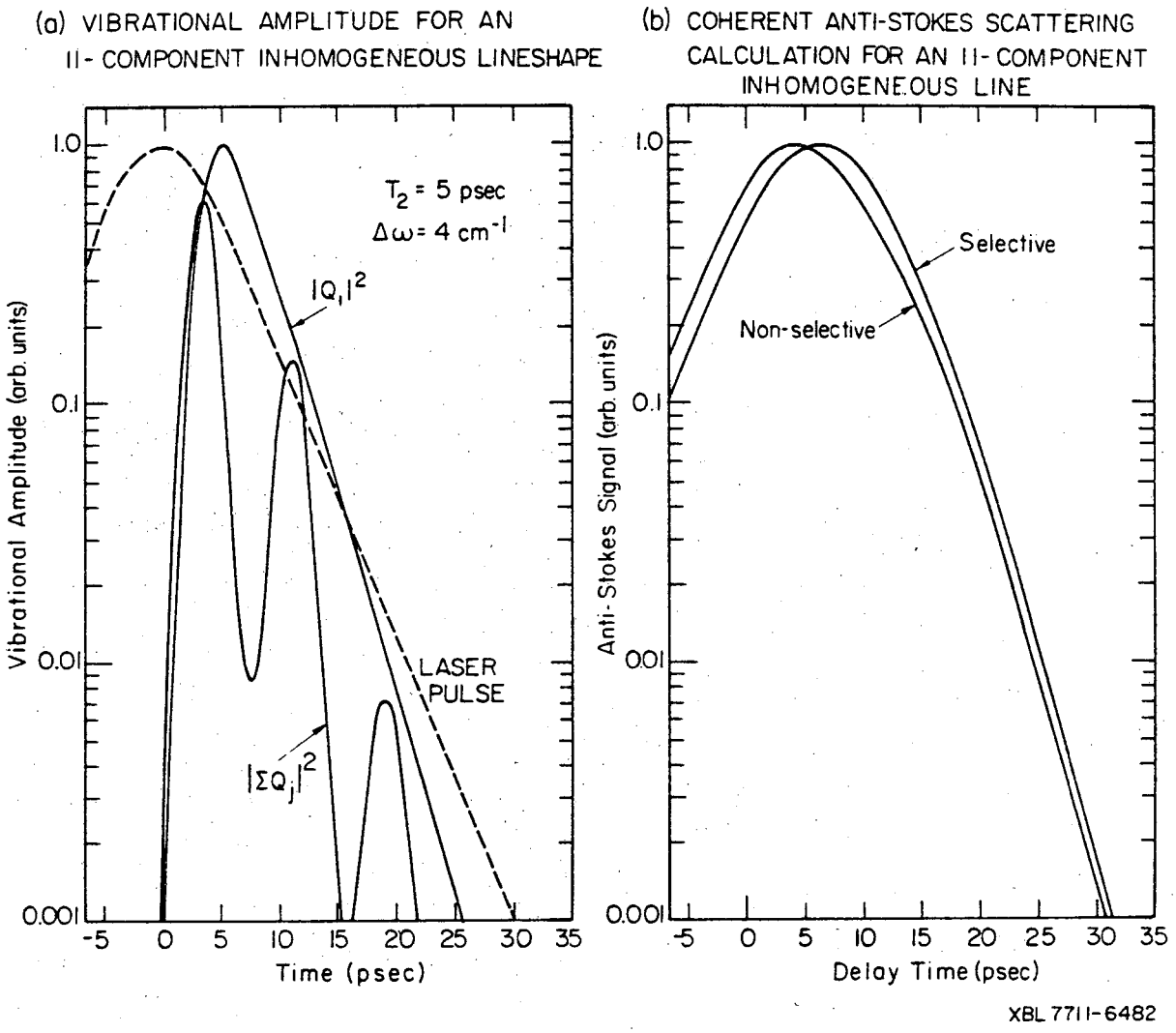
(a) VIBRATIONAL AMPLITUDE FOR AN
11-COMPONENT INHOMOGENEOUS LINESHAPE
T_2 = 5 psec
$\Delta\omega$ = 4 cm^{-1}
$|Q_1|^2$
LASER
PULSE
$|\Sigma Q_j|^2$
Vibrational Amplitude (arb. units)
1.0
0.1
0.01
0.001
-5 0 5 10 15 20 25 30 35
Time (psec)
(b) COHERENT ANTI-STOKES SCATTERING
CALCULATION FOR AN 11-COMPONENT
INHOMOGENEOUS LINE
Selective
Non-selective
Anti-Stokes Signal (arb. units)
1.0
0.1
0.01
0.001
-5 0 5 10 15 20 25 30 35
Delay Time (psec)
XBL 7711-6482

Figure 28

B. Experimental

Sample Preparation

Ethanol used in the pulse shape determination was Rossville Gold Shield alcohol and was used directly from the container. Trichloroethane was MCB reagent grade. p-xylene was MCB reagent grade and was further purified by chromatography on an alumina column. Durene purchased from Eastman Organic Chemicals was recrystallized from ethanol and zone refined for 100 passes. This purification process resulted in good optical quality crystals which were grown using the Bridgman technique. The crystals were annealed for one week at 1°C below their melting point to further improve the optical quality and reduce scattered light. For liquid durene samples, the recrystallized material was used in a quartz cell with facility for passing heated water from a constant temperature bath through a water jacket. This procedure maintained the durene at a pre-determined temperature above its melting point.

The crystal parameters of durene are well known.[101] The crystal structure is monoclinic with space group ($P2_1/a$) and contains two molecules per unit cell with site symmetry C_i. The crystals were oriented as follows: Durene cleaves easily along the 001 plane which is usually parallel to the axis of crystal growth. The crystals are optically biaxial with the optic plane 010.[102] Thus two extinctions are seen when the crystal is observed between crossed polarizers with the light path perpendicular to the cleavage plane. Using a polarizing microscope, it was found that the crystallographic b axis corresponds to the extinction direction which makes approximately a 67° angle with respect to the growth axis.

The cleaved faces of the crystals were used as the entrance and exit windows for the laser beam. If a very good cleavage was obtained, no polishing of the faces was needed. If necessary for good optical quality, the crystal was solvent polished using a lens tissue wetted with benzene on a flat glass plate. Since durene readily sublimes at room temperature, the crystals were kept in a stoppered tube when not actually being used in an experiment. Repolishing was usually necessary after about 8-10 hours exposure to the air. The crystals were mounted on glass rods with epoxy cement for the purpose of positioning and orienting them in the experimental set-up.

The durene crystals used in these experiments had optical path lengths of from eight to ten millimeters. The liquid durene, ethanol and trichloroethane samples were contained in quartz-windowed cells of 10 mm path length, and the p-xylene sample was contained in a similar 20 mm path length cell.

Optical Arrangement

The picosecond light source used in these experiments was the Nd: glass mode-locked laser system described in Part Two of this thesis. After frequency doubling, the remaining 1.06μ light was filtered out and the second harmonic single pulse was directed into the experimental set-up shown schematically in Fig. 29. This arrangement is similar to that developed by the Kaiser group.[44]

The operation of the optics is as follows: A small portion (~5%) of the vertically polarized second harmonic pulse is extracted by an uncoated wedged quartz flat beam splitter for use as the probe pulse.

Fig. 29. Diagram of the set-up used for the dephasing time measurement. BS = beam splitter; DL = optical delay line; T_1 and T_2 = Gallilean telescopes; F_1, F_2, and F_3 = filters; $\lambda/2$ = quartz half-wave plate; PMT_1, PMT_2, and PMT_3 = photomultiplier tubes which monitor the laser intensity, Stokes intensity and anti-Stokes intensity respectively; S = sample; SP = 3/4 m spectrometer; and A = aperture.

MEASUREMENT OF VIBRATIONAL DEPHASING TIME (T_2) USING COHERENT ANTI-STOKES SCATTERING

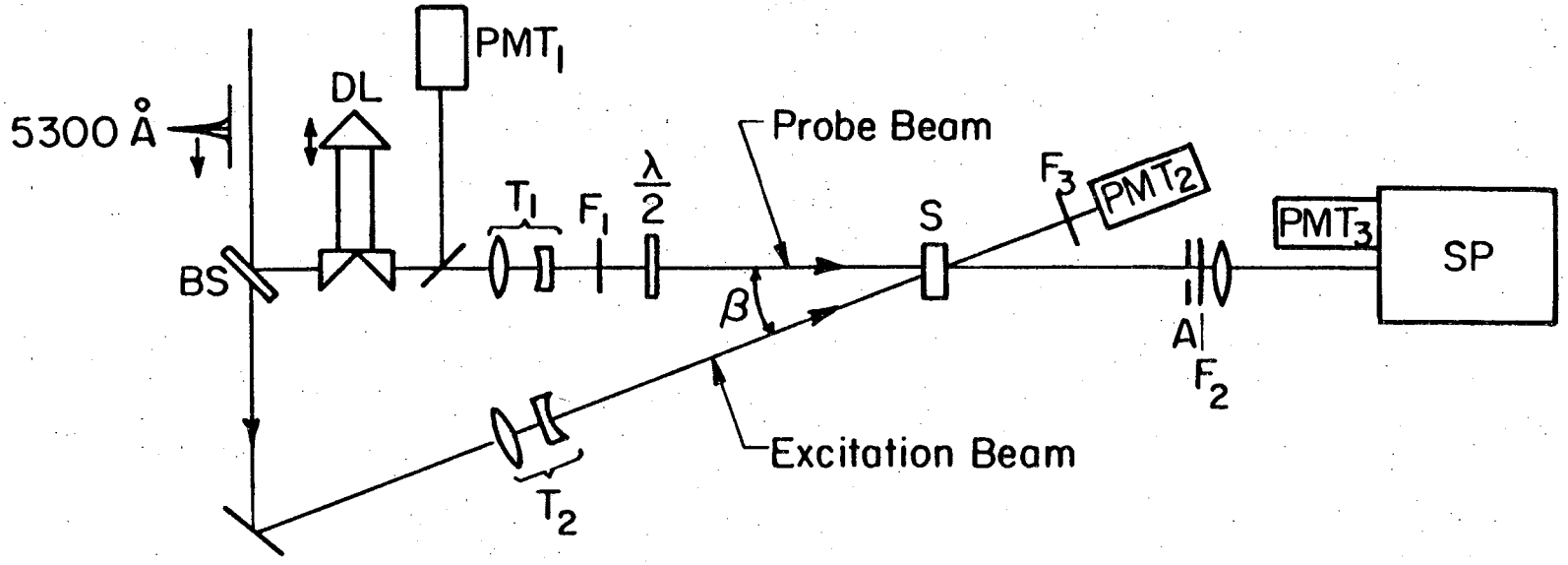

Ref: von der Linde, Laubereau and Kaiser, Phys. Rev. Lett., 26, 954 (1971)

XBL7612-7941

Figure 29

The remaining 90+% of the energy is collimated into the sample by the Galilean telescope (labeled T_2 in Fig. 29) which produces an approximately Gaussian beam with beam waist at the sample and allows the spot size to be adjusted between ~0.5 mm and ~2 mm diameter (measured at the 1/e points). The intensity of the Stokes radiation generated in the sample is measured by the phototube PMT_2. Filter F_3 consists of Schott 0G570 and 0G590 filters and appropriate neutral density filters. A Glan-Thompson polarizer in the excitation beam just before the sample ensures highly vertically polarized light. The probe pulse delay is controlled by an adjustable three-prism delay line. The adjustable prism is mounted on a Lansing translation stage and the optical path length setting can be easily reproduced to within 0.01 mm. PMT_1 monitors the intensity of the probe pulse, and another telescope of similar design collimates the probe beam into the sample. A quartz $\lambda/2$ plate rotates the polarization of the probe beam 90° so that the polarization of the anti-Stokes scattered probe light can be used to distinguish it from anti-Stokes light produced by the much more intense excitation pulse. Filter F_1 (Schott GG495) ensures that any interfering radiation near the wavelength of the anti-Stokes signal is eliminated. The anti-Stokes signal is selected spatially by an aperture and the 5300 Å probe light is removed by two 4600 Å Ditric Optics 3-cavity interference filters. Any troublesome signal from the exciting beam is removed by a sheet-type polarizer oriented opposite to the Glan polarizer in the exciting beam. The signal is then focused on the slit of a Spex 3/4 m monochrometer and detected in first order with an EMI 6256S photomultiplier. The data shown below was collected with

a slit width of 600 microns.

The alignment of the experiment is done initially with the He-Ne beam from the alignment laser. With careful adjustment of the He-Ne beam and good laser alignment the two are usually quite closely coincident. The coincidence can be monitored via the burn spots made by the 5300 Å beam on a piece of Polaroid film inserted in the beam for this purpose. The excitation and probe He-Ne beams are made to cross near the exit face of the sample. This adjustment is made while viewing the He-Ne beams as they exit from the sample with a 30× microscope. In this way the beams can be accurately overlapped. The depth of field of the microscope is a fraction of a millimeter, and the two beams are made to coincide when the microscope is focused about 0.5 mm inside the sample. One should also check at this point to make certain that the position of the probe beam does not move as the delay line prism is translated. The detectors and monochromator are then aligned, and all filters inserted. When the sample is a crystal of durene, the crystal is oriented with the excitation pulse-polarization perpendicular and the probe pulse polarization parallel to the crystal b axis. This was determined by viewing the He-Ne beam after it had passed through the polarizer in the excitation path, the crystal, and a polarizer oriented 90° with respect to the first one. The crystal is then mounted such that the maximum extinction of the He-Ne light was obtained.

The wave vector matching angle β is determined by the experimental geometry as indicated in Fig. 29. The range of possible values for α and γ (see Fig. 26) is determined by the divergence of the emitted Stokes

radiation and the angle of acceptance of the anti-Stokes collection optics respectively. The Stokes divergence is determined by the excitation beam diameter and sample path length, since these factors restrict those directions in space for which a Stokes ray traverses the maximum distance within the irradiated part of the sample. At least two of these angles are necessarily non-zero for perfect phase matching because of the dispersion of the sample medium. For the molecules studied here β was chosen to be ~8° since γ is then near zero. The excitation and probe beam diameters were approximately 1.5 mm and were measured with a Reticon photodiode array. The corresponding Stokes divergence combined with a 1° acceptance angle for the anti-Stokes beam constitutes relatively non-selective phase matching geometry, in that phase matching is allowed for a range of vibrational frequencies greater than the spontaneous Raman linewidths of the vibrations investigated.

Excitation pulse energies were in the 1-2 mJ range. This gives a power density of from 10 to 20 gigawatt per square centimeter. The conversion efficiency of the excitation process was measured using photomultipliers which were calibrated with a Hadron model 100 thermopile and corrected for relative quantum efficiency, filters, etc. The conversion of excitation energy to Stokes radiation was found to be about 0.5% to 1%. The vibrational mode which was excited by the stimulated Raman process was identified by measurements of the stimulated Raman spectrum of the molecules investigated. The spectra were recorded on photographic film or on the PAR optical multichannel analyzer coupled to a Spex 3/4 m spectrograph.

Data Collection

The peak signal from the photomultipliers (time constant 1 msec) was captured by sample and hold circuits and digitized by the data acquisition system described in Part Two. These signals represent the integrated energy of the laser pulse and the Raman scattered light. The resulting digital data was used by the data acquisition system to normalize the anti-Stokes signal for each shot. Since each excited molecule gives rise to one Stokes photon, the Stokes pulse energy is a measure of the number of excited molecules. Therefore, the anti-Stokes signal is normalized to the probe intensity and the vibrational excitation using the formula:

$$I_{coh}(t_D) = \frac{I_{AS}}{I_S \cdot I_L} \tag{71}$$

where I_{AS} and I_S are proportional to the anti-Stokes signal and the Stokes energy, and I_L is proportional to the probe pulse energy. The results of at least five acceptably mode-locked laser shots (each pulse train was monitored with an H.P. PIN photodiode and Tektronix type 519 oscilloscope) were averaged to obtain the data point for each probe delay time. The error bars shown in the figures below represent an estimate of the error given by the standard deviation of this average.

Spontaneous Raman Scattering

The spontaneous Raman spectra shown in this work were recorded using a Jobin-Yvon Ramanor double monochrometer. A Coherent Radiation model CR-3 argon ion laser operated on the 4880 Å line and suitably

filtered to eliminate plasma lines was used as the excitation source. Detection was with an RCA C31034 photomultiplier and Princeton Applied Research Quantum Photometer photon counter. The slitwidth of 50 microns on the exit and entrance slits and 75 microns on the intermediate slits provided a resolution of better than 1 cm^{-1}. The spectra of solid durene were recorded with a powder sample, and of solid xylene with a polycrystalline sample obtained by fairly rapid freezing (~10 sec). For the low temperature work the samples were sealed in pyrex tubes (~2 mm ID) under vacuum after several freeze-pump-thaw degassing cycles. These tubes were mounted in a copper sample holder which was in turn mounted on an Air Products Displex closed cycle helium refrigerator cold tip. Indium shims between the Pyrex tube and the sample holder helped to establish thermal contact. The temperature was monitored with an iron-doped gold vs. chromel-P thermocouple using an ice-bath reference junction and Data Precision digital voltmeter. The temperature of the sample was controlled by passing current through a heater wrapped around the sample end of the cold tip. The temperature could be varied in this way between ~9°K and ~270°K.

C. Results and discussion

In order to characterize the response of the experimental apparatus, including the effects of the laser pulse shape and to demonstrate the procedure used in fitting the experimental data with calculated curves, some vibrations with known dephasing times were investigated. Data for the coherent anti-Stokes scattering experiment on the 2921 cm^{-1} vibration

of ethanol and the 2941 cm^{-1} vibration of 1,1,1-trichloroethane are presented in Fig. 30 and Fig. 31. These liquids have been previously investigated both with spontaneous Raman scattering and with picosecond techniques, and their dephasing times (T_2) have been reported as 0.52 psec[44] and 2.6 psec[31a] respectively. Using this value for the ethanol dephasing time, the best fit to the data by the curve calculated from Eqs. (58) and (63) was determined by adjusting the pulse shape function $E_L(t')$. As discussed earlier, the short dephasing time of ethanol makes this experiment quite sensitive to the pulse shape. As demonstrated in the calculation shown in Fig. 27a, above, the vibrational excitation for T_2 = 0.5 psec rises and decays rapidly compared to the picosecond pulse width. Thus, it behaves as a delta function as far as the integral in Eq. (63) for the anti-Stokes signal is concerned, and the anti-Stokes signal as a function of the delay time is an excellent approximation to the pulse shape. By using various trial functions, it was found that a suitable fit was obtained with a pulse shape given by

$$I_L(t') = |E_L(t')|^2 = \begin{cases} \exp[-(t'/6.34\ \text{psec})^2] & \text{for } t' \leq 0 \\ \\ \text{sech}[t'/3.94\ \text{psec}] & \text{for } t' \geq 0 \end{cases} \qquad (72)$$

where $t' = t - zn/c$. This pulse shape has a rapidly rising (gaussian) leading edge and an exponential trailing edge, and its use results in the calculated curve shown in Fig. 30. This fitting procedure also served to determine the location of the $t_D = 0$ point.

Once the pulse shape has been determined in this way, data from other samples can be fitted using T_2 as the only adjustable parameter.

Fig. 30. Coherent anti-Stokes scattering data for the C-H stretching mode of ethanol. The normalized anti-Stokes signal is plotted as a function of probe pulse delay time. The theoretical fit indicates that our laser pulse intensity can be represented as a Gaussian rise [$I_L = I_o \exp(-t/6.34 \text{ psec})^2$) for $t \leq 0$] and an exponentially falling tail [$I_L = I_o \text{ sech}(t/3.94 \text{ psec})$ for $t \geq 0$].

Fig. 31. The coherent anti-Stokes data for the 2941 cm^{-1} vibration of 1,1,1-trichloroethane is shown. The data can be fit by assuming a value of $T_2 = 3.5$ psec which is to be compared with the accepted value of 2.6 psec. The calculated curve expected for a dephasing time of 0.5 psec (e.g. ethanol) is also shown for comparison.

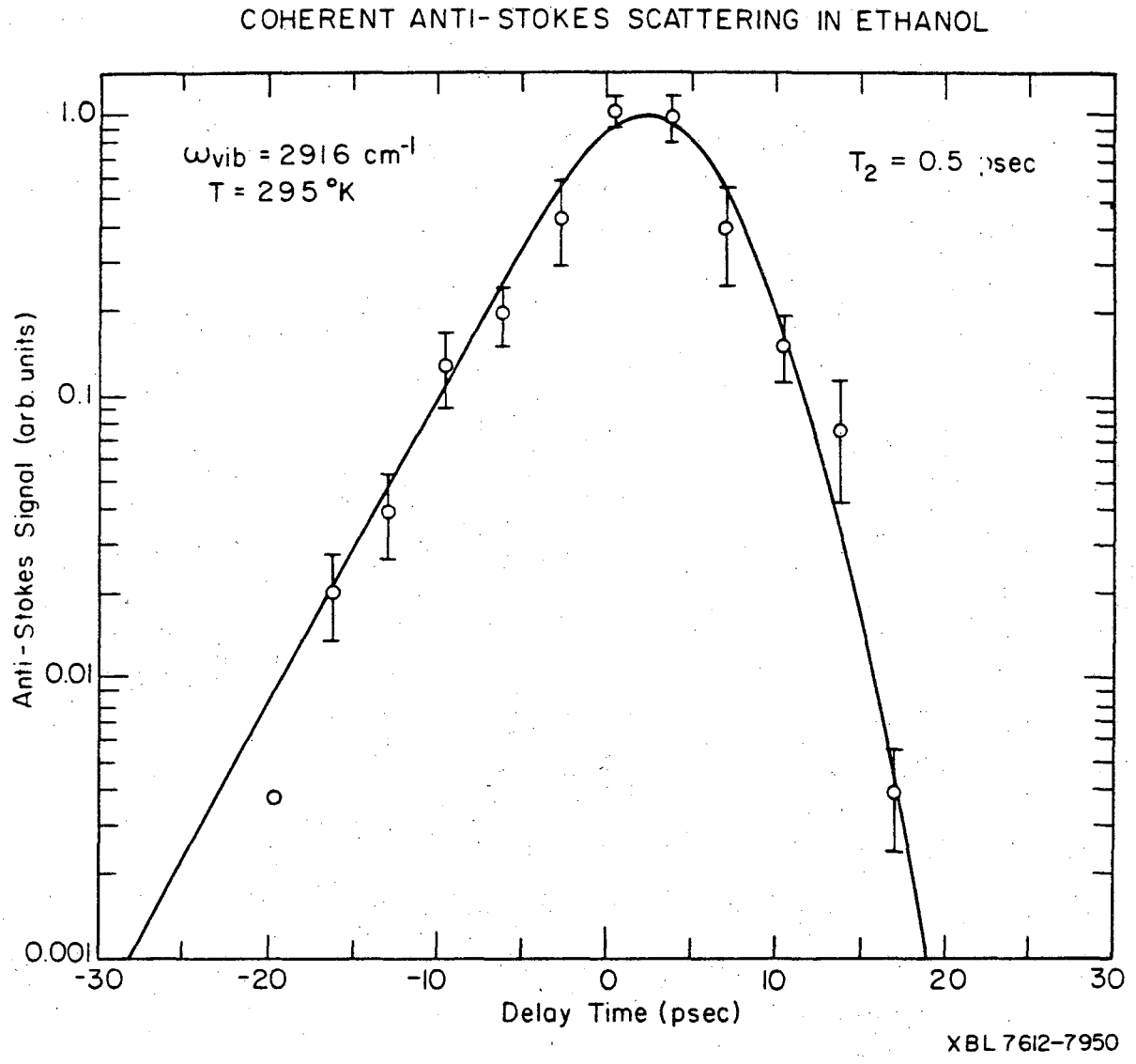
COHERENT ANTI-STOKES SCATTERING IN ETHANOL
ω_{vib} = 2916 cm^{-1}
T = 295 °K
T_2 = 0.5 psec
Anti-Stokes Signal (arb. units)
1.0
0.1
0.01
0.001
-30
-20
-10
0
10
20
30
Delay Time (psec)
XBL 7612-7950

Figure 30

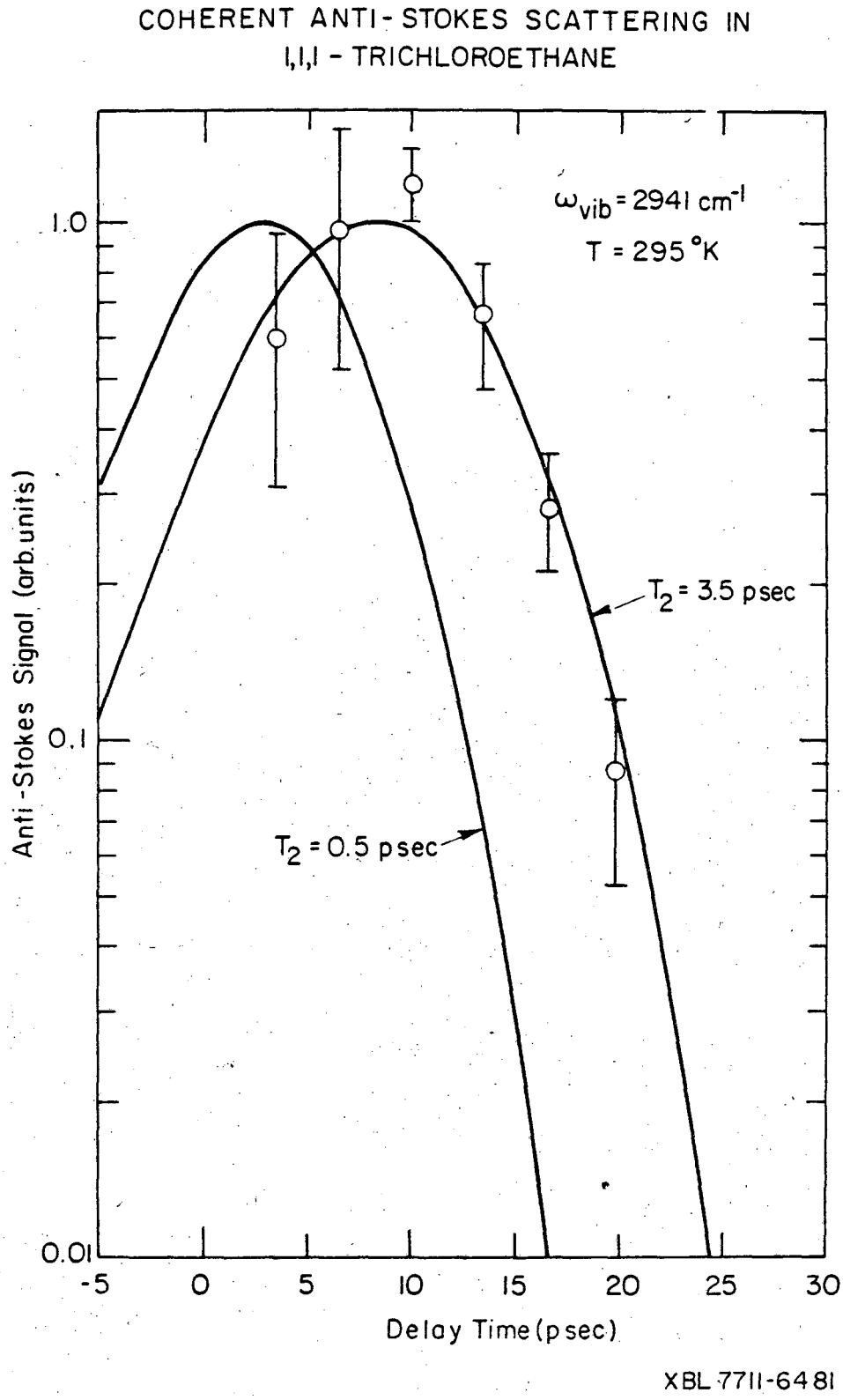
COHERENT ANTI-STOKES SCATTERING IN
1,1,1 - TRICHLOROETHANE
ω_{vib} = 2941 cm^{-1}
T = 295 °K
T_2 = 3.5 psec
T_2 = 0.5 psec
Anti-Stokes Signal (arb.units)
1.0
0.1
0.01
-5
0
5
10
15
20
25
30
Delay Time (psec)
XBL 7711-6481

Figure 31

This method is capable of estimating T_2 even when the dephasing time is comparable to or somewhat shorter than the pulse width. The reason for this is that the probe delay required to give the peak signal increases as T_2 increases. This delay is calibrated fairly accurately by the fitting process, especially when experimental data is available for several orders of magnitude below the peak. Thus, this process is somewhat different than the usual deconvolution procedure commonly used to obtain short decay times in the presence of a long excitation pulse in that the information is contained in the position of the peak signal rather than in the tail of the decay. Thus, the sensitivity of this delay to the value of the dephasing time determines the accuracy of the technique. However, the fitting procedure depends on several additional assumptions. First, the pulse shape must be reproducible. Second, Eq. (58) depends on parameters of the active medium, namely the Raman gain. Therefore, the Stokes conversion efficiency as well as other experimental parameters should be reproduced as closely as possible from sample to sample to compensate for such differences. In practice, one tries to estimate the probable accuracy of such a determination of T_2 based on the sensitivity of the fit to different values of these parameters. From these considerations, a possible error of a factor of two seems reasonable for the range of dephasing times studied here (0.5 - 4 psec). For example, the apparent decay time of the experimental data for 1,1,1-trichloroethane in Fig. 31 indicates that $T_2 < 5$ psec. However, by fitting the data as described above, the best value of T_2 is determined to be $T_2 = 3.5$ psec. This value and the previously determined value of 2.6 psec are within the factor of two estimated margin of error. This technique was also applied in the

case of the 2914 cm^{-1} vibration of solid and liquid durene, and liquid p-xylene (2912 cm^{-1} vibration). The data, fitted curves and corresponding values of T_2 are shown in Figs. 32, 33, and 34. The crystal data represents the first direct picosecond measurement of a vibrational dephasing time in an organic molecular crystal.

The T_2 values obtained for the durene samples are 0.5 psec for the liquid and 0.75 psec for the single crystal. Since these values are essentially the same to within the estimated error, it would appear that the dominant dephasing mechanism is independent of the translational symmetry of the crystal in the case of this particular mode. Therefore, the dephasing time should not be interpreted in terms of scattering of delocalized excitons by phonons and is probably not directly related to vibrational energy transfer in these systems. This is not surprising since the lattice vibrations are highly excited at room temperature and effectively disrupt the translational symmetry. For the case of a Raman-active mode such as this one with zero transition dipole moment and sub-picosecond dephasing time, any energy transfer processes would probably take place via an incoherent hopping motion. Thus, if it is true that the vibrational energy dynamics in the room temperature solid and liquid are similar as this admittedly minimal piece of data seems to indicate, it should not come as a surprise. However, a more definitive statement than this cannot be made at this time.

One must then consider what possible mechanisms are responsible for dephasing of this mode. Several authors have discussed dephasing in terms of coupling with degrees of freedom of the bulk crystal or liquid

Fig. 32. Coherent anti-Stokes data for the 2914 cm^{-1} vibration of durene measured in a single crystalline sample at room temperature can be fit with a dephasing time of T_2 = 0.75 psec.

Fig. 33. Coherent anti-Stokes data for the 2914 cm^{-1} vibration of liquid durene. The theoretical fit to the data gives T_2 = 0.5 psec in this case.

Fig. 34. Coherent anti-Stokes data for the 2912 cm^{-1} vibration of p-xylene. The value of T_2 determined in this case is 2.2 psec.

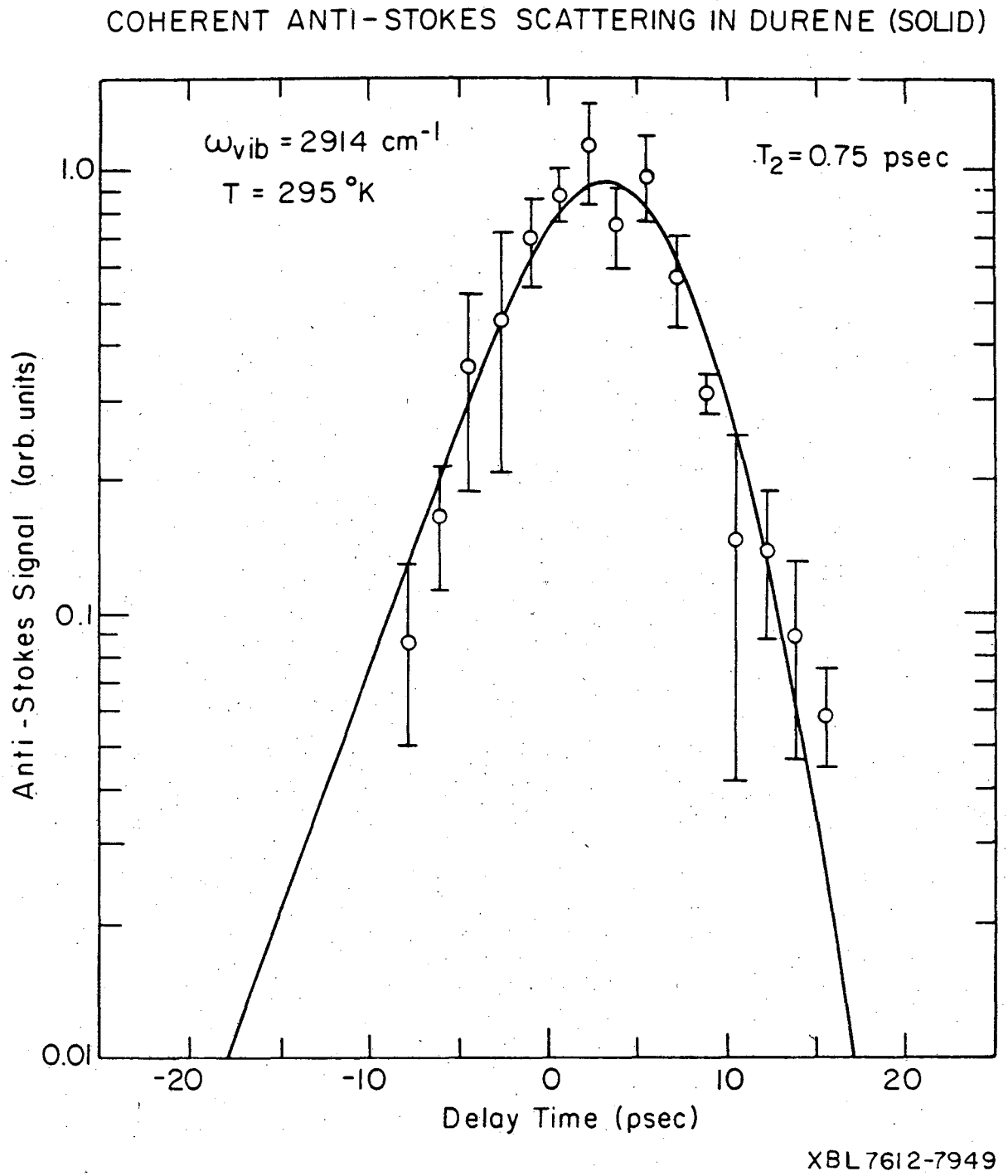
COHERENT ANTI-STOKES SCATTERING IN DURENE (SOLID)
ω_{vib} = 2914 cm^{-1}
T = 295 °K
T_2 = 0.75 psec
Anti-Stokes Signal (arb. units)
1.0
0.1
0.01
-20
-10
0
10
20
Delay Time (psec)
XBL7612-7949

Figure 32

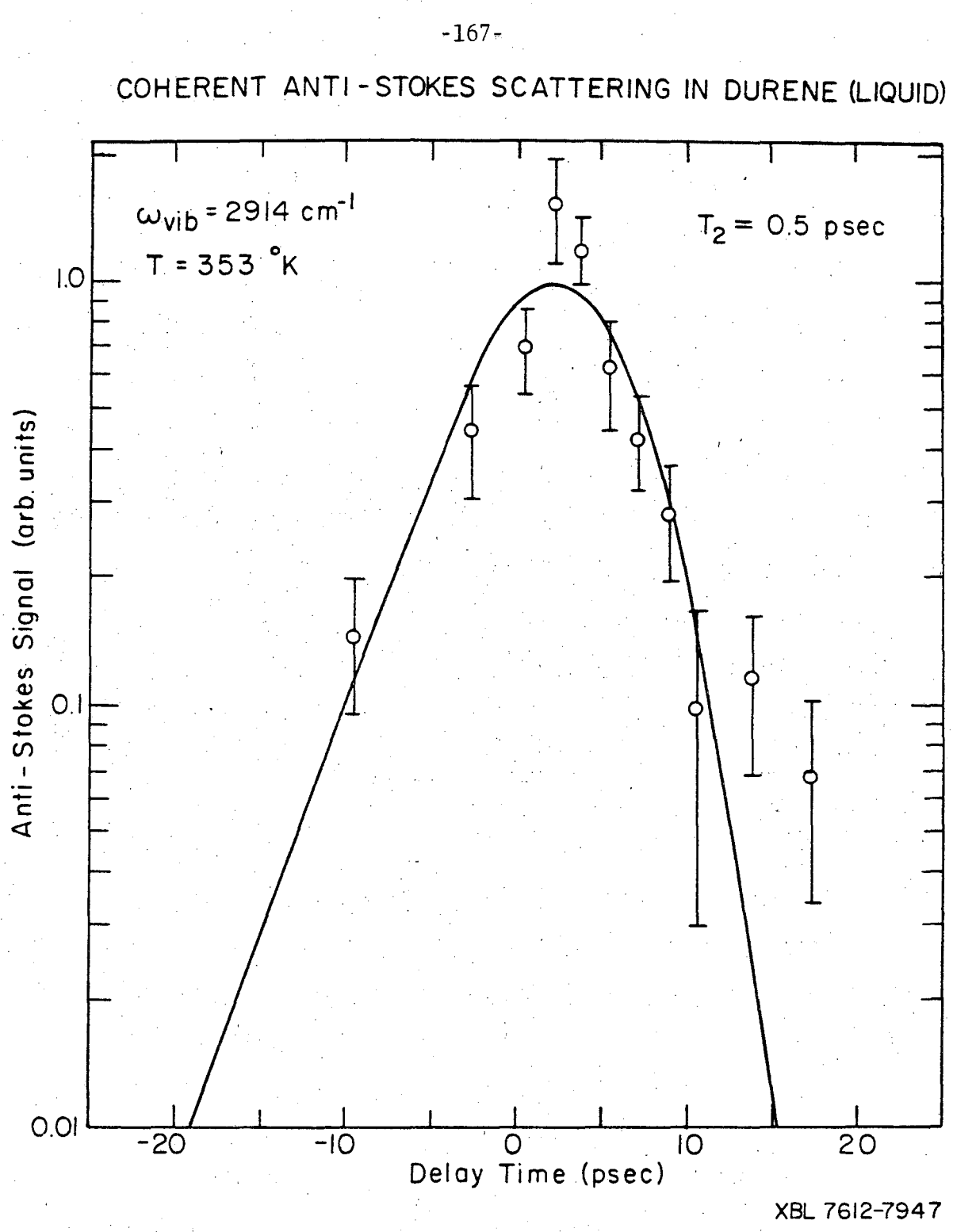
COHERENT ANTI-STOKES SCATTERING IN DURENE (LIQUID)
ωvib = 2914 cm-1
T = 353 °K
T2 = 0.5 psec
Anti-Stokes Signal (arb. units)
1.0
0.1
0.01
-20
-10
0
10
20
Delay Time (psec)
XBL 7612-7947

Figure 33

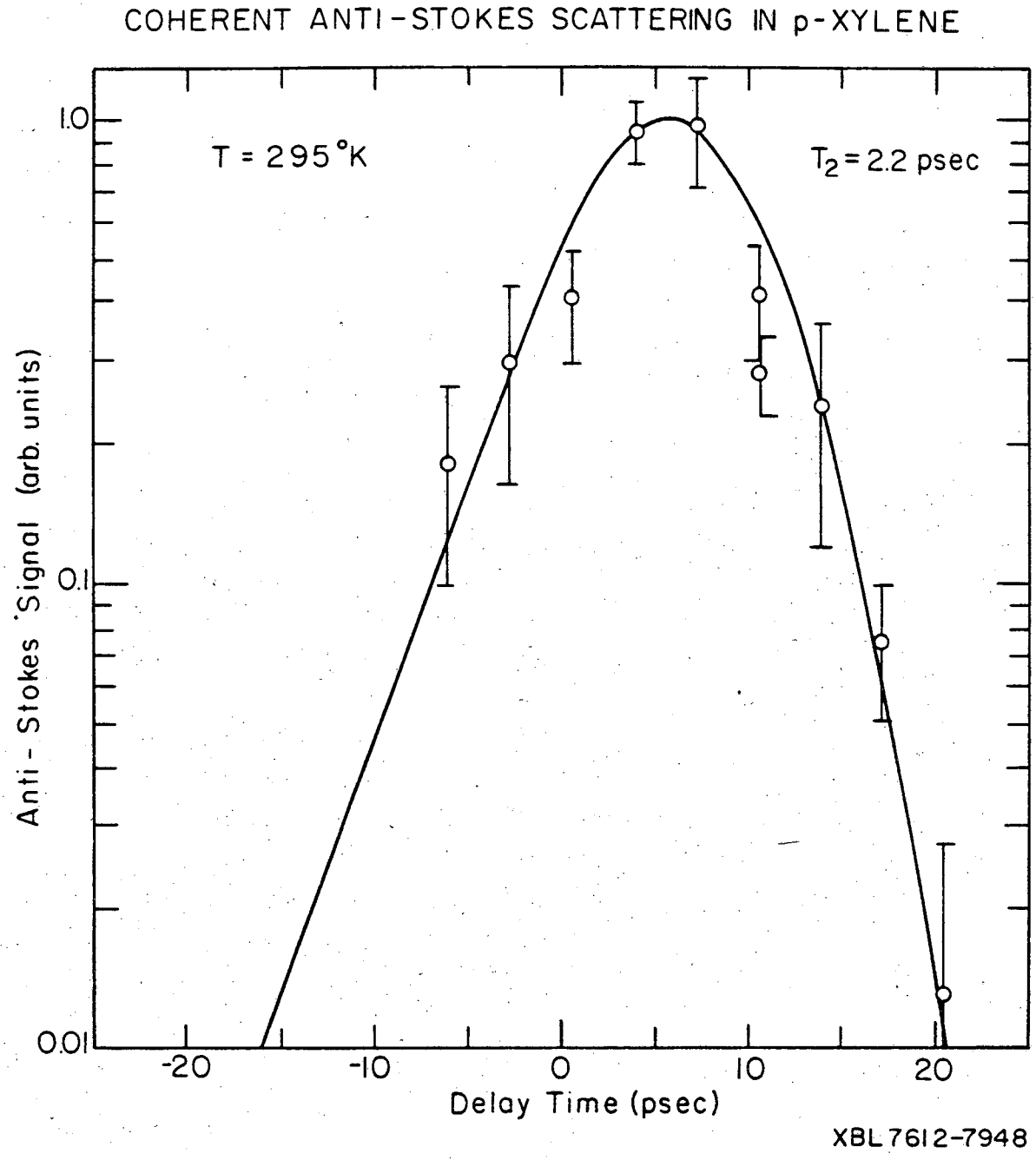
COHERENT ANTI-STOKES SCATTERING IN p-XYLENE
T = 295°K
T_2 = 2.2 psec
Anti-Stokes Signal (arb. units)
1.0
0.1
0.01
-20
-10
0
10
20
Delay Time (psec)
XBL 7612-7948

Figure 34

(e.g. phonons).[85-87] As discussed below in Section II, coupling with other intramolecular modes may also contribute. Both of these contributions would be expected to be strongly temperature dependent. In addition, one must also consider contributions due to the vibrational lifetime (T_1) and from inhomogeneous broadening. To help clarify the situation, the spontaneous Raman spectrum of durene in this frequency region was studied from room temperature to 10°K. The low- and high-temperature spectra are shown in Fig. 35. The band at 2912 cm^{-1} and the neighboring bands to lower frequency are assigned to the second harmonics and combination bands of C-H bending motions of the methyl groups ("scissors modes"). This assignment is made by analogy to the assignments of other methylated benzenes.[103-106] These harmonic bands appear very strongly in the Raman spectrum due to a Fermi resonance with the nearby C-H stretching modes, which are assigned as the five bands between 2920 cm^{-1} and 3050 cm^{-1}. Based on the result from the picosecond experiment, one expects a room temperature linewidth (full width at half maximum) given by

$$\overline{\delta\nu} = [\pi c T_2]^{-1} \qquad (73)$$

or 14 cm^{-1} for durene solid. The observed linewidth is about a factor of two larger than this value, although this is within the estimated experimental error. At low temperature the C-H stretching bands narrow considerably while the harmonic of the C-H bend at 2912 cm^{-1} stays quite broad. This is consistent with a dominant contribution to the linewidth from inhomogeneous broadening or from T_1. In a relatively large polyatomic molecule like durene the density of states near 2900 cm^{-1} due to overtones

Fig. 35. The picosecond dephasing time measurements in durene correspond to the intense band (at room temperature) at 2914 cm^{-1}. This band and others between 2920 cm^{-1} and 2850 cm^{-1} are attributed to harmonics of C-H bending vibrations due to the methyl protons ("scissors" modes). The five bands which become very sharp at low temperatures are assigned as C-H stretches. The line near 3030 cm^{-1} corresponds to the aromatic ring protons, and the other four lines the methyl group protons. The arrows in the lower panel indicate the magnitude of frequency shifts which occur when the sample is warmed to room temperature.

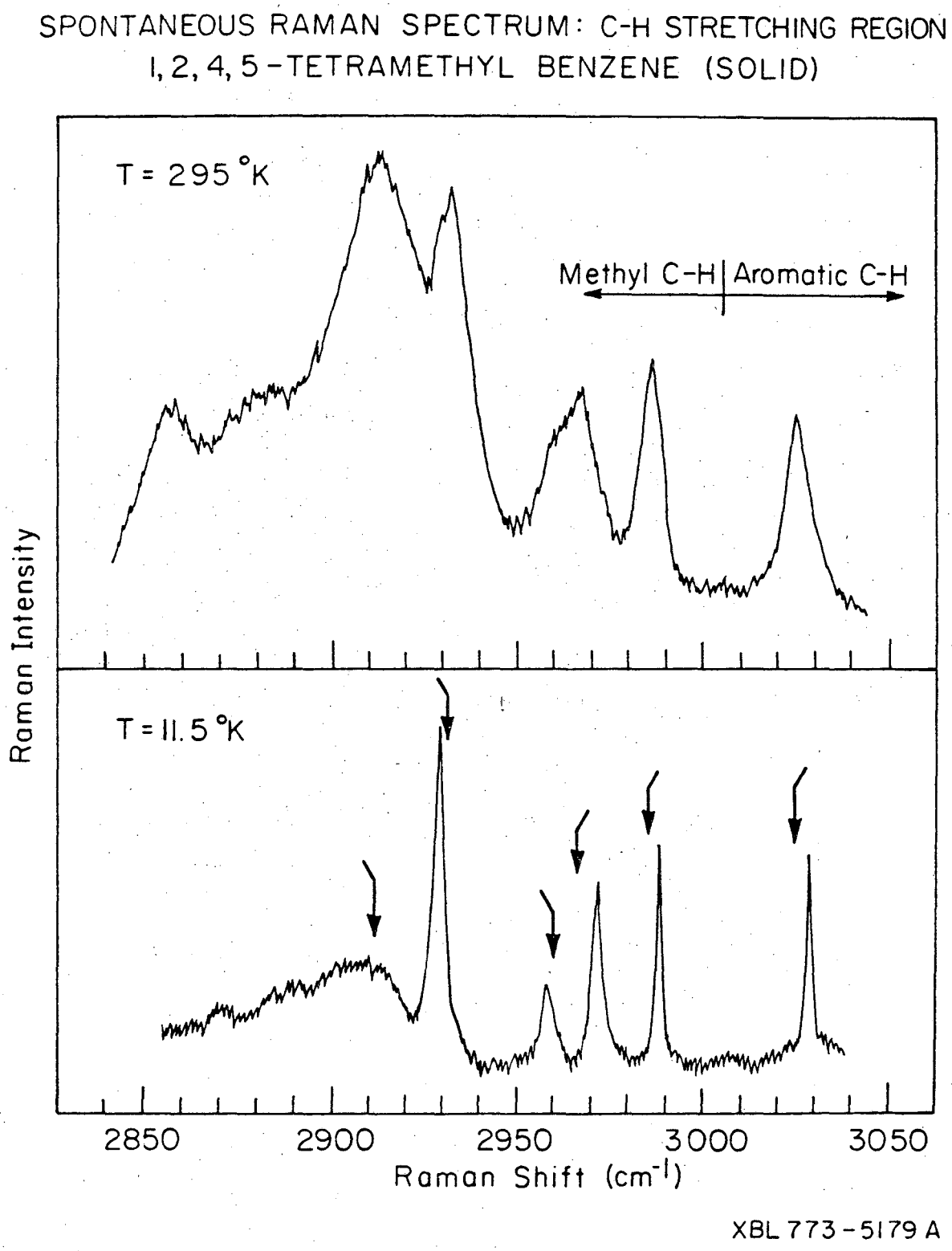
SPONTANEOUS RAMAN SPECTRUM: C-H STRETCHING REGION
1,2,4,5-TETRAMETHYL BENZENE (SOLID)
T = 295 °K
Methyl C-H
Aromatic C-H
T = 11.5 °K
Raman Intensity
2850
2900
2950
3000
3050
Raman Shift (cm⁻¹)
XBL 773-5179 A

Figure 35

and combinations of other intramolecular modes is expected to be quite large. Thus, T_1 for this mode probably results for the most part from redistribution of the vibrational energy among other intramolecular modes. Such a predominantly intramolecular pathway might well be almost independent of temperature over this range. The relatively fast T_1 for this vibration compared to the C-H stretches might result from relatively stronger coupling to nearby levels or from a peak in the density of these levels at this energy. A confirmation of this idea would require a direct measurement of T_1, since the T_2 measurement only represents a lower limit. In all measurements made so far in liquids, T_1 is considerably longer than T_2. Thus, the conjecture that T_1 and T_2 may be equal in this system would be a departure from this pattern.

For comparison, picosecond and spontaneous Raman measurements of p-xylene were also made. The picosecond results (see Fig. 34) for the band at 2915 cm^{-1} imply a dephasing time of 2.2 psec. However, the spontaneous Raman band has a width (FWHM) of 21 cm^{-1} which is four times too broad for this value of T_2 (see Fig. 36). This difference is not within the expected experimental error. The apparent discrepancy might possibly be resolved if these measurements had been made on an inhomogeneous line. The low-temperature (90°K) spontaneous Raman spectrum of p-xylene shown in Fig. 37 seems to lend support to this possibility since it clearly seems to indicate the presence of a number of spectral components near 2900 cm^{-1}. The relatively sharp lines at 2906 cm^{-1}, 2942 cm^{-1}, and 2970 cm^{-1} have been assigned to the C-H stretching modes of the methyl groups.[104] The other components in the area between 2850 cm^{-1} and 2930 cm^{-1} can be assigned as in durene to harmonics and combination bands of

Fig. 36. The spontaneous Raman lineshape function (triangles) and the linewidth expected from the picosecond results are compared. The solid lines represent Lorentzian lineshape functions. The factor of four discrepancy cannot be accounted for by experimental error and may be the result of an inhomogeneous line.

Fig. 37. The temperature dependent Raman spectrum of xylene shows a number of interesting effects, many of which are only partially understood at this time. The point to note is that the picosecond data at room temperature in the liquid phase correspond to the harmonics of the C-H bending modes on the methyl groups as in durene. At low temperatures, it appears as if there are several spectral components in the region below 2925 cm^{-1} which may not be completely averaged at room temperature, thus leading to an inhomogeneous line.

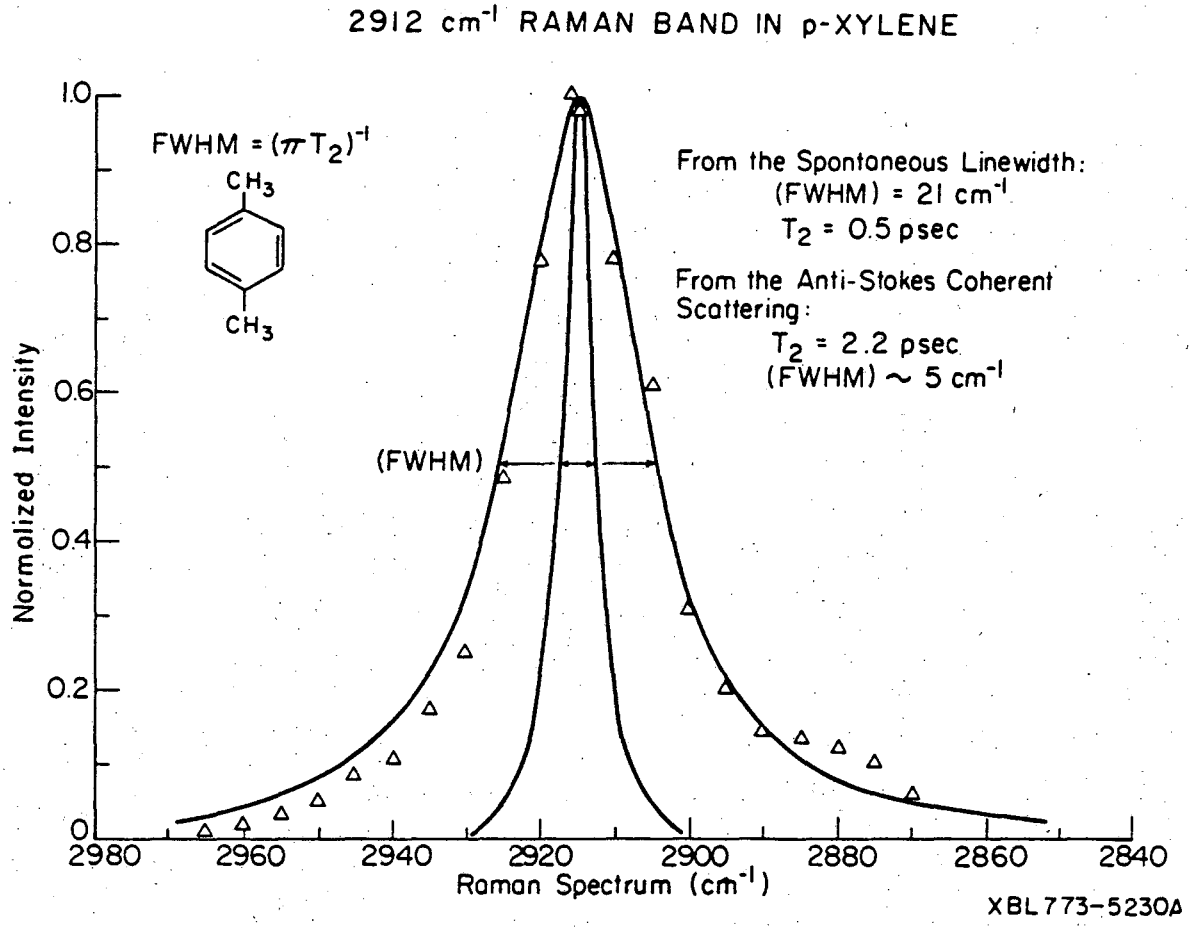
2912 cm⁻¹ RAMAN BAND IN p-XYLENE
FWHM = (πT2)⁻¹
CH3
CH3
From the Spontaneous Linewidth:
(FWHM) = 21 cm⁻¹
T2 = 0.5 psec
From the Anti-Stokes Coherent Scattering:
T2 = 2.2 psec
(FWHM) ~ 5 cm⁻¹
(FWHM)
Normalized Intensity
1.0
0.8
0.6
0.4
0.2
0
2980
2960
2940
2920
2900
2880
2860
2840
Raman Spectrum (cm⁻¹)
XBL773-5230A

Figure 36

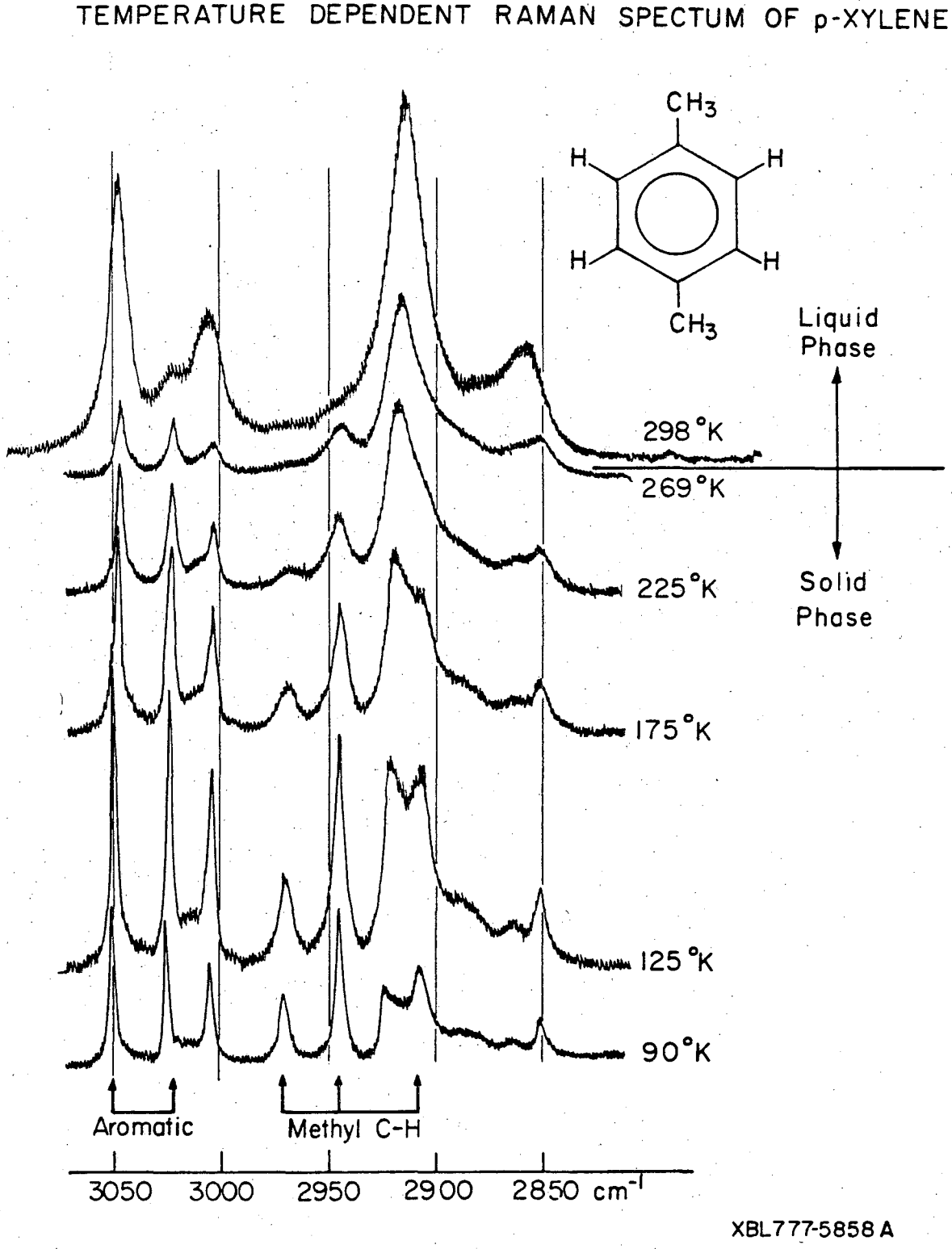
TEMPERATURE DEPENDENT RAMAN SPECTUM OF p-XYLENE
CH3
H
H
H
H
CH3
Liquid Phase
298 °K
269 °K
225 °K
Solid Phase
175 °K
125 °K
90 °K
Aromatic
Methyl C-H
3050
3000
2950
2900
2850 cm-1
XBL777-5858 A

Figure 37

the methyl C-H bending modes. As the temperature is increased, the C-H stretch bands tend to broaden and lose intensity. Finally, in the liquid phase, the C-H bend harmonics dominate the spectrum near 2900 cm^{-1}, and the picosecond data correspond to the dephasing of these harmonics. It is quite reasonable that the interactions which are responsible for the inhomogeneity which is apparently present in the solid, are not completely averaged by molecular motion even in the liquid phase.

As pointed out in the theoretical discussion however, the differential equations which describe the excitation process must be modified in the presence of inhomogeneous broadening. Thus, although the xylene data can be fit by a single isochromat with T_2 = 2.2 psec, this result does not necessarily reflect the true homogeneous relaxation time when a comparison with the observed spontaneous linewidth indicates the possibility of inhomogeneous broadening. Qualitatively, however, the equations of Laubereau[98] indicate that the build-up and decay of each isochromat is governed by an equation formally identical to that for the homogeneous case. Since the fitting process used to obtain the 2.2 psec value is sensitive to the time required for this build-up, one might expect this value to give some indication of the degree of inhomogeneity.

Preliminary attempts to calculate the expected anti-Stokes signal using a computer integration of the full inhomogeneous equations [Eq. (68)] have failed to completely resolve this question. The difficulty with these calculations lies in the large number of isochromats (and correspondingly large amounts of computer time) required to accurately represent the inhomogeneous distribution. However, the calculations seem to indicate that a homogeneous dephasing time which is <u>longer</u> than

2.2 psec might be required to account for the data. This comes about because the experimental geometry provided phase-matching conditions in this case for a range of frequencies including the inhomogeneous linewidth. The coherent scattering data presented here therefore monitors the complex sum of the vibrational amplitudes of all isochromats. Interference among these isochromats causes the build-up of this sum to be cut off somewhat earlier in time than the peak of the individual amplitudes. Thus, a longer T_2 is required to compensate. Even so, the calculations completed thus far with a limited number of isochromats have been unable to completely account for this data. If the homogeneous relaxation time turns out to be sufficiently long, the problem can be resolved experimentally through the use of highly selective wave vector matching geometry which would allow the decay of a single isochromat to be observed in the coherent probe scattering experiment.

The presence of inhomogeneous broadening is easily rationalized in a solid by the existence of crystal defects and static disorder, but is somewhat surprising in the liquid phase. It is interesting to note that Laubereau, et.al.[5] have observed inhomogeneous broadening in one of the vibrational bands of liquid methanol and have successfully measured the homogeneous decay time. In this case the spontaneous Raman linewidth is 26 cm^{-1} and the homogeneous dephasing time has a value of T_2 = 4.6 psec. They attribute the inhomogeneity to the persistence of different molecular environments for relatively long periods of time due to strong intermolecular hydrogen bonding. From the point of view of the results described here, it should be mentioned that their experiment was performed on the methanol band at 2942 cm^{-1} which has also been assigned to the harmonic

of the C-H bending mode of the methyl group.[107] Thus, the presence of inhomogeneous broadening in this class of methyl group vibrations might explain the methanol results, the p-xylene picosecond data discussed above, and the lack of a strong temperature dependence for the linewidth of the corresponding band (2912 cm^{-1}) of durene. However, these statements are of a speculative nature, since the presence of inhomogeneity in the xylene and durene case has not yet been proven unequivocally. Further study of these systems and similar ones will be necessary to directly measure the homogeneous relaxation times, and understand the detailed nature of the inhomogeneity as well as the source of the homogeneous decay.

D. Conclusion

The dephasing time of a methyl group C-H bending mode harmonic has been directly measured in a single crystal of 1,2,4,5-tetramethylbenzene (durene) using picosecond spectroscopy. This represents the first such measurement in an organic molecular crystal. These determinations were facilitated by fitting the experimental data to numerical solutions of the equations which describe the stimulated Raman excitation and probing process. Solutions of these equations were presented for both homogeneously and inhomogeneously broadened lines, and it was shown that the fitting process is capable of obtaining semi-quantitative values for T_2 when it is on the order of or even somewhat smaller than the picosecond pulse width.

Similar measurements on the same mode in liquid durene and liquid p-xylene were also made. Comparisons with the spontaneous Raman spectra

of these compounds and with previous picosecond results in methanol suggest that inhomogeneous broadening may be an important source of linewidth for this C-H bending harmonic in liquids. This is also consistent with the observed temperature dependence of the spontaneous Raman spectrum in solid durene and solid p-xylene. The presence of inhomogeneous broadening of this line could possibly be confirmed and the homogeneous T_2 more accurately measured by the use of selective wave vector matching conditions to observe the decay of a single isochromat. Further analysis of the vibrational spectrum may also help to determine the source of the inhomogeneity in this band, which at present is an open question. In this vein, the following section of this work will explore an example of the dynamical averaging of different vibrational states. This averaging process (similar to exchange averaging in magnetic resonance) is directly related to the persistence of inhomogeneous broadening or the averaging of this inhomogeneity in the presence of molecular motion.

Also left essentially untouched is the area of vibrational energy transfer dynamics in these systems. Although the comparison of the durene crystal and liquid results seem to indicate that the crystal periodicity is relatively unrelated to the dephasing of the particular vibrational mode investigated, very little else can be said. Because of the fairly selective nature of the excitation process, other vibrational modes of this molecule cannot easily be studied by this technique, and it is difficult to put together a complete picture of the dynamics. Perhaps experiments at low temperatures and with isotopically mixed crystal systems can shed some light on this problem.

III. Dephasing of Vibrational States by Energy Exchange

A. Introduction

While picosecond and spontaneous Raman lineshape measurements have greatly broadened the scope of experimental knowledge of vibrational relaxation, a thorough understanding must include the mechanisms and pathways which relate the relaxation times to the dynamics. With such an understanding, measurements of vibrational dephasing can help to characterize the associated interactions between the vibrating molecule and excitations of its surroundings. Recent strides toward this goal have been rapid. Picosecond experiments have demonstrated the importance of both energy relaxation (T_1 processes)[31a] and dephasing (T_2 processes)[44] in determining the Raman lineshape. They have separated the contributions due to inhomogeneous broadening from those which represent the "true" dynamics of dephasing, and they have successfully mapped out the important pathways for redistribution of vibrational energy in some cases.[5] On the theoretical side, several authors[85-87] have advanced models which relate the experiments to the interactions responsible for the dephasing and which are particularly appropriate for the diatomic or small molecule case. In the case of polyatomic molecules, however, it should be realized that the important relaxation and dephasing channels include ones associated with intramolecular interaction between different vibrational modes. In fact, in many cases this mechanism may dominate other dephasing processes, and an example of such a case will be presented.

Furthermore, in order to extract the dynamical information which

characterizes a given dephasing channel, such as scattering rates or lifetimes, it is necessary to consider the possible influence of phase memory. When phase memory is not important, it may be possible to directly interpret the (homogeneous) dephasing time as a scattering rate among a range of possible vibrational frequencies. However, if the excitation scatters back to its original frequency in a time which is too short to completely randomize its phase, the resulting narrowing effect must be taken into account to extract the true scattering rate.

In this section, it will be shown that when the effects of this "energy exchange" are incorporated into the vibrational correlation function it is possible in favorable cases to determine which dephasing channels are dominant and to extract the corresponding rates of energy exchange or scattering times. This approach quite easily takes into account the participation of intramolecular degrees of freedom in the dephasing process and is therefore applicable to polyatomic molecules.

In Part B, an outline of the exchange formalism is presented from the point of view of vibrational dephasing of polyatomic molecules, and the connection and similarity with previous formulations of the exchange mechanism are indicated. In Part C, these ideas are illustrated with experimental data on the C-H stretching modes of durene (1,2,4,5-tetramethylbenzene). It is found that quantitative application of the theory can result in a deeper understanding of the anharmonic interactions between the C-H stretches and various low frequency methyl group motions.

B. The exchange model: theoretical development

The approach to vibrational dephasing processes to be presented here is actually quite general. The key idea is the partitioning of the degrees of freedom of the molecule and surroundings (excluding vibrational mode A whose dephasing we are interested in) into two groups, the exchanging modes and the reservoir. The exchanging modes are those modes which interact strongly with mode A such that their excitation shifts the frequency of mode A. These need not be intramolecular vibrations, but might, for example, be lattice vibrations or acoustic waves depending on the system. The reservoir consists of all remaining degrees of freedom. When the exchanging modes (B modes) exchange thermal energy with the reservoir, their excitation and de-excitation causes a random modulation of the vibrational frequency of mode A. It is the rate of this modulation relative to its amplitude which determines the importance of phase memory in the scattering process. The effects of the modulation will be determined in the context of Markoffian coupling of the exchanging modes and the reservoir. In other words, it is assumed that the coherence time of the reservoir is short compared to the time required for any change in the state of the system (mode A and the exchanging modes).

The application of these ideas to vibrational dephasing is shown in Fig. 38 for the case where for simplicity only one exchanging mode is shown. Relaxation to lower states (the normal T_1 channels) is separated from scattering in this one channel denoted by the two vibrational states V and V'. The two vibrational frequencies associated with V and V' are coupled via exchange and are defined as ω_o and $\omega_o + \delta\omega$, respectively. It should be noted that $\delta\omega$ can be either positive or negative depending on

the nature of the coupling, and that the vibrational state V' associated with the frequency $\omega_o + \delta\omega$ is at an energy E_i above the state V. The scattering rates responsible for vibrational energy exchange are given as W_+ and W_-, and the lifetime in V' is given as $\tau = (W_-)^{-1}$. The effect of this scattering on the Raman spectrum is to generate a width of the scattered light. This comes about as follows: The laser light and Stokes radiation field couple with the ensemble of oscillators to result in the flow of energy from the laser field to the Stokes field. This process continues as long as the radiation fields and the oscillators retain the proper phase. A scattering process which changes the frequency of the oscillators interrupts the flow of energy and results in a finite width for the Stokes radiation. However, if the oscillator returns to the original frequency in a short time, it "remembers" its phase. This corresponds to a relatively longer correlation time and therefore reduced spectral broadening. In addition, the "mixing in" of the second frequency causes an apparent shift of the frequency of the scattered Stokes light. This broadening and associated frequency shift are the signature of the exchange mechanism.

These effects of phase memory can be quantified using two approaches suggested by magnetic resonance exchange theory. For example, the random frequency modulation model of Anderson[108] can be used to calculate the contribution of the exchange to the decay of the vibrational correlation function and thus its effect on the low power spontaneous Raman spectrum. Alternately, the exchange terms can be incorporated into the density matrix equations of motion for Raman excitation in a manner similar to the modified Bloch equation method of McConnell.[110] This approach would

be useful in including the effects of exchange in the coupled-wave description of stimulated Raman scattering discussed above. The approach taken here will make use of the formalism of reservoir theory[111,112] to calculate the effects of coupling between the reservoir and the exchanging modes. This approach has the advantage that the mechanism leading to the scattering rates W_+ and W_- are included in a flexible way, and the connection between the two methods just mentioned becomes somewhat clearer. Attention will be focused on the spontaneous Raman lineshape which can be determined from the vibrational correlation function using the formula:[70,71]

$$I(\omega) \sim \int_{-\infty}^{\infty} \exp(-i\omega t) \langle [\vec{\varepsilon}_s \cdot \overleftrightarrow{\alpha}(0) \cdot \vec{\varepsilon}_I][\vec{\varepsilon}_s \cdot \overleftrightarrow{\alpha}(t) \cdot \vec{\varepsilon}_I] \rangle_o \times \langle Q(0)\, Q(t) \rangle_v \, dt \tag{74}$$

where the polarizability autocorrelation function has been separated into orientational (o) and vibrational (v) contributions. $\alpha(t)$ is the Raman tensor for the transition of interest (mode A), $Q(t)$ is its normal coordinate, and ε_s and ε_I are the polarization vectors of the scattered and incident light.

Reservoir Approach

The Hamiltonian which will be used to describe the molecule and reservoir takes the form

$$\mathcal{H} = H_A + H_B + H_P + H_R + H_I = H_M + H_R + H_I \tag{75}$$

H_A and H_B are the zero order Hamiltonians for mode A and the exchanging modes, and H_P is the perturbation which couples mode A with the B modes

thus causing the dependence of the A frequency on the B quantum number. H_R and H_I represent the zero order reservoir Hamiltonian and the interaction between the reservoir and the B modes respectively. As in the theory of Anderson,[108] H_I is a "motional" Hamiltonian. Since $[H_P,H_I] \neq 0$, this term indirectly introduces a time dependence of the frequency of mode A via the perturbation H_P. This time dependence can be displayed by the use of the reduced density matrix, ρ^M, which has the equation of motion[111]

$$\dot{\rho}^M = (-i/\hbar)\ \mathrm{Tr}_R([\mathcal{H},\rho]) \tag{76}$$

where ρ is the density matrix for the molecule plus reservoir and Tr_R is a trace over reservoir coordinates, i.e. $\rho^M = \mathrm{Tr}_R(\rho)$. This tracing operation represents an average over the reservoir distribution which is not observed experimentally. The following form will be used for $\mathcal{H}$:

$$H_A = \hbar\Omega_A(a^\dagger a + \tfrac{1}{2}) \tag{77}$$

$$H_B = \sum_j \hbar\Omega_j(b_j^\dagger b_j + \tfrac{1}{2}) \tag{78}$$

$$H_P = V_{anh}(a^\dagger, a, b_j^\dagger, b_j) \tag{79}$$

$$H_R = \sum_k \hbar\omega_k(\beta_k^\dagger\beta_k + \tfrac{1}{2}) \tag{80}$$

$$H_I = \sum_{j,k} \hbar\, g_{jk}(b_j\beta_k^\dagger + \beta_k b_j^\dagger) \tag{81}$$

a, b_j, and β_k are annihilation operators for the A mode, B modes and reservoir modes respectively, corresponding to the frequencies Ω_A, Ω_j, and ω_k. V_{anh} is the anharmonic coupling between A and B modes. The

problem of finding the time dependence of ρ^M is simplified by two key assumptions. First, it is assumed that the reservoir is so large that the interaction has little effect on it, and that ρ^R is therefore constant in time and given by a thermal distribution. The second is the Markoff approximation. Under this approximation, correlation functions of the reservoir coordinates are assumed to behave as δ-functions compared to the time evolution of ρ^M, and we cannot hope to describe the effect of coherence in the molecule-reservoir interactions, even at short times.

Since the method of derivation of the equation of motion for the reduced density matrix, ρ^M, is described quite lucidly elsewhere,[111,112] the procedure is only outlined here. First, by eliminating the dependence in Eq. (76) of the full density matrix, ρ, a simplified equation of motion is obtained:

$$\dot{\rho}^M(t) = -1/\hbar^2 \int_0^t dt' \; Tr_R \left\{ V_I(t)\, V_I(t')\, \rho_I^M(t') \otimes \rho_I^R(0) - V_I(t)\, \rho_I^M(t') \otimes \rho_I^R(0)\, V_I(t') \right\} + \begin{matrix}\text{hermitian} \\ \text{adjoint}\end{matrix} \tag{82}$$

where

$$V_I(t) = \sum_{j,k} \hbar\, g_{jk} \left\{ b_j\, \beta_k^\dagger \exp[-i(\Omega_j - \omega_k)t] + \beta_k\, b_j^\dagger \exp[-i(\omega_k - \Omega_j)t] \right\} \tag{83}$$

is the interaction picture version of H_I, and ρ_I^M and ρ_I^R are also in the interaction picture. The Markoff approximation consists of noting that the integrand in Eq. (82) is negligible except for $t' \approx t$ and setting $\rho_I^M(t') = \rho_I^M(t)$. By introducing the density of reservoir modes $\mathcal{D}(\omega)$, the sum over reservoir modes is converted to an integral over ω.

Performing these integrations, and transforming back to the Schroedinger picture, one obtains the equation of motion:

$$\dot{\rho}^M = (-i/\hbar)[H_M,\rho^M] - \tfrac{1}{2}\sum_j \Big\{[b_j b_j^\dagger \rho^M - b_j^\dagger \rho^M b_j]\ \gamma_j \bar{n}(\Omega_j) - [b_j \rho^M b_j^\dagger - \rho^M b_j^\dagger b_j]\ \gamma_j\big(\bar{n}(\Omega_j)+1\big) + \text{h.a.}\Big\} = \mathcal{B}\rho^M \qquad (84)$$

where $\bar{n}(\Omega_j) = [\exp(\hbar\Omega_j/kT) - 1]^{-1}$ is the average number of reservoir excitations at $\omega = \Omega_j$, and $\gamma_j = 2\pi\hbar^2 |g_{jk}(\omega_k = \Omega_j)|^2\, \mathcal{D}(\Omega_j)$. $\mathcal{B}$ is the equivalent "superoperator."

It is illustrative to consider matrix elements of Eq. (84). It will be assumed, as in Fig. 38, that only one mode of frequency Ω_B is involved in the exchange and that the temperature is low enough that only the four states $|V_A,V_B\rangle = |00\rangle$, $|01\rangle$, $|10\rangle$, and $|11\rangle$ need be considered. One then finds that

$$\dot{\rho}^M_{00,10} = -i\,\omega_o\,\rho^M_{00,10} - W_+\,\rho^M_{00,10} + W_-\,\rho^M_{01,11} \qquad (85)$$

$$\dot{\rho}^M_{01,11} = -i(\omega_o + \delta\omega)\,\rho^M_{01,11} - W_-\,\rho^M_{01,11} + W_+\,\rho^M_{00,10} \qquad (86)$$

where $W_+ = \gamma_B \bar{n}(\Omega_B)$ and $W_- = \gamma_B\big(\bar{n}(\Omega_B)+1\big)$. The form of the exchange rates W_+ and W_- is traceable to the form chosen for H_I. By including appropriate interactions for double quantum transitions, etc., the results for W_+ and W_- would be affected accordingly. In this way, the appropriate "motional Hamiltonian" for a particular problem can in principle be incorporated into the formalism. The frequency terms including frequency shifts due to H_P are given by $\omega_o = \Omega_A + (V_{10,10} - V_{00,00})/\hbar$ and $\omega_o + \delta\omega =$

Fig. 38. Energy levels for vibrational exchange between two modes denoted by V and V'. A vibrational mode of frequency ω_o and vibrational quantum number n_v interacts with some low-frequency mode (quantum number n_t) such that excitation of the low-frequency mode shifts the frequency by $\delta\omega$. Excitation and de-excitation of the exchanging mode occur with the rates W_+ and W_-. The resulting modulation of the vibrational frequency is similar to the modulation of the larmor frequency in the two-site exchange problem in NMR. The exchange process manifests itself in the Raman spectrum through the vibrational correlation function.

VIBRATIONAL ENERGY EXCHANGE
BETWEEN COUPLED STATES

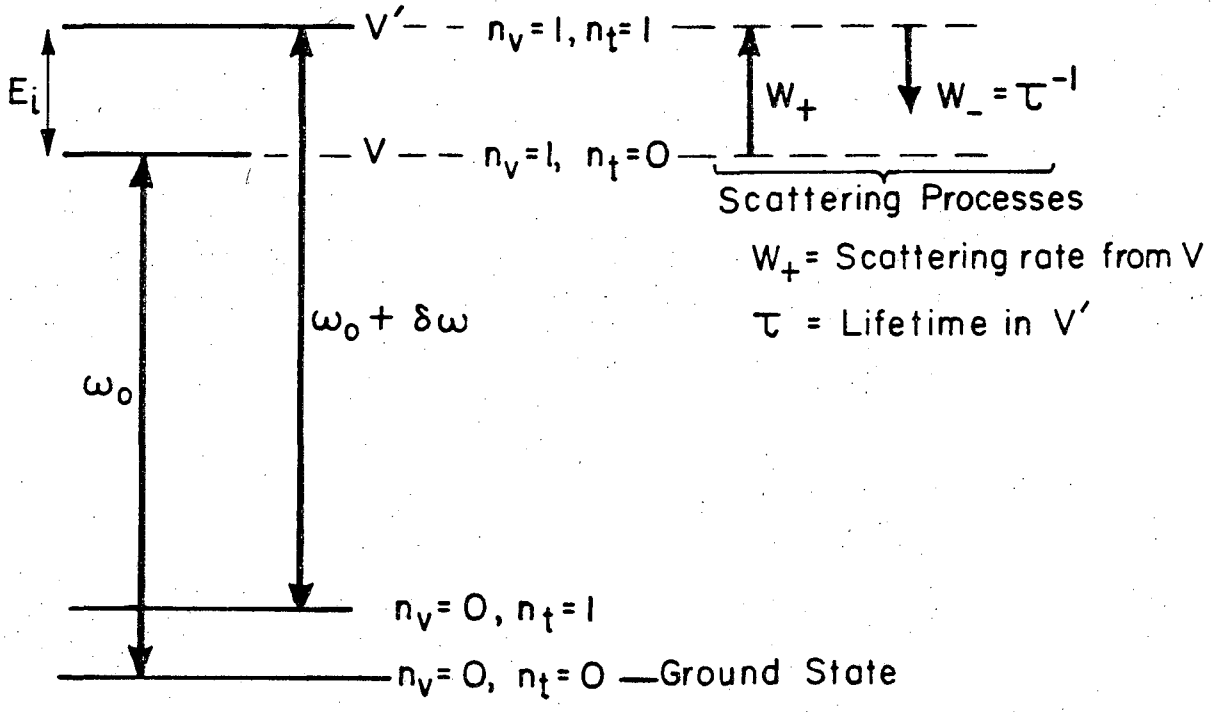

XBL774-5291

Figure 38

$\Omega_A + (V_{11,11} - V_{01,01})/\hbar$, where $V_{k\ell,nm} = \langle k\ell|V_{anh}|nm\rangle$. In this derivation the off-diagonal elements of H_p have been ignored, since within the framework of this formalism they would result in a partial redistribution of the vibrational excitation initially in mode A among the B modes. However, if the rate of mixing caused by these off-diagonal elements is fast compared to the transition rate γ_B, this redistribution will not occur, and the excitation remains in a single level (the one which correlates with the original level). In other words, the change in the vibrational frequency adiabatically follows the excitation of the B mode(s). In such a case it may be correct to include the off-diagonal part of H_p insofar as it makes a contribution to $\delta\omega$.[113] It should be noted that Eqs. (85) and (86) are essentially equivalent to the modified Bloch equation approach to the exchange problem.[110] Although the radiation field does not appear in this derivation, it could easily have been included in the original Hamiltonian, H_M.

To calculate the observed Raman spectrum, one needs the vibrational correlation function. This is equivalent in this formalism to the one-time average $\langle Q(t)\rangle$ where $Q = Q(a^\dagger + a)$ is the vibrational coordinate for mode A.[114] For the simple two-frequency exchange problem,

$$\langle Q(t)\rangle \sim \rho^M_{00,10}(t) + \rho^M_{01,11}(t) \tag{87}$$

Thus, we need only solve the coupled set of equations (85) and (86) which can be written in matrix form as:

$$\underset{\sim}{\dot{P}}^M_{01}(t) \equiv \begin{bmatrix} \dot{\rho}^M_{00,10}(t) \\ \\ \dot{\rho}^M_{01,11}(t) \end{bmatrix} = \begin{bmatrix} -i\omega_o - W_+ & W_- \\ \\ W_+ & -i(\omega_o + \delta\omega) - W_- \end{bmatrix} \begin{bmatrix} \rho^M_{00,10}(t) \\ \\ \rho^M_{01,11}(t) \end{bmatrix}$$

$$\equiv (i\underset{\approx}{\omega}_V + \underset{\approx}{\pi})\,\underset{\sim}{P}^M_{01}(t) \tag{88}$$

where $\underset{\approx}{\omega}_V$ is the diagonal matrix containing the vibrational frequencies and $\underset{\approx}{\pi}$ contains the transition rates among these frequencies. Therefore,

$$\frac{\langle Q(t)\rangle}{\langle Q(0)\rangle} = [1\ 1]\cdot\begin{bmatrix}\rho^M_{00,10}(t)\\ \rho^M_{01,11}(t)\end{bmatrix} = \underset{\sim}{1}\cdot\exp[t(i\underset{\approx}{\omega}_V+\underset{\approx}{\pi})]\cdot\underset{\sim}{W} \qquad (89)$$

where $\underset{\sim}{W} = \underset{\sim}{P}^M_{01}(0)$ is the initial population distribution. Eq. (89) is the matrix form of the expectation value of Q obtained from a direct formal solution of Eq. (84), namely:

$$\langle Q(t)\rangle = \mathrm{Tr}_M[Q\ \exp(t\mathcal{B})\ \rho^M(0)] \qquad (90)$$

The result is extendable to more complicated situations than the two-frequency example presented here by incorporating the appropriate interactions, frequency shifts, and exchange rates. Equation (89) is identical to Anderson's result [Eq. (49), ref. 108] and completes the connection between his approach, the reservoir approach and the modified Bloch equations.

Spectral Lineshape Functions

Aside from other contributions to the correlation function, the spectral lineshape is given by[115]

$$I(\omega) \sim \int_{-\infty}^{\infty}\exp(-i\omega t)\,\{\underset{\sim}{1}\cdot\exp[t(i\underset{\approx}{\omega}_V+\underset{\approx}{\pi})]\cdot\underset{\sim}{W}\}\,dt = \mathrm{Re}\,\{\underset{\sim}{1}\cdot\underset{\approx}{A}^{-1}\cdot\underset{\sim}{W}\} \qquad (91)$$

where $\underset{\approx}{A} = i(\underset{\approx}{\omega}_V - \omega\underset{\approx}{I}) + \underset{\approx}{\pi}$. For the two-frequency problem, the following explicit form is obtained:

$$I(\omega) = \frac{W_+(\delta\omega)^2 / (1 + W_+/W_-)}{[\omega'^2 - (\delta\omega/2)^2]^2 + [W_-(\omega' + \delta\omega/2) + W_+(\omega' - \delta\omega/2)]^2} \quad (92)$$

where $\omega' = \omega - \omega_o - \delta\omega/2$. The behavior of $I(\omega)$ as a function of temperature is shown in Fig. 39. For the purpose of this illustration, parameters were chosen which led to the observation of two well-defined peaks in the low-temperature limit. However, it is quite possible and often observed that the smaller peak is essentially invisible or appears as a shoulder or extended wing of the larger peak. Thus, the two-peak structure may not always be observed experimentally. It should also be noted that spectral narrowing is predicted at high temperatures. However, the simple two-frequency model would not be applicable in this limit, since other exchanging modes of higher frequency and harmonics of the low-frequency modes would introduce additional frequency shifts into the problem. Although the increased complexity of this situation could be incorporated into the theory, the comparison with experimentally observed lineshapes would be difficult owing to the large number of unknown parameters (exchange rates, etc.). The important point to note, though, is that these effects would probably obscure the narrowing expected when the original channel is in fast exchange.

For purposes of comparison between the theory and experimental lineshapes, sources of broadening other than the exchange process under consideration must be included in the lineshape function. One way to do this is to multiply the correlation function by $\exp(-t/T_2')$ before Fourier transformation in Eq. (91). When this factor is included, $I(\omega)$ becomes

Fig. 39. This figure shows an example of the temperature dependence of the exchange lineshape [Eq. (92)] for the parameters shown in the figure. The five curves correspond to the following temperatures: Curve #1 = 150°K; Curve #2 = 250°K; Curve #3 = 500°K; Curve #4 = 800°K; and Curve #5 = 1500°K. For this calculation the exchange rates were given by $W_+ = \gamma\left(\bar{n}(\Omega_B)\right)$ and $W_- = \gamma\left(\bar{n}(\Omega_B) + 1\right)$ where $\Omega_B = 150\ cm^{-1}$.

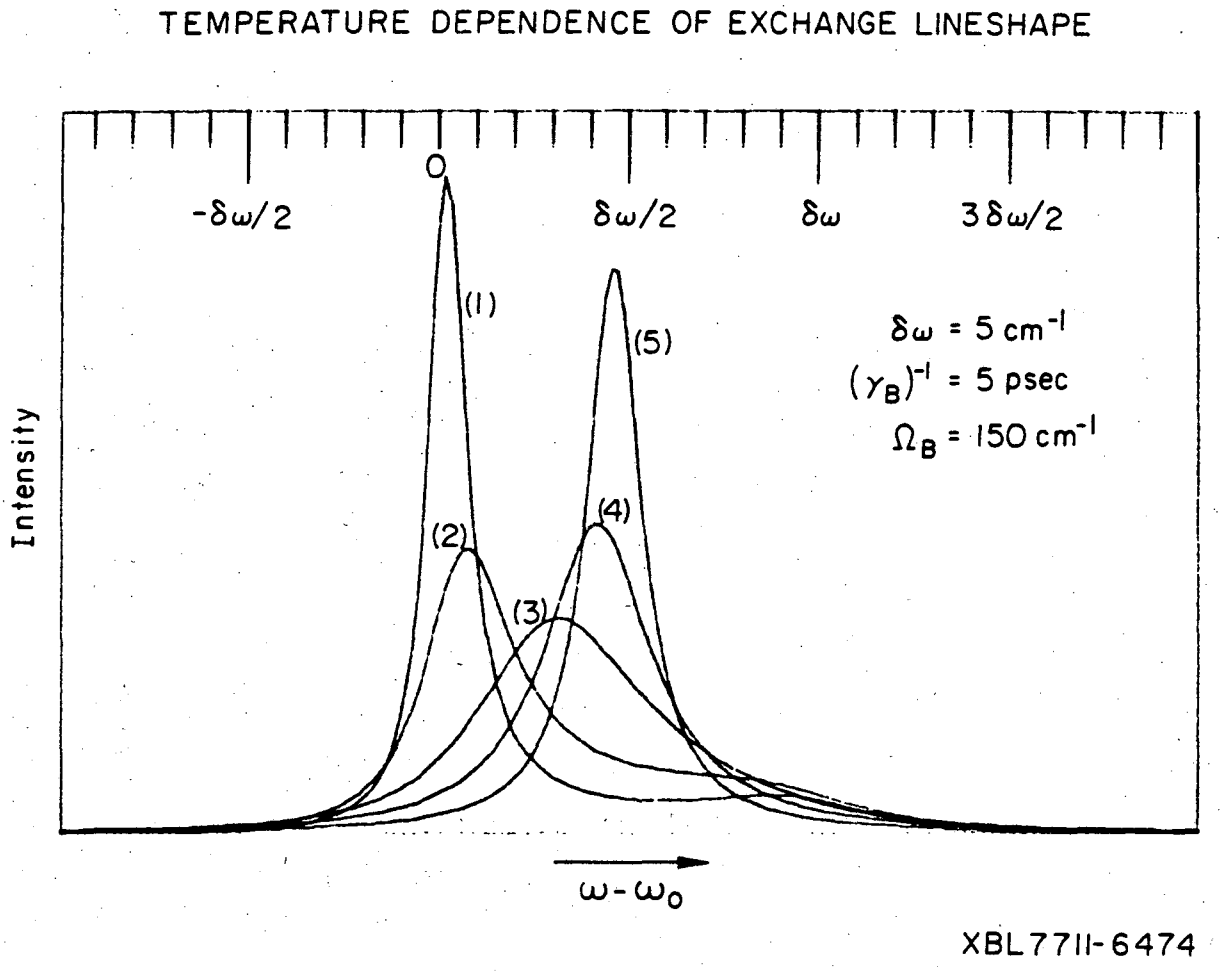
TEMPERATURE DEPENDENCE OF EXCHANGE LINESHAPE
0
-δω/2
δω/2
δω
3δω/2
(1)
(2)
(3)
(4)
(5)
δω = 5 cm⁻¹
(γB)⁻¹ = 5 psec
ΩB = 150 cm⁻¹
Intensity
ω - ω0
XBL7711-6474

Figure 39

$$I(\omega) = \frac{\left\{W_+W_-(\delta\omega)^2 + T_2'^{-1}\left[(W_+ + W_-)^3 + W_-(\delta\omega/2 - \omega')^2 + W_+(\delta\omega/2 + \omega')^2\right] + 2T_2'^{-2}(W_+ + W_-)^2 + T_2'^{-3}(W_+ + W_-)\right\} / (W_+ + W_-)}{\left\{\left[(\delta\omega/2)^2 - \omega'^2 + T_2'^{-2} + T_2'^{-1}(W_+ + W_-)\right]^2 + \left[W_-(\delta\omega/2 + \omega') - W_+(\delta\omega/2 - \omega') + 2\omega'/T_2'\right]^2\right\}} \quad (93)$$

This reduces to a Lorentz line of width $2/T_2'$ when W_+ and $W_- \to 0$ and to Eq. (92) when $T_2' \to \infty$. The use of this lineshape function in fitting experimental spectra is discussed below.

Since in the low temperature regime we have $W_+/W_- < 1$, $\delta\omega/W_+ < 1$, and $\delta\omega/W_- \lesssim 1$, one expects a large peak in $I(\omega)$ near ω_o and a small one near $\omega_o + \delta\omega$ whose center frequencies are shifted by an amount much less than $\delta\omega$. Therefore it should be possible to obtain Lorentzian approximation to $I(\omega)$ near $\omega = \omega_o$. This result is obtained by setting $\omega' - \delta\omega/2 \approx -\delta\omega$ in Eq. (92):

$$I(\omega) \approx \frac{W_+\tau^2(\delta\omega)^2 / [D(1 + W_+\tau)]}{(\omega' + \delta\omega/2 - W_+\tau\delta\omega/D)^2 + W_+^2[(\delta\omega)^2\tau^2]^2 / D^2} \quad (94)$$

where $D = 1 + (\delta\omega)^2\tau^2$ and $\tau = (W_-)^{-1}$ is approximately constant over the temperature range where this equation is valid. Thus, one expects to observe an effective Raman frequency

$$\omega^{eff} = \omega_o + W_+\delta\omega\tau / \left(1 + (\delta\omega)^2\tau^2\right) \quad (95)$$

and an effective relaxation time

$$\left(T_2^{eff}\right)^{-1} = W_+(\delta\omega)^2\tau^2 / \left(1 + (\delta\omega)^2\tau^2\right) + (T_2')^{-1} \quad (96)$$

where other relaxation processes are represented by T_2'. These approximate equations are particularly useful in visualizing the effects of phase memory.[116] In particular, when $\delta\omega\tau << 1$ the vibration retains all memory of its phase prior to scattering, and both the frequency shift and broadening effects vanish. It should be pointed out that whenever $\delta\omega\tau \lesssim 1$ one observes less contribution to the linewidth than might be expected on the basis of the scattering rate W_+, since $(T_2^{eff})^{-1} - (T_2')^{-1} < W_+$. In this sense the line is "exchange narrowed." On the other hand, when $\delta\omega\tau >> 1$ scattering results in complete loss of phase memory. In this case, the frequency shift vanishes, and the contribution to the dephasing time is simply W_+. Thus, it is the temperature dependent linewidth and frequency shift which is present when partial phase memory is retained (the intermediate exchange regime) that provides experimental evidence for vibrational exchange.

C. Comparison with experiments

It is our belief that these ideas are quite widely applicable and can make important contributions to the understanding of vibrational dephasing. In many cases it should be possible to measure the vibrational spectrum of a molecule over a temperature range which includes a region where $\delta\omega/W_+$ and $\delta\omega/W_-$ are of the order of unity. When this "intermediate exchange" region is accessible, it is possible to extract fundamental dynamical information such as exchange rates and the form of the interaction responsible for the dephasing. The Raman spectrum of durene in the C-H stretching region provides an excellent example of such an application.

This example possesses the advantage that individual low frequency methyl group motions appear to dominate the exchange process. The presence of single dephasing channels for each C-H stretching mode is dictated by the nature of the interaction term in the Hamiltonian responsible for the coupling to the exchanging mode. An analysis of this spectrum should therefore be helpful in investigating this coupling.

The Raman spectrum of durene between 2850 cm^{-1} and 3050 cm^{-1} is shown in Fig. 35 for the low temperature limit and at room temperature. The five bands above 2920 cm^{-1} display a marked broadening and shift of apparent vibrational frequency as the temperature is increased. For example, the temperature dependence of the observed linewidth and effective vibrational frequency is shown in Figs. 40 and 41 for the Raman band at 2929 cm^{-1}. As is indicated, these data decompose into an approximately temperature independent contribution and a contribution which varies exponentially with 1/T. This is exactly the dependence predicted by Eqs. (95) and (96) when $W_- = \tau^{-1}$ is roughly constant and $W_+ = \bar{n}(\Omega_B)/\tau \approx \tau^{-1} \exp(-E_i/kT)$ where the observed activation energy is expected to be approximately equal to Ω_B, the frequency of the dephasing (exchanging) mode. The interesting feature of these data is that $E_i = 220$ cm^{-1} is very close to the observed frequency for the torsional motion of the methyl groups at 190 cm^{-1}.[117] Thus, it appears likely that the torsion acts as exchanging mode for this C-H stretching mode. This temperature dependence has been further analyzed in terms of the more accurate line-shape function presented above. With some simplifying assumptions, a least-squares fitting procedure can be used to determine the unknown

Fig. 40. The temperature dependence of the Raman linewidth of the C-H stretching mode at 2929 cm^{-1} contains an approximately constant contribution and a contribution above ~30°K which is temperature dependent and is attributed to the exchange process. As shown in (b), this contribution displays an effective activation energy near the methyl group torsional frequency.

Fig. 41. The temperature dependence of the effective Raman frequency also displays an exponential dependence with an activation energy equal to that corresponding to the linewidth. These observations provide the clue that the torsional motion is acting as exchanging mode for this C-H stretching vibration. These data can be analyzed using Eqs. (95) and (96) to give approximate values of $\delta\omega$ and τ. A more accurate analysis but one which is slightly more complicated involves fitting the lineshape data to the theoretical expression, Eq. (93).

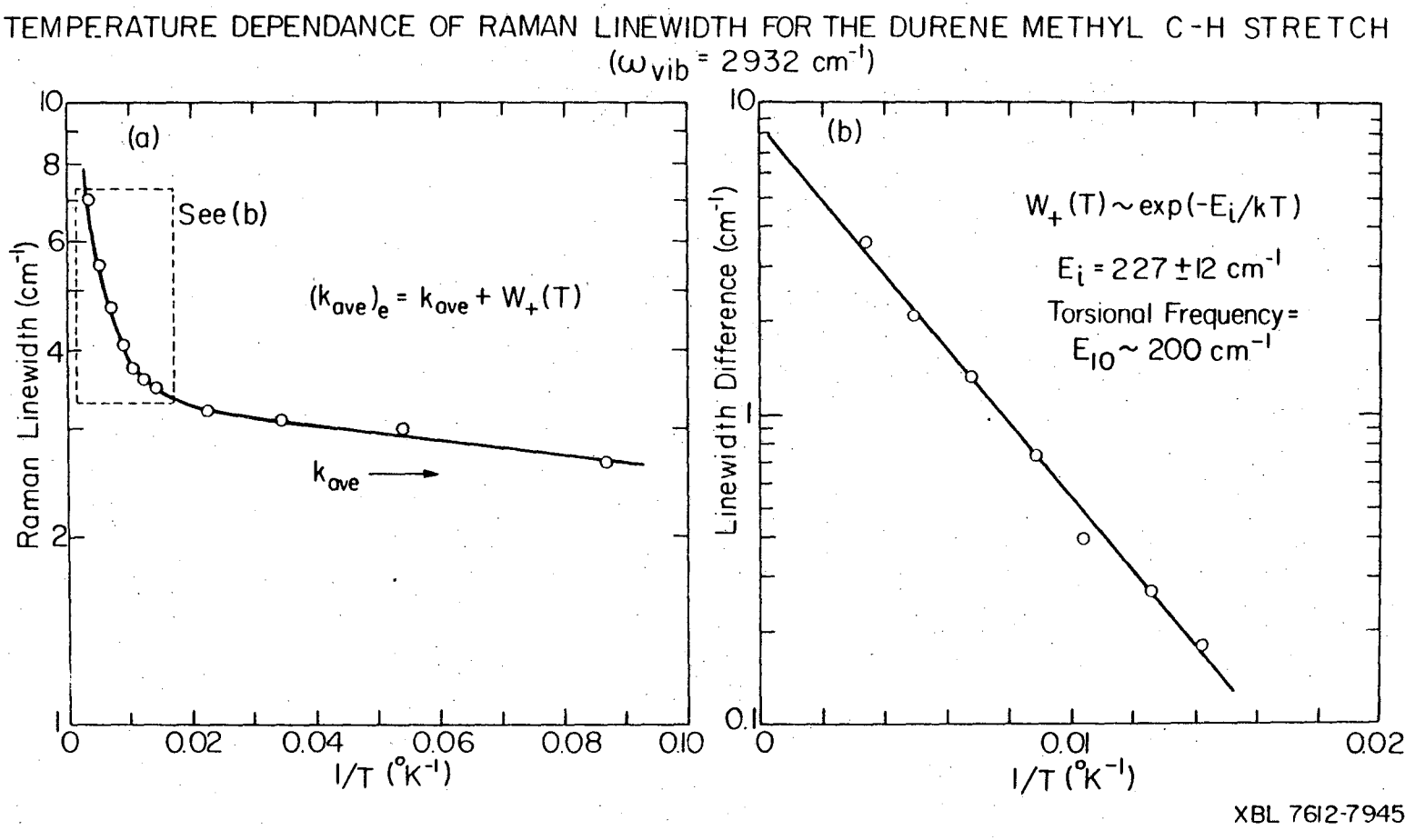
TEMPERATURE DEPENDANCE OF RAMAN LINEWIDTH FOR THE DURENE METHYL C-H STRETCH
(ω_{vib} = 2932 cm^{-1})
(a)
See (b)
$(k_{ave})_e = k_{ave} + W_+(T)$
k_{ave}
Raman Linewidth (cm^{-1})
1/T (°K^{-1})
(b)
$W_+(T) \sim \exp(-E_i/kT)$
$E_i = 227 \pm 12$ cm^{-1}
Torsional Frequency =
$E_{10} \sim 200$ cm^{-1}
Linewidth Difference (cm^{-1})
1/T (°K^{-1})
XBL 7612-7945

Figure 40

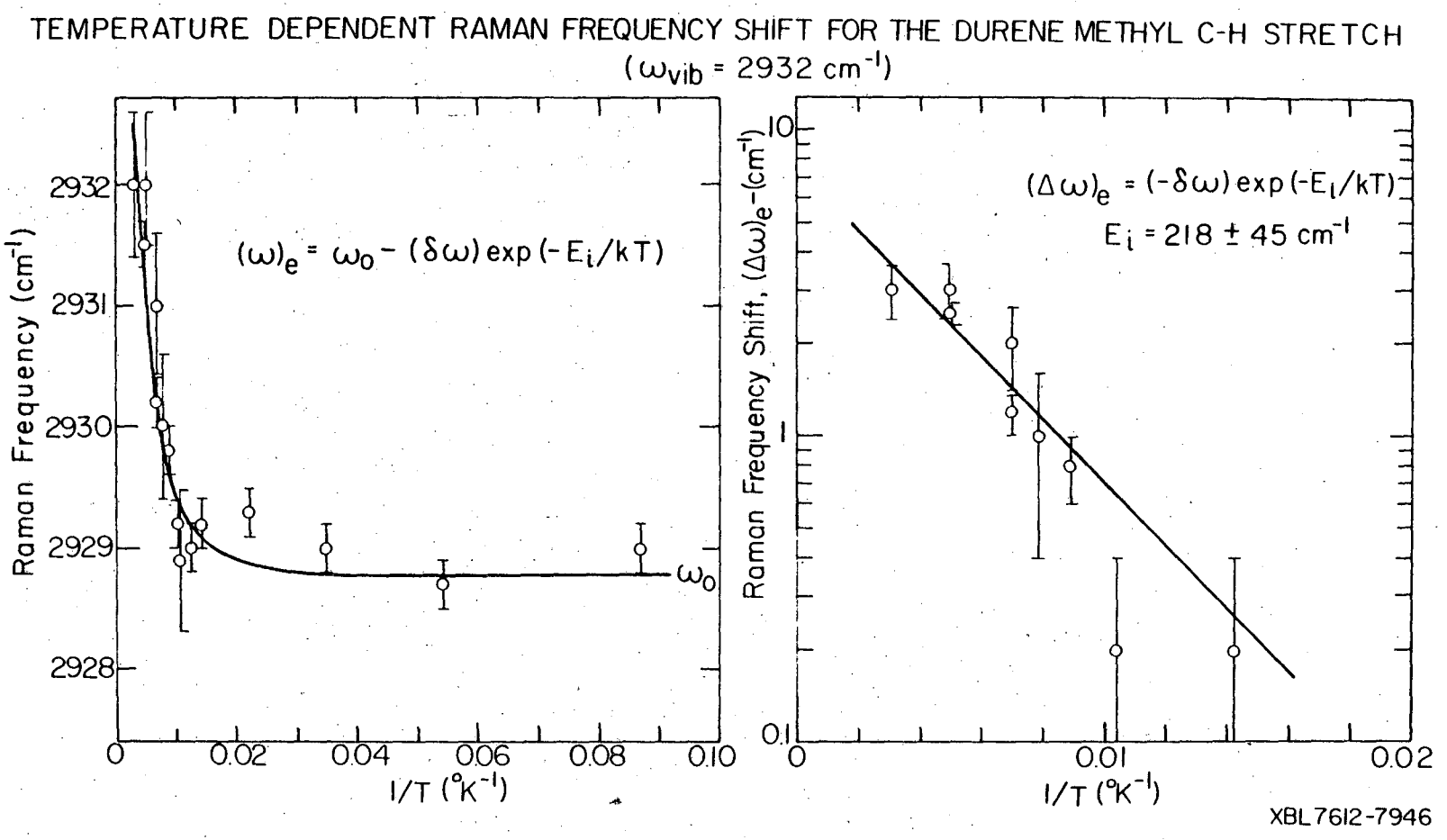
TEMPERATURE DEPENDENT RAMAN FREQUENCY SHIFT FOR THE DURENE METHYL C-H STRETCH
(ω_{vib} = 2932 cm^{-1})
$(\omega)_e = \omega_0 - (\delta\omega)\exp(-E_i/kT)$
Raman Frequency (cm^{-1})
2932
2931
2930
2929
2928
ω_0
0
0.02
0.04
0.06
0.08
0.10
1/T (°K^{-1})
$(\Delta\omega)_e = (-\delta\omega)\exp(-E_i/kT)$
$E_i = 218 \pm 45$ cm^{-1}
Raman Frequency Shift, $(\Delta\omega)_e$-(cm^{-1})
10
1
0.1
0
0.01
0.02
1/T (°K^{-1})
XBL7612-7946

Figure 41

parameters in Eq. (93) from the experimental lineshape data. It may then be possible to identify more unequivocally the modes which are important in the dephasing process.

In order to fit Eq. (93) to the experimental lineshape data, it was assumed that the exchange rates in the temperature range studied are given by $W_- = \tau^{-1}$ and $W_+ = \tau^{-1} \exp(-E_i/kT)$, where and E_i are the excited lifetime of the exchanging mode and the effective activation energy, respectively. The resulting expression for the lineshape (obtained from Eq. (93) with these substitutions) contains five parameters; τ, $\delta\omega$, and E_i describe the exchange process, and T_2' and ω_o give the low-temperature linewidth and frequency. These parameters are adjusted for the best fit to approximately 125 data points which represent the observed lineshape at ten different temperatures. This procedure was carried out using a standard general least-squares computer fitting program similar to those used in crystal structure determinations. The resulting value of E_i for the 2929 cm^{-1} mode is 194 ± 10 cm^{-1} which is almost exactly equal to the observed torsional frequency. With this encouragement, data from the remaining four lines were also fit using this procedure. The resulting values of the fitted parameters are shown in the inset of Fig. 42. Typical experimental lineshape data and the corresponding fitted function are shown in Fig. 43. The standard deviation of the observed data from the calculated lineshape function ranged from ~2% to ~7%.

The quantities $\delta\omega$ and τ represent the effects of the parts of the Hamiltonian which embody the interaction between the observed vibrational mode and the exchanging mode and the exchanging mode and the reservoir modes respectively (i.e. H_p and H_I). In particular, the quantity τ is

Fig. 42. The exchange rate W_+ is shown for the five durene lines indicated in the inset. The assumption is made that the rate $W_- = \tau^{-1}$ is constant over this temperature range (see Fig. 44). The effects of the exchange are observed for temperatures above about 100°K as the intermediate exchange region is beginning to be approached. The inset shows possible assignments for the C-H stretching modes, the dephasing (exchanging) modes which are thought to be important in the exchange process, and the values of the parameters determined by the fitting process. These include the effective activation energy, E_i, the frequency shift due to the perturbation H_p, $\delta\omega$, and the lifetime in the upper state, τ.

VIBRATIONAL DEPHASING RATES FOR THE RAMAN ACTIVE C-H STRETCHES IN 1,2,4,5 TETRAMETHYLBENZENE (DURENE)

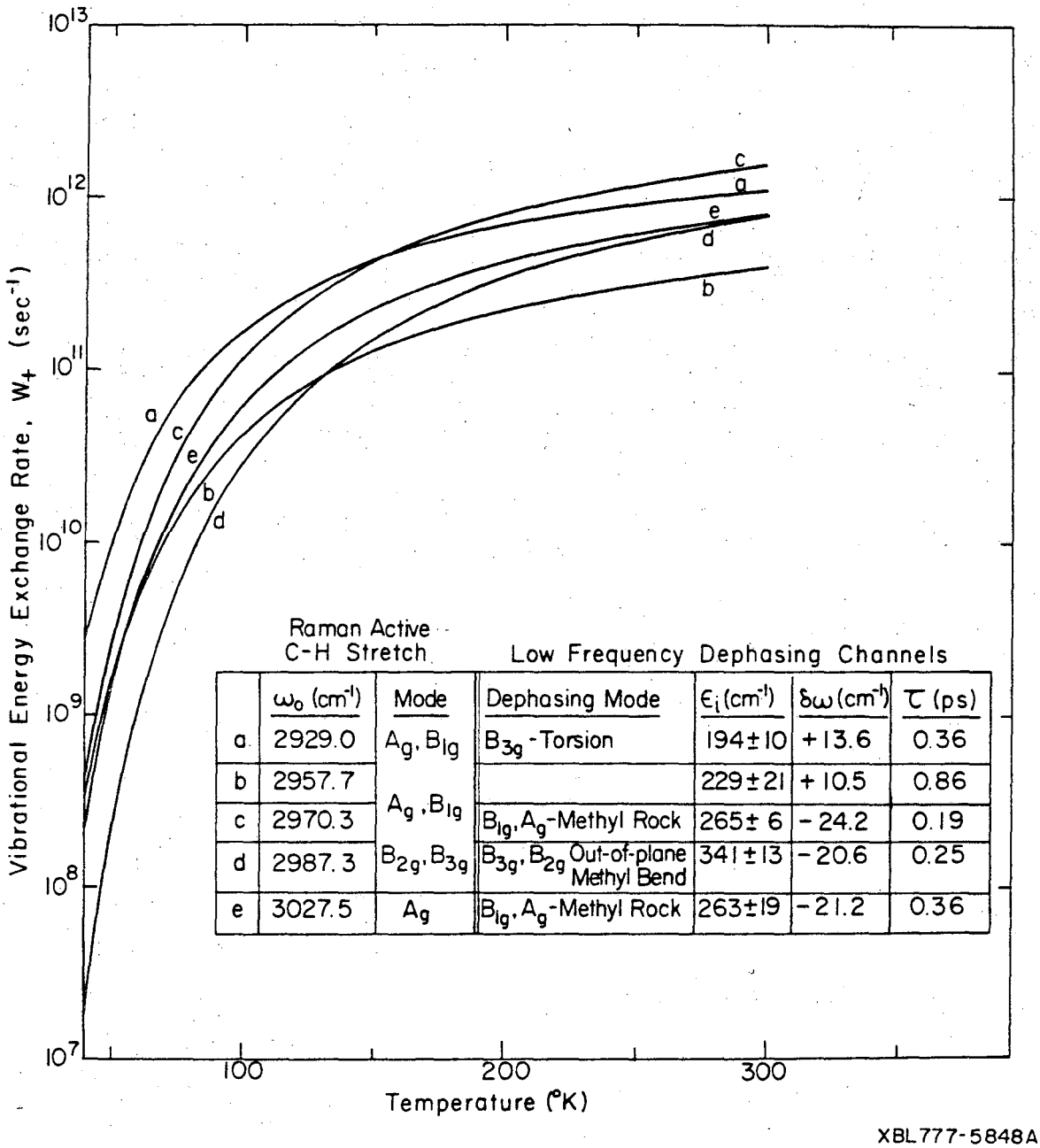

	Raman Active C-H Stretch		Low Frequency Dephasing Channels			
	ω_0 (cm^{-1})	Mode	Dephasing Mode	ϵ_i (cm^{-1})	$\delta\omega$ (cm^{-1})	τ (ps)
a	2929.0	A_g, B_{1g}	B_{3g} - Torsion	194±10	+13.6	0.36
b	2957.7	A_g, B_{1g}		229±21	+10.5	0.86
c	2970.3		B_{1g}, A_g - Methyl Rock	265± 6	-24.2	0.19
d	2987.3	B_{2g}, B_{3g}	B_{3g}, B_{2g} Out-of-plane Methyl Bend	341±13	-20.6	0.25
e	3027.5	A_g	B_{1g}, A_g - Methyl Rock	263±19	-21.2	0.36

XBL777-5848A

Figure 42

Fig. 43. Typical fits to experimental lineshapes using the lineshape function given in Eq. (93). In (a) the approximate function [Eq. (94)] is also shown (Curve #2) for comparison. For the lower temperature curves in (b) and (c), the approximate curve would be essentially coincident with the more exact function. The values of the various parameters mentioned in the text which are determined by the fitting process are shown in the figures. The experimental data is that for the aromatic C-H stretch line at 3027 cm^{-1} in the durene spectrum.

COMPARISON OF CALCULATED EXCHANGE LINESHAPE AND OBSERVED LINESHAPE
DURENE 3027 cm^{-1} VIBRATION

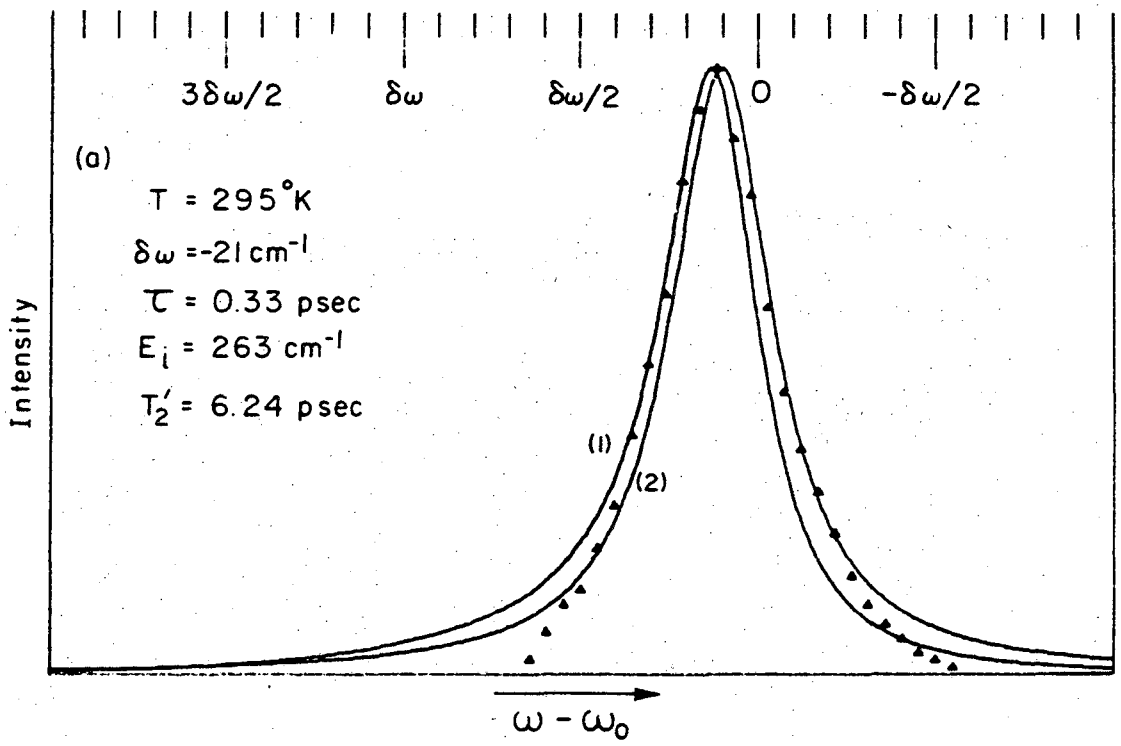

Figure 43a

COMPARISON OF CALCULATED EXCHANGE LINESHAPE AND OBSERVED LINESHAPE
DURENE 3027 cm^{-1} VIBRATION

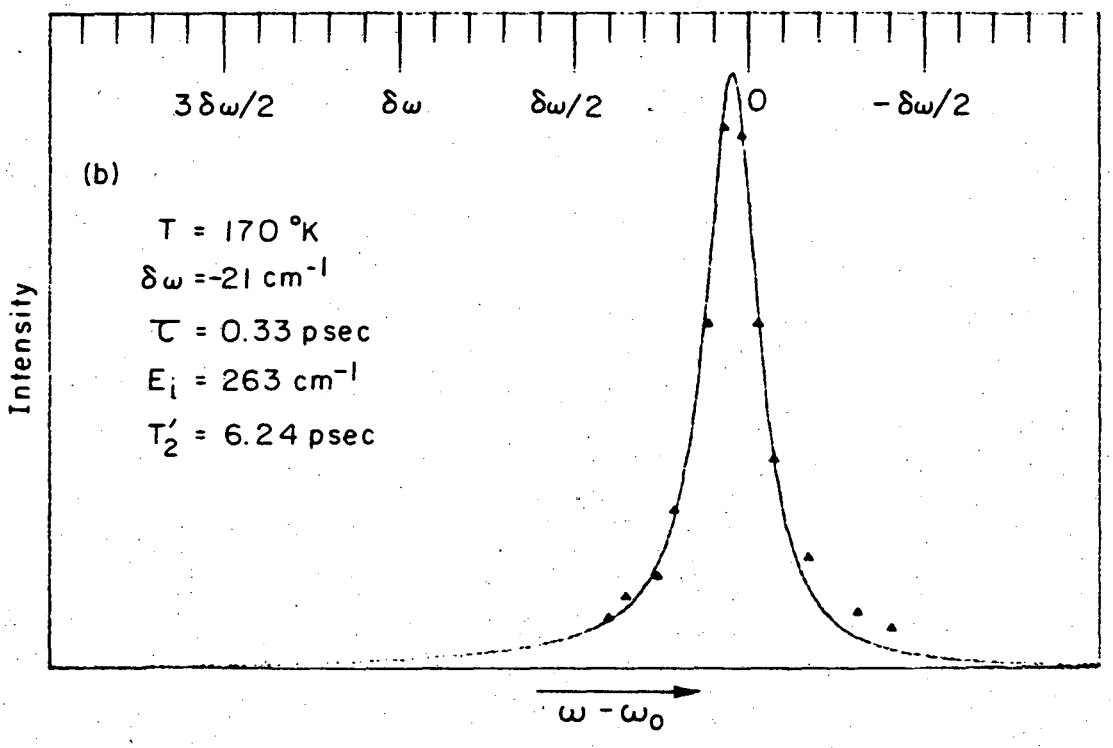

XBL7711-6472

Figure 43b

COMPARISON OF CALCULATED EXCHANGE LINESHAPE AND OBSERVED LINESHAPE
DURENE 3027 cm^{-1} VIBRATION

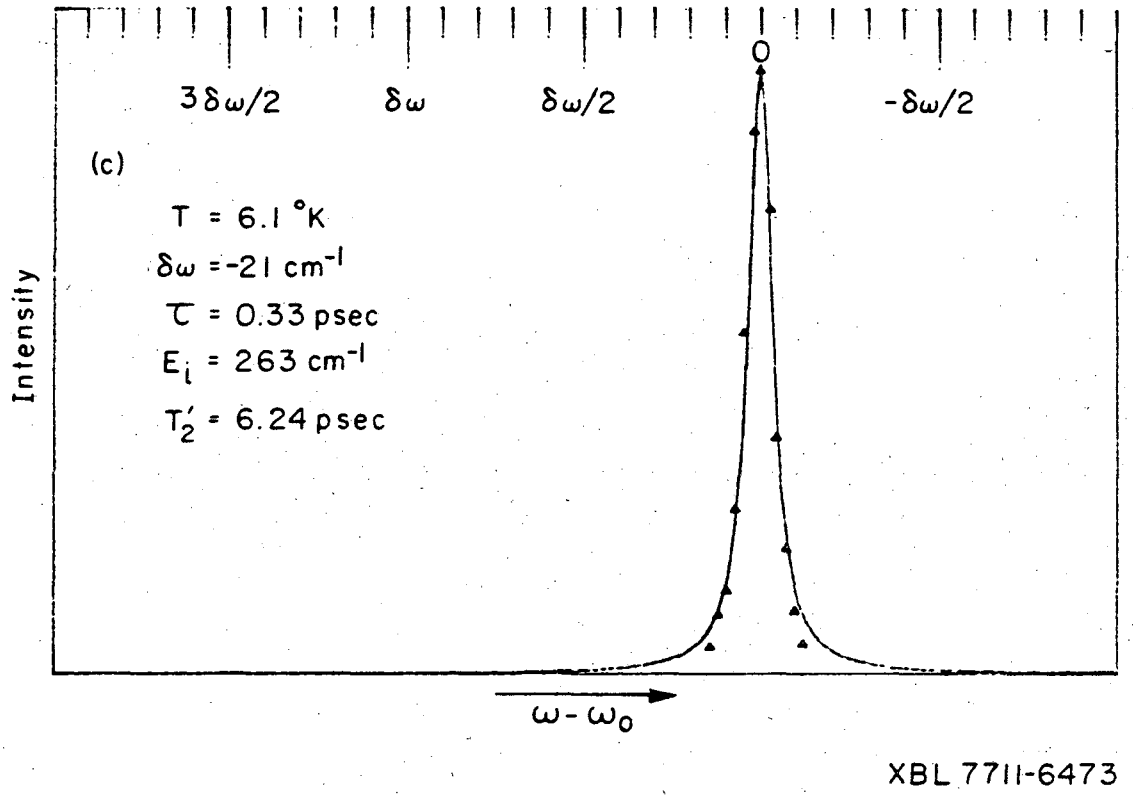

Figure 43c

very interesting, since it is a population relaxation time (T_1) for the mode undergoing exchange. This quantity is very hard to measure by other means, since it cannot be obtained directly from the linewidth of the corresponding Raman line. An approximation to the product $\delta\omega\tau$ can be obtained by dividing the contribution to the linewidth due to exchange by the shift of the apparent vibrational frequency from ω_o [see Eq. (95) and (96)]. This quantity is plotted as a function of temperature for the five durene lines in Fig. 44 and is constant to within experimental error, supporting the assumption of constant τ. It should be stressed that $|\delta\omega\tau|$ is of the order of unity for all five lines in the durene spectrum. It is this feature which makes the "intermediate exchange" regime accessible and results in the observation of significant frequency shifts due to exchange. From the temperature dependence of the exchange rate W_+ (see Fig. 42), it can be seen that these five vibrational modes are in intermediate exchange for temperatures between about 100°K and 300°K. At higher temperatures both W_+ and W_- increase, and the approximation of constant τ would not be appropriate.

When the low frequency vibrational spectrum of durene is examined, one finds (as indicated above for the 2929 cm^{-1} band) that the activation energies, E_i, correspond quite closely — with only one exception — to observed bands in the low frequency vibrational spectrum of durene. This correspondence is indicated in the column labeled "Dephasing Mode" in Fig. 42, along with the symmetry of these modes in the point group D_{2h}. The observed fundamental frequencies[117] for these modes are 187 cm^{-1} and 197 cm^{-1} for the torsion, 282 cm^{-1} for the methyl rock, and 354 cm^{-1} for the out-of-plane bend.

Fig. 44. This graph plots the portion of the line broadening due to the exchange process divided by the frequency shift. This quantity gives an approximation to the quantity $\delta\omega\tau$, and indicates that this product is constant as a function of temperature over the temperature range investigated (to within experimental error).

RATIO OF THE TEMPERATURE DEPENDENT PORTION OF THE LINEWIDTH AND FREQUENCY SHIFT IN THE RAMAN TRANSITIONS OF TETRAMETHYLBENZENE (DURENE)

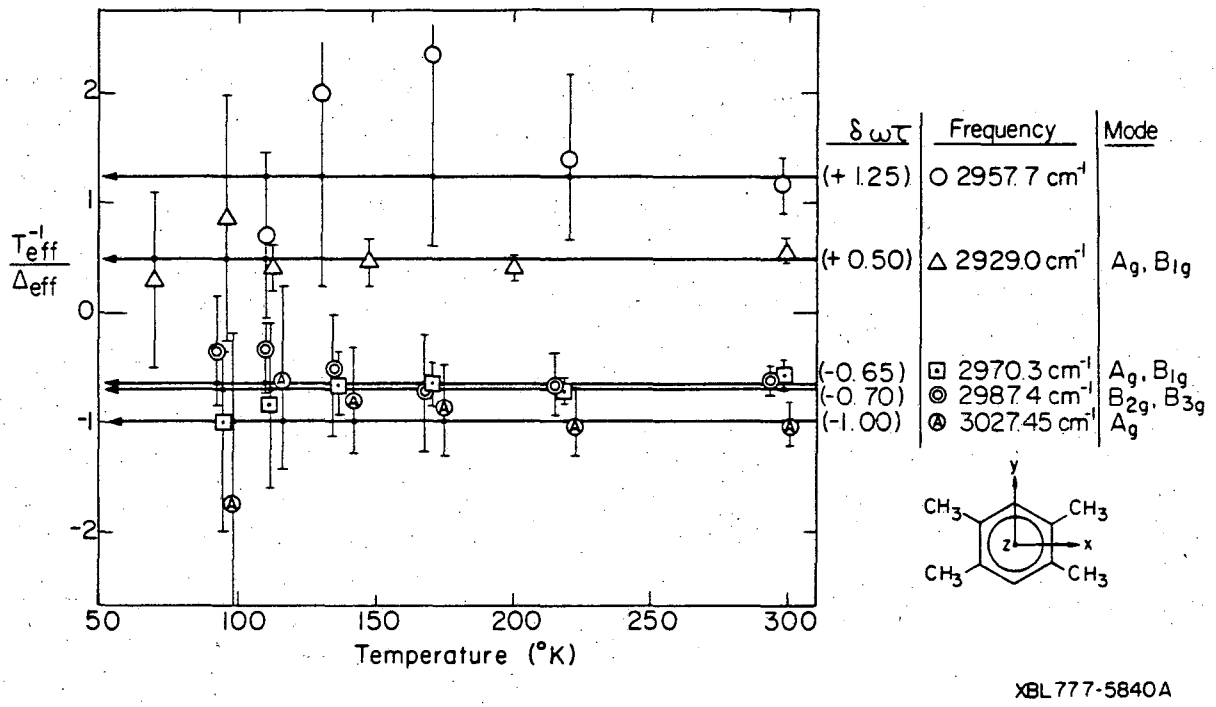

Figure 44

These results suggest that the interaction responsible for coupling the C-H stretching modes to these low frequency methyl group motions is very selective in nature. There are two probable sources of this selectivity, one which results from symmetry considerations and one which might be called "accidental" selectivity. Presumably the coupling is a result of mixed mode terms in the anharmonic potential energy. For reasons related to the structure of the molecule, some of these terms which couple a given C-H stretch to one low frequency mode may dominate those which couple it to other modes. This would typify "accidental" selectivity. On the other hand, the requirement that the potential energy possess the full symmetry of the molecule may imply the absence of some anharmonic coupling terms except for modes of certain symmetry classes, thus restricting the possible candidates for interaction.

To distinguish among these possibilities it is helpful to consider the importance of individual terms in the potential energy:

$$V = \sum_i C_i Q_i^2 + \sum_{i,j,k} C_{ijk} Q_i Q_j Q_k + \sum_{ijk\ell} C_{ijk\ell} Q_i Q_j Q_k Q_\ell + \cdots \tag{97}$$

In this expression, the C's are real coefficients while the Q's represent vibrational normal coordinates in the harmonic approximation. The second and third terms in Eq. (97) are the leading terms in the anharmonic part of the potential. We will restrict attention to cubic and quartic terms involving no more than two coordinates. Starting with harmonic oscillator base states, the contribution to $\delta\omega$ from each of these terms has been estimated to second order in perturbation theory. The only first order contribution is from terms of the form $C_{1122} Q_1^2 Q_2^2$

where Q_1 is the coordinate of a C-H stretch and Q_2 that of a low frequency mode. This contribution may be of either sign depending on the sign of the coefficient. There are no symmetry restrictions on these modes and this term cannot cause selectivity due to symmetry. A summary of the contributions from these various terms is shown in Table IV. The magnitudes were calculated assuming equal C-coefficients and are only intended to roughly indicate the relative importance of each term. They were calculated using values of ω_1 and ω_2 typical of the vibrational frequencies and activation energies observed. The sign of each contribution and any symmetry conditions are also indicated. The cubic terms all require that one mode or the other have a_g symmetry. Of these, by far the largest contribution comes from a combination of a Q_2^3 single-mode anharmonicity and $Q_1^2 Q_2$ coupling. Of the quartic terms, both the $Q_1^2 Q_2^2$ and $Q_1^3 Q_2$ terms have large contributions, and the latter indicates a symmetry-type selectivity which requires that both the C-H mode and the dephasing mode have the same symmetry. However, it is important to keep in mind that the actual contribution to $\delta\omega$ from these terms is determined largely by the sign and magnitude of the C-coefficients which are difficult to estimate or guess, and that the largest contribution to $\delta\omega$ for all these cases is likely to be the $Q_1^2 Q_2^2$ term which is diagonal and therefore contributes in first order. In addition, one would in general expect situations to occur where more than one exchanging mode is important. This introduces the possibility of coupling terms like $C_{123}\, Q_1 Q_2 Q_3$ which might be of importance in such a case.

From these considerations and with a knowledge of the symmetry assignment of each vibration, one might hope to decide which term or terms

TABLE IV. Contributions to $\delta\omega$ from various terms in the anharmonic potential.

Term	Symmetry rule	$\delta\omega$ [a]	Relative magnitude [b]	Sign
$Q_1^2Q_2$	$\Gamma_2 = a_g$	$-\left[\frac{4}{2\omega_1+\omega_2} + \frac{4}{2\omega_1-\omega_2}\right]\lvert C_{112}\rvert^2$	1.3×10^{-3}	-
$Q_1Q_2^2$	$\Gamma_1 = a_g$	$-\left[\frac{4}{\omega_1+2\omega_2} - \frac{4}{\omega_1-2\omega_2}\right]\lvert C_{122}\rvert^2$	4.7×10^{-4}	+
$Q_1^3 + Q_1Q_2^2$	$\Gamma_1 = a_g$	$-\left[\frac{4}{\omega_1+2\omega_2} - \frac{4}{\omega_1-2\omega_2}\right]\lvert C_{122}\rvert^2 - \frac{24C_{122}C_{111}}{\omega_1}$	7.5×10^{-3}	+/-
$Q_2^3 + Q_1^2Q_2$	$\Gamma_2 = a_g$	$-\left[\frac{4}{2\omega_1+\omega_2} + \frac{4}{2\omega_1-\omega_2}\right]\lvert C_{112}\rvert^2 - \frac{24C_{112}C_{222}}{\omega_2}$	9.3×10^{-2}	+/-
$Q_1Q_2^3$	$\Gamma_1\otimes\Gamma_2 = a_g$	$-\left[\frac{18}{\omega_1+3\omega_2} - \frac{18}{\omega_1-3\omega_2} + \frac{54}{\omega_1+\omega_2} - \frac{54}{\omega_1-\omega_2}\right]\lvert C_{1222}\rvert^2$	6.5×10^{-3}	+
$Q_1^3Q_2$	$\Gamma_1\otimes\Gamma_2 = a_g$	$-\left[\frac{18}{3\omega_1+\omega_2} + \frac{18}{3\omega_1-\omega_2} + \frac{54}{\omega_1+\omega_2} + \frac{54}{\omega_1-\omega_2}\right]\lvert C_{1112}\rvert^2$	4.0×10^{-2}	-
$Q_1^2Q_2^2$	none	$4C_{1122} - \left[\frac{16}{\omega_1} + \frac{16}{\omega_2} + \frac{8}{\omega_1+\omega_2}\right]\lvert C_{1122}\rvert^2$	3.9	+/-

[a] Calculated using second order perturbation theory.

[b] These quantities represent $\delta\omega$ in cm^{-1} for a situation where all C-coefficients are equal to 1 cm^{-1}, ω_1 = 3027 cm^{-1} and ω_2 = 263 cm^{-1}.

in the potential are important as far as the exchange process is concerned. However, this procedure is hampered by the lack of a full assignment of this region of the durene spectrum.[103]

The aromatic C-H stretch has a_g symmetry in D_{2h} and should clearly be assigned to the line at 3027 cm^{-1}. The corresponding dephasing mode is the methyl rock at 282 cm^{-1} which has either a_g or b_{1g} symmetry. Thus, any of the terms in Table IV may be important in the interaction. However, if a possible dephasing mode were not of a_g symmetry, the only important term would be the $Q_1^2Q_2^2$ term. It is possible that the methyl rock is singled out in this case because the contributions from several possible terms in combination overwhelm contributions from other modes which come from only single terms in the potential. However, if one thinks of the structure of the molecule and the methyl motion involved in this case, it seems intuitively sensible that the aromatic C-H stretch would couple more strongly to the methyl rock than to other low frequency methyl modes. Since the rocking motion is in the plane of the ring, it is not unreasonable that it should exert a stronger perturbation on the ring protons than either the torsion or out-of-plane bending modes.

The assignment of the methyl C-H stretching frequencies is less certain and the extent to which the results can be interpreted is therefore limited. A possible assignment is indicated in Fig. 42, and is based on a comparison with studies of other methylated benzenes.[104-106] The D_{2h} point group is used. The six C-H modes which are expected to appear in the Raman spectrum should occur in pairs of two essentially degenerate levels, since the splitting due to in-phase vs. out-of-phase motion of the protons on <u>different</u> methyl groups is expected to be very small. Since

the bands at frequencies less than 2920 cm^{-1} can be assigned as overtones and combinations of C-H bending or "scissors" modes of the methyl group protons, this leaves four lines and only three assignments. The assignment of the line at 2929 cm^{-1} is the most certain since it is well separated from the other three and probably corresponds to in-phase motion of the three methyl protons. It has been assigned accordingly in Fig. 42. However, it is not possible at the present to be certain of the remaining assignments. The choice indicated in Fig. 42 is suggestive, since the C-H modes and dephasing modes have the same symmetry. This ordering corresponds to the assignment of the methyl modes in toluene.[105] No explanation is offered though, of the observation of four methyl C-H lines rather than three.

With this assignment it appears that the mode at 2929 cm^{-1} interacts with a dephasing mode of different symmetry, in contrast to the aromatic C-H mode. This limits the possible terms in the anharmonic potential which could be responsible to the $Q_1^2Q_2^2$ term and some relatively minor terms.

It is possible that this term is dominant in many cases. It should be kept in mind that it makes the sole diagonal contribution to $\delta\omega$, and as such its contribution (ignoring any differences in the size of the $C_{ij...}$ coefficients) is about two orders of magnitude greater than that from other terms. Since this term offers no symmetry selection rules, it is difficult to see why a single dephasing mode is important to the exclusion of other possible dephasing modes. Apparently ignoring the size of the C's in comparing the contributions of various terms is not a wise procedure, since the magnitude of these coefficients may in fact play the most important role in determining which mode is selected as

dephasing mode. The only symmetry rule which selects for C-H stretching modes and dephasing modes of the same symmetry occurs when the $Q_1^3Q_2$ and/or $Q_1Q_2^3$ terms are dominant. In these cases also, it is difficult to see why the $Q_1^2Q_2^2$ term would not play an important role and why a single dephasing mode should be selected.

Thus, it is unclear whether or not symmetry rules play any role in selection of dephasing modes for each C-H stretch. The difficulty is enhanced by the lack of firm spectral assignments. The C-H modes apparently occur in degenerate pairs of differing symmetry which broaden and shift identically (since no sign of splitting is observed at any temperature). Since this degeneracy indicates that different methyl groups on the ring are essentially not coupled, it might seem more appropriate to consider the local symmetry of the independent methyl groups rather than using the D_{2h} group. The symmetry rules discussed above would then be only approximate or play very little role at all.

On the other hand, intuitive arguments and observations of space-filling molecular models indicate that steric interactions between adjacent methyl groups play an important part in the anharmonic interaction [Eq. (97)] responsible for $\delta\omega$. For example, steric interactions between the methyl rocking motion and the aromatic C-H stretch might play a dominant role in selecting this mode as dephasing mode. From this point of view, it is clear that the molecule as a whole (and thus the D_{2h} point group) should be considered to understand these interactions. We have not been able to resolve this dilemma on the basis of the data presented thus far. However, the importance of exchange in this system seems fairly clear, and the kinds of information available from application

of the theory to an experimental example has been demonstrated.

D. Conclusion

In conclusion, an approach to vibrational dephasing in condensed phases has been outlined which is potentially applicable to many experimental studies of lineshapes in vibrational spectra. The theory is presented in a manner which incorporates the interactions among the various degrees of freedom in a reasonably general and yet explicit way which leads to a clarification of the relationship between the random frequency modulation and modified Bloch equation approaches.

This formalism has been applied to the analysis of the Raman spectrum of durene in the C-H stretching region. It was found that single low frequency methyl group modes provide the dominant dephasing channels, and analysis of the temperature dependent lineshape in the intermediate exchange temperature range allowed the determination of energy exchange rates, lifetimes, and frequency shifts. The relationship between these quantities and the form of the potential responsible for the interaction of the dephasing modes with the C-H stretching modes was discussed. It was found that the $C_{1122}\ Q_1^2\ Q_2^2$ term in the anharmonic potential may play an important role in these interactions. It is hoped that this kind of information will be helpful in the future in elucidating the nature of interactions responsible for dephasing processes.

Finally, it should be pointed out that the exchange formalism is very versatile and can be applied in a similar manner in other branches of spectroscopy to provide a fuller understanding of the information contained in spectral lineshapes.

CONCLUSION

The main thrust of this work has been the understanding of the dynamics of excited states in condensed phase molecular systems from the point of view of coherence. Emphasis has been placed on the investigation and understanding of the phase of the excitations. These relaxation processes may be and usually are distinct from those which result in relaxation of the excited state population itself, and are in general more closely related to interesting properties of condensed matter such as transport phenomena and molecular motion. In particular, it has been demonstrated that the characterization of excited state energy transport requires a thorough investigation of the role of coherence.

In the field of triplet excitons in molecular crystals, indirect measurements such as the ones presented here have demonstrated the importance of coherent energy transport. "Average" properties such as the coherence length and coherence time have been investigated experimentally. On the other hand, very little has been said about the dynamics of individual states. For example, the scattering of population in one k-state in an exciton band to others is likely to be strongly dependent on k. This kind of information is not available and it is the kind of information that will be necessary to experimentally define the characteristics of exciton-phonon interactions.[3] Secondly, the experimental timescale is not easily available to directly investigate the interactions of delocalized exciton states (rather than thermalized distributions) with trap states.[21] Finally, the role of the coherence of the laser light in the excitation process

itself has only recently come to the forefront of this field, and this line of investigation promises to be very fruitful.[24, 25]

The situation in the case of picosecond investigations of vibrational dephasing and relaxation is somewhat different in that these measurements represent the decay of relatively well-defined states prepared coherently by the stimulated Raman excitation process. Considerable advances have been made in some cases in understanding the detailed nature of these relaxation processes.[77] The main difficulty in making such detailed statements lies in the inflexibility of the experimental technique. Since a proper understanding of these phenomena will require a survey of a variety of molecules and vibrational modes, improvements in picosecond technology and/or experimentalists' ingenuity will be needed. The present state of the art--the Nd: glass mode-locked laser--leaves much to be desired in versatility and convenience of use and forces one to chose a system to study for reasons of experimental convenience rather than scientific importance. A major step in the right direction for the field of vibrational dynamics is the recent development and use of tunable infrared picosecond pulses in the study of vibrational relaxation.[118]

Finally, the importance in polyatomic molecules of intramolecular perturbations in the understanding of coherence phenomena is beginning to emerge from several directions. The ideas presented here on the influence of vibrational energy exchange of dephasing processes is one example. The investigation of intramolecular dissipative interactions is more important in areas such as selective photochemistry and

radiationless relaxation[119] and should continue to be a topic of great interest. It is hoped that the exchange ideas and formalism will find quite general applicability in this and other fields.

ACKNOWLEDGEMENTS

I would like to express my sincere gratitude to all the members of the C. B. Harris research group. The interaction and environment they have provided is a valuable part of my education and my life.

I especially thank Professor Charles Harris for providing encouragement as well as timely scientific insights, suggestions and ideas. His guidence has been of great benefit to me.

I would also like to thank Paul Cornelius and Ahmed Zewail whose time, effort and thought have contributed substantially to this work.

This work was supported in part by the Materials and Molecular Research Division of the Lawrence Berkeley Laboratory under the auspices of the U. S. Energy Research and Development Administration, in part by a grant from the National Science Foundation, and by a National Science Foundation Graduate Fellowship.

REFERENCES

1. R. P. Feynman, R. B. Leighton, and M. Sands, The Feynman Lectures on Physics, Vol. III, Ch. 13, (Addison-Wesley, 1965).
2. A. S. Davydov, Theory of Molecular Excitons, (McGraw-Hill, 1962).
3. M. Grover and R. Silbey, J. Chem. Phys. 52, 2099 (1970); 54, 4843 (1971).
4. V. M. Kenkre and R. S. Knox, Phys. Rev. B 9, 5279 (1974).
5. For an excellent review of this work see A. Laubereau and W. Kaiser, in Chemical and Biochemical Applications of Lasers, C. B. Moore, ed., (Academic Press, 1976).
6. See For example, D. W. Oxtoby and S. A. Rice, Chem. Phys. Lett. 42, 1 (1976).
7. M. D. Fayer and C. B. Harris, Phys. Rev. B 9, 748 (1974).
8. See for example, J. Schmidt, D. A. Antheunis, and J. H. van der Waals, Mol. Phys. 54, 680 (1971).
9. A. H. Francis and C. B. Harris, Chem. Phys. Lett. 9, 181,188 (1971).
10. M. A. El-Sayed, J. Chem. Phys. 54, 680 (1971), and references therein.
11. A. H. Zewail and C. B. Harris, Chem. Phys, Lett. 28, 8 (1974); Phys. Rev. B 11, 935 (1975); 11, 952 (1975).
12. R. Schmidberger and H. C. Wolf, Chem. Phys. Lett. 25, 185 (1974).
13. C. B. Harris, R. L. Schlupp and H. Schuch, Phys. Rev. Lett. 30, 1019 (1973).
14. M. D. Fayer and C. B. Harris, Chem. Phys. Lett. 25, 149 (1974).
15. H. Brenner, J. C. Brock, M. D. Fayer and C. B. Harris, Chem. Phys.

Lett. 33, 471 (1975); M. T. Lewellyn, A. H. Zewail and C. B. Harris, J. Chem. Phys. 63, 3687 (1975).

16. C. B. Harris and M. D. Fayer, Phys. Rev. B 10, 1784 (1974).
17. R. M. Hochstrasser and J. D. Whiteman, J. Chem. Phys. 56, 5945 (1972); J. D. Whiteman, Ph.D. Thesis, Univ. of Pennsylvania, Philadelphia, Pa. (1971).
18. R. M. Hochstrasser and A. H. Zewail, Chem. Phys. 4, 142 (1974).
19. A. H. Francis and C. B. Harris, J. Chem. Phys. 57, 1050 (1972).
20. A. M. Nishimura, A. H. Zewail and C. B. Harris, J. Chem. Phys. 63, 1919 (1975).
21. It should be mentioned that other models have been put forth to solve the problem of Frenkel exciton trapping. Specifically, the impurity quenching parameters were added to the exciton density matrix master equation in the different migration limits. This theoretical treatment can be found in several references: R. M. Pearlstein, J. Chem. Phys. 56, 2431 (1972); R. P. Hemenger, K. Lakatos-Lindenberg and R. M. Pearlstein, J. Chem. Phys. 60, 3271 (1974).
22. This procedure has been modified (D. D. Dlott and M. D. Fayer Chem. Phys. Lett. 41, 305 (1976)) to include effects of temperature dependent exciton and trap lifetimes. However, this temperature dependence is difficult to separate from the effects of band-trap equilibria, and this correction is fairly small in this case.
23. The value of Δ reported in ref. 19 was used in these calculations, and since the results for the chain length depend on this value, it should be mentioned that other determinations of Δ have given

different values (eg. see ref. 22). These differences may reflect actual variations from one crystal to another. A measurement of the trap depth in the crystal used in the experiments described here gave $\Delta = 19$ cm $^{-1}$. This would give a value of the chain length within a factor of two of 256000.

24. A. H. Zewail and T. E. Orlowski, Chem. Phys. Lett. 45, 399 (1977).

25. T. J. Aartsma and D. A. Wiersma, Chem. Phys. Lett. 42, 520 (1976).

26. H. W. Mocker and R. J. Collins, Appl. Phys. Lett. 7, 270 (1965); A. J. DeMaria, D. A. Stetsen and H. Hyman, Appl. Phys. Lett. 8, 174 (1966).

27. See for example, J. A. Armstrong, Appl. Phys. Lett. 10, 16 (1967).

28. J. A. Giordmaine, P. M. Rentzepis, S. L. Shapiro, and K. W. Wecht, Appl. Phys. Lett. 11, 219 (1967).

29. D. von der Linde, IEEE J. Quantum Electron., QE-8, 328 (1972).

30. V. S. Letokhov, Soviet Phys. JETP, 27, 746 (1968); 28, 562 (1969); 28, 1026 (1969).

31. (a) A. Laubereau, D. von der Linde and W. Kaiser, Phys. Rev. Lett. 28, 1162 (1972).

(b) D. Ricard and J. Ducuing, J. Chem. Phys. 62, 3616 (1975).

32. V. Sundstrom, P. M. Rentzepis, and E. C. Lim, J. Chem. Phys. 66, 4287 (1977); J. P. Heritage and A. Penzkofer, Chem. Phys. Lett. 44, 76 (1976); R. M. Hochstrasser, D. S. King and A. C. Nelson, Chem. Phys. Lett. 42, 8 (1976).

33. G. E. Busch, M. L. Applebury, A. A. Lamola, and P. M. Rentzepis,

Proc. Nat. Acad. Sci. 69, 2802 (1972).

34. K. J. Kaufmann, P. L. Dutton, T. L. Netzel, J.S. Leigh, and P. M. Rentzepis, Science 188, 1301 (1975); M. G. Rockley, M. W. Windsor, R. J. Cogdell and W. W. Parson, Proc. Nat. Acad. Sci. 72, 2251 (1975).

35. (a) K. B. Eisenthal and K. H. Drexhage, J. Chem. Phys. 51, 5720 (1969);

(b) G. R. Fleming, J. M. Morris, and G. W. Robinson, Chem. Phys. 17, 91 (1976).

36. D. Huppert and P. M. Rentzepis, J. Chem. Phys. 64, 191 (1976).

37. T. J. Chuang, G. W. Hoffman, and K. B. Eisenthal, Chem. Phys. Lett. 25, 201 (1974).

38. G. E. Busch, R. P. Jones, and P. M. Rentzepis, Chem. Phys. Lett. 18, 178 (1973).

39. A. Laubereau and W. Kaiser, Opto-electronics 6, 1 (1974); G. E. Busch and P. M. Rentzepis, Science 194, 276 (1976): K. B. Eisenthal, Acc. Chem. Res. 8, 118 (1975).

40. I. D. Abella, N. A. Kurnit and S. R. Hartmann, Phys, Rev. 141, 391 (1966).

41. R. G. Brewer and R. L. Shoemaker, Phys. Rev. Lett. 27, 631 (1971).

42. S. L. McCall and E. L. Hahn, Phys. Rev. Lett. 18, 908 (1967).

43. R. G. Brewer and A. Z. Genack, Phys, Rev. Lett. 36, 959 (1976).

44. D. von der Linde, A. Laubereau and W. Kaiser, Phys. Rev. Lett. 26, 954 (1971).

45. A. Laubereau, D. von der Linde, and W. Kaiser, Phys. Rev. Lett. 27, 802 (1971); A. Laubereau, G. Wochner, and W. Kaiser, Opt. 14, 75 (1975).

46. For an excellent presentation of the physics of laser operation and related topics such as basic time-dependent quantum mechanics, quantum theory of radiation, coherent pulse propagation, and quantum theory of noise, see Sargent, Scully and Lamb.[47] Yariv[48] is also a good source in this area as well as in nonlinear optics and stimulated Raman scattering. For an introduction to the field of non-linear optics, Baldwin[51] is excellent. Finally, the works by Levine[49] and Ross[50] give a more practical approach to laser operation. They cover basic laser dynamics, theory of laser cavity modes, and give many experimental examples and references.

47. M. Sargent III, M. O. Scully, and W. E. Lamb, Laser Physics, (Addison-Wesley, 1974).

48. A. Yariv, Quantum Electronics, 2nd. ed., (John Wiley and Sons, 1975).

49. A. K. Levine, Lasers, Vol. I-III, (Marcel Dekhev, New York, 1968).

50. D. Röss, Lasers Light Amplifiers and Oscillators, (Academic Press, 1969).

51. Baldwin, Introduction to Non-linear Optics, (Plenum Press, New York, 1969).

52. Ref. 47, pp. 135-137.

53. D. J. Bradley, G. H. New, and S. J. Caughey, Phys. Lett. A30, 78 (1969).

54. D. von der Linde, O. Bernecker and A. Laubereau, Opt. Comm. 2, 215 (1970).

55. R. C. Hyer, H. D. Sutphin, and K. R. Winn, Rev. Sci. Inst. 46, 1333 (1975).

56. (a) M. R. Topp, P. M. Rentzepis and P. Jones, Chem. Phys. Lett. 9, 1 (1971).

(b) T. L. Netzel and P. M. Rentzepis, Chem. Phys. Lett. 29, 337 (1974).

57. See for example D. Magde and M. W. Windsor, Chem. Phys. Lett. 27, 31 (1974).

58. A. J. DeMaria, W. H. Glenn Jr., M. J. Brienza, and M. E. Mack, Proc. of IEEE 57, 2 (1969).

59. D. H. Auston, Appl. Phys. Lett. 18, 249 (1971).

60. D. von der Linde and A. Laubereau, Opt. Comm. 3, 279 (1971).

61. A. Penzkofer, D. von der Linde and A. Laubereau, Opt. Comm. 4, 377 (1972).

62. R. Y. Chiao, E. Garmire and C. H. Townes, Phys. Rev. Lett. 13, 479 (1964); P. L. Kelley, Phys. Rev. Lett. 15, 1005 (1965); Y. R. Shen, in Progress in Quantum Electronics 14, pp. 1-34 (1975).

63. N. Bloembergen and P. Lallemand, Phys, Rev. Lett. 16, 81 (1966); R. R. Alfano and S. L. Shapiro, Phys. Rev. Lett. 24, 584, 592, 1217 (1970).

64. F. Shimizu, Phys. Rev. Lett. 19, 1097 (1967).

65. A. Penzkofer, A. Laubereau, and W. Kaiser, Phys. Rev. Lett. 31, 863 (1973).

66. D. von der Linde and K. F. Rodgers, Opt. Comm. 8, 91 (1973).

67. A. Penzkofer and W. Kaiser, Appl. Phys. Lett. 21, 427 (1972); N. G. Basov, I. Kertes, P. G. Kryukov, Y. A. Matueets, Y. V. Senatskii, and S. V. Chekalin, Soviet Phys. JETP 33, 289 (1971).

68. G. W. Robinson, in Ann. Rev. of Phys. Chem. 21, 429 (1970).

69. E. R. Bernstein, S. D. Colson, R. Kopelman, and G. W. Robinson, J. Chem. Phys. 48, 5596 (1968).

70. R. G. Gordon, J. Chem. Phys. 40, 1973 (1964); 42, 3658 (1965); 43, 1307 (1965); Adv. Mag. Res. 3, 11 (1968).

71. L. A. Nafie and W. L. Peticolas, J. Chem. Phys. 57, 3145 (1972).

72. S. Bratos and E. Marechal, Phys. Rev. A 4, 1078 (1971); M. Constant and R. Fauguembergue, J. Chem. Phys. 58, 4030 (1973).

73. W. G. Rothschild, J. Chem. Phys. 65, 455 (1976).

74. R. R. Alfano and S. L. Shapiro, Phys. Rev. Lett. 26, 1247 (1971), 29, 1655 (1972); Opt. Comm. 6, 98 (1972); S. L. Shapiro, R. C. Hyer and A. J. Campillo, Phys. Rev. Lett. 33, 513 (1974).

75. D. Ricard, W. H. Lowdermilk, and J. Ducuing, Chem. Phys. Lett. 16, 617 (1972); D. Ricard, J. Chem. Phys. 63, 3841 (1975); see also ref. 31b.

76. P. R. Monson, S. Patumtevapibal, K. J. Kaufmann, and G. W. Robinson, Chem. Phys. Lett. 28, 312 (1974).

77. A. Laubereau, L. Kirschner, and W. Kaiser, Opt. Comm. 9, 182 (1973).

78. A. Laubereau, A. Seilmeier, and W. Kaiser, Chem. Phys. Lett. 36, 232 (1975); K. Spanner, A. Laubereau, and W. Kaiser, Chem. Phys. Lett. 44, 88 (1976).

79. A. Laubereau, Chem. Phys. Lett. 27, 600 (1974).

80. G. Renner and M. Maier, Chem. Phys. Lett. 28, 614 (1974); W. F. Calaway and G. E. Ewing, J. Chem. Phys. 63, 2842 (1975); S. R. J. Brueck and R. M. Osgood Jr., Chem. Phys. Lett. 39, 568 (1976).

81. R. M. Hochstrasser and J. E. Wessel, Chem. Phys. 6, 19 (1974).

82. P. C. M. van Woerkom, J. de Bleyser, M. de Zwart, and J. C. Leyte, Chem. Phys. 4, 236 (1974).

83. R. Fleming, O. L. J. Gijzeman, and S. H. Lin, J. Chem. Soc., Faraday Trans. II 70, 37 (1974); S. H. Lin, J. Chem. Phys. 65, 1053 (1976).

84. A. Nitzan, S. Mukamel, and J. Jortner, J. Chem. Phys. 63, 200 (1975).

85. D. W. Oxtoby and S. A. Rice, Chem. Phys. Lett. 42, 1 (1976).

86. D. J. Diestler, Chem. Phys. Lett. 39, 39 (1976).

87. P. A. Madden and R. M. Lynden-Bell, Chem. Phys. Lett. 38, 163 (1976).

88. S. F. Fischer and A. Laubereau, Chem. Phys. Lett. 35, 6 (1975).

89. J. P. Maier, A. Seilmeier, A. Laubereau, and W. Kaiser, Chem. Phys. Lett. 46, 527 (1977).

90. J. A. Giordmaine and W. Kaiser, Phys. Rev. 144, 676 (1966).

91. W. L. Peticolas, L. Nafie, P. Stein, and B. Fanconi, J. Chem. Phys. 52, 1576 (1970).

92. Y. R. Shen and N. Bloembergen, Phys. Rev. 137, A 1787 (1964).

93. M. Maier, W. Kaiser, and J. A. Giordmaine, Phys. Rev. 177, 580 (1969).

94. R. L. Carman, F. Shimizu, C. S. Wang, and N. Bloembergen, Phys. Rev. A 2, 60 (1970).

95. W. Kaiser and M. Maier, in Laser Handbook, F. T. Arecchi and E. O. Schutz-Du Bois, eds., (North Holland Pub., 1972), pp. 1077-1150; N. Bloembergen, Nonlinear Optics, (W. A. Benjamin, 1965).

96. See ref. 47, sections 8-1 and 13-1.

97. C. R. Chester, Techniques in Partial Differential Equations, Ch. 9, (McGraw-Hill, 1971).

98. A. Laubereau, G. Wochner, and W. Kaiser, Phys. Rev. A 13, 2212 (1976).

99. A. Laubereau, G. Wochner, and W. Kaiser, Opt. Comm. 17, 91 (1976).

100. F. B. Hildebrand, Introduction to Numerical Analysis, Ch. 6, (McGraw-Hill, 1956).

101. R. W. G. Wyckoff, Crystal Structures, Vol. VI, p. 350, (2nd ed., Wiley Interscience, 1969).

102. A. N. Winchell, The Optical Properties of Organic Compounds, (Univ. of Wisconsin Press, 1943).

103. N. Le Calve, G. Garrigou-Lagrange, M.-T. Forel, Z. Tomczak, and A. Tramer, J. Chem. Physique 63, 1446 (1966).

104. S. Julien-LaFerrierre and J.-M. Lebas, Spectrochim. Acta 27A, 1337 (1971).

105. J. K. Wilmshurst and H. J. Bernstein, Can. J. Chem. 35, 911 (1957); N. Fuson, J. Deschamps, C. Garrigou-Lagrange, and M.-T. Forel, J. Soc. Chim. Series 5, 95 (1959).

106. K. W. F. Kohlrausch, Monat. Für Chemie 76, 3 (1946); J. H. S. Green, Spectrochim. Acta. 26A, 1913 (1970); J. H. S. Green, D. J. Harrison and W. Kynaston, Spectrochim. Acta 27A, 793 (1971); 27A, 807 (1971).

107. G. Herzberg, Molecular Spectra and Molecular Structure, Vol. II, P. 334, (Van Nostrand, Reinhold, 1945).

108. P. W. Anderson, J. Phys. Soc. Jpn. 9, 316 (1954); see also ref. 109.

109. R. Kubo and K. Tomita, J. Phys. Soc. Jpn. 9, 888 (1954); R. Kubo, J. Math, Phys. 4, 174 (1963).

110. H. M. McConnell, J. Chem. Phys. 28, 430 (1958).

111. See ref. 47, Ch. 16-20.

112. W. H. Louisell, Quantum Statistical Properties of Radiation in Pure and Applied Optics, (John Wiley and Sons, 1973).

113. For a discussion of this point as applied to the magnetic resonance problem. see ref. 108.

114. The relationship between this one-time average, $\langle Q(t) \rangle$, and the two-time average or correlation function $\langle Q(t + \tau)\, Q(\tau) \rangle_{\tau}$, is related to the so-called Fluctuation-dissipation theorem and is discussed in detail in refs. 111 and 112.

115. A. Abragham, The Principles of Nuclear Magnetism, pp. 447-451, (Oxford Univ. Press, 1961).

116. C. A. van't Hof and J. Schmidt, Chem. Phys. Lett. 36, 460 (1975).

117. P. N. Prasad and R. Kopelmann, J. Chem. Phys. 58, 129 (1973); 58, 5031 (1973).

118. A. Laubereau, L. Greiter and W. Kaiser, Appl. Phys, Lett. 25, 87 (1974).

119. J. Jortner, S. A. Rice, and R. M. Hochstuasser, in Adv. in Photochem., Vol. VII, pp. 149-307 (1969).

This report was done with support from the Department of Energy. Any conclusions or opinions expressed in this report represent solely those of the author(s) and not necessarily those of The Regents of the University of California, the Lawrence Berkeley Laboratory or the Department of Energy.

TECHNICAL INFORMATION DIVISION
LAWRENCE BERKELEY LABORATORY
UNIVERSITY OF CALIFORNIA
BERKELEY, CALIFORNIA 94720